

Nonlinear Dynamics of the Additive-Pulse Modelocked Laser

A Thesis

Presented to the Faculty of the Graduate School

of Cornell University

in Partial Fulfillment of the Requirements for the Degree of

Master of Science

DISTRIBUTION STATEMENT A

Approved for public release;
Distribution Unlimited

19980430 052

by

Eric John Mozdy

January 1997

DTIC QUALITY

ATED 3

REPORT DOCUMENTATION PAGE			Form Approved OMB No. 0704-0188	
Public reporting burden for this collection of information is estimated to average 1 hour per response, including the time for reviewing instructions, searching existing data sources, gathering and maintaining the data needed, and completing and reviewing the collection of information. Send comments regarding this burden estimate or any other aspect of this collection of information, including suggestions for reducing this burden, to Washington Headquarters Services, Directorate for Information Operations and Reports, 1215 Jefferson Davis Highway, Suite 1204, Arlington, VA 22202-4302, and to the Office of Management and Budget, Paperwork Reduction Project (0704-0188) Washington, DC 20503.				
1. AGENCY USE ONLY (Leave Blank)		2. REPORT DATE January 1997	3. REPORT TYPE AND DATES COVERED Final	
4. TITLE AND SUBTITLE Nonlinear Dynamics of the Additive-Pulse Modelocked Laser			5. FUNDING NUMBERS	
6. AUTHORS Eric John Mozdy			AFRL-SR-BL-TR-98- 0371 REPORT NUMBER	
7. PERFORMING ORGANIZATION NAME(S) AND ADDRESS(ES) Cornell University			10. SPONSORING/MONITORING AGENCY REPORT NUMBER	
9. SPONSORING/MONITORING AGENCY NAME(S) AND ADDRESS(ES) AFOSR/NI 110 Duncan Avenue, Room B-115 Bolling Air Force Base, DC 20332-8080			10. SPONSORING/MONITORING AGENCY REPORT NUMBER	
11. SUPPLEMENTARY NOTES				
12a. DISTRIBUTION AVAILABILITY STATEMENT Approved for Public Release			12b. DISTRIBUTION CODE	
13. ABSTRACT (Maximum 200 words) See attached.				
14. SUBJECT TERMS			15. NUMBER OF PAGES	
			16. PRICE CODE	
17. SECURITY CLASSIFICATION OF REPORT Unclassified		18. SECURITY CLASSIFICATION OF THIS PAGE Unclassified	19. SECURITY CLASSIFICATION OF ABSTRACT Unclassified	20. LIMITATION OF ABSTRACT UL

© 1997 Eric John Mozdy

DTIC QUALITY INSPECTED

ABSTRACT

A model of the additive-pulse modelocked (APM) laser is developed, with an emphasis on nonlinear dynamics. The APM laser has been traditionally used as a stable, pulsed light source, with multiple regions of instability that hamper useful operation. Many of these instabilities are deterministic, resulting from large levels of nonlinearity, and can be exploited if understood. In this thesis, the different elements of a typical APM laser are studied, and their effects incorporated into a four-equation iterative model. The essentials of nonlinear dynamics are then presented, as tools for identifying and characterizing deterministic instabilities. The APM model is then used to simulate the laser under conditions of high nonlinearity, giving rise to quasiperiodicity, period-doubling, crises, and chaos. The chaotic regions of operation are characterized by embedding dimension and largest lyapunov exponent, and some sample attractors are plotted in three dimensions. The identification of the period-doubling route to chaos, the Lyapunov exponent quantification of the chaos, and the proof of quasiperiodicity and crisis behavior all represent new accomplishments and valuable insight into the APM laser dynamics.

BIOGRAPHICAL SKETCH

Eric J. Mozdy was born on December 26, 1970 in Erie, PA, and spent most of his early years in Meadville, a town just 40 miles south of Erie. He is the second youngest of eight children, and enjoys large groups of people. After attending Meadville Area Senior high School, he came to Cornell to pursue a degree in Electrical Engineering in 1989. He received a B.S. degree with highest distinction in 1993, and under the direction of Clifford Pollock, began graduate study at Cornell the same year. Soon thereafter, he married his wife, Rachel, a chemical engineer also from Cornell. Together, they have had two beautiful children, both girls, currently ages 1 and 2 1/2 years. Next to his family, he spends almost all of his time pursuing the MS/PhD degrees in the field of Electrical Engineering.

To my family.

ACKNOWLEDGEMENTS

I would first like to thank Dr. Clifford Pollock, who gave me the opportunity as an undergraduate to perform true laboratory research. It was this experience which led me to graduate study. Clif is an experienced mentor, and a good friend. I would also like to thank my other committee members for their valuable discussions, revisions of my thesis, and interest in my research.

The United States Air Force Laboratory Graduate Fellowship Program and the United States Joint Services Electronics Program (JSEP) have together made this work possible, through their funding of my graduate research. In addition, I would like to thank Doctors Tom Gavrielides, Vassilios Kovanis, and Tim Newell of Phillips Laboratory at Kirtland Air Force Base for my introduction to nonlinear dynamics, and for their valuable discussions and analysis software.

I cannot exaggerate the value of my wife's love and support and more importantly, her help with the technical aspects of my thesis. My graduate career has also been greatly influenced by my children, whose innocence and unconditional love lend a perfect balance to the seriousness of work.

Finally, I would like to thank my fellow students in the Pollock group, especially David Cohen, Martin Jaspan and Duane Barber, who have worked with me from my first year as a graduate student, and have taught me everything important about "real" laser systems.

Table of Contents

Biographical Sketch	iii
Dedication	iv
Acknowledgements	v
Table of Contents	vi
List of Tables	viii
List of Figures	ix
1 Introduction	1
1.1 Historical Perspective	1
1.2 Organizational Outline	2
2 The Additive-Pulse Modelocked Laser	4
2.1 An Introduction to Modelocking	4
2.2 The Laser Cavity	5
2.3 Theory	9
2.3.1 The NaCl Laser	9
2.3.2 Self-Phase Modulation	10
2.3.3 Pulse Shortening and Steady State	13
2.4 Modeling	15
2.4.1 Overview	15
2.4.2 Spectral Filtering	16
2.4.3 The Main Cavity: Gain	19
2.4.4 The Main Cavity: Net Model	24
2.4.5 The External Cavity: SPM	25
2.5 Numerical Model	27
2.5.1 Introduction	27
2.5.2 The Simulation Seed Pulse	27
2.5.3 Gain Constants	29
2.5.4 BTP Filter Specifications	31
3 An Overview of Nonlinear Dynamics and Chaos	34
3.1 Nonlinear Differential Equations and Phase-plane Analysis	34
3.2 Bifurcations	38
3.3 Chaos	42
3.3.1 Introduction	42

3.3.2	The Lorenz System	43
3.3.3	Lyapunov Exponents	46
3.4	Iterative Maps, Fractal Dimension, and Lyapunov Exponent Estimation	50
3.4.1	The Logistic Map	50
3.4.2	Fractal Dimension	54
3.4.3	The Ikeda Map and Attractor Reconstruction	56
3.4.4	The Practical Lyapunov Exponent	61
4	Simulated Additive-pulse Modelocked Laser Dynamics	64
4.1	Typical Operation	64
4.1.1	The Additive-pulse Modelocked Laser Model as a Map	64
4.1.2	Other Steady-state Experimental Observations	66
4.2	Nonlinear Laser Dynamics	68
4.2.1	Quasiperiodicity in the Simulated Laser	68
4.2.2	Period-doubling and Chaos in the Simulated Laser	71
4.2.3	Chaotic APM Behavior	75
4.2.4	Routes to Chaos	88
4.3	Exploring Parameter Space	92
4.3.1	Fiber Coupling Variations	92
4.3.2	Gain Variations	97
5	Conclusion	105
5.1	Model Limitations	105
5.2	Future Directions	110
5.2.1	Model Variations	110
5.2.2	Experimental Possibilities	111
A	ABCD Analysis of the NaCl APM Cavity	114
	Bibliography	118

List of Tables

2.1	Typical NaCl APM Laser Output Specifications	28
2.2	Laser Gain Parameters	30
2.3	Model BTP Parameter Specifications	33
4.1	Largest Lyapunov Exponents for APM Chaos	86

List of Figures

2.1	The NaCl APM Laser Cavity	7
2.2	Beam Waists within the APM Main Cavity	8
2.3	A Four-level Energy Band Schematic	10
2.4	A Gaussian Pulse and SPM-induced Phase Chirp	12
2.5	Interferometric Recombination of Chirped Pulses	14
2.6	A Schematic of the Field Amplitudes in the APM Laser	15
2.7	An Intracavity Birefringent Tuner Plate	16
2.8	Typical BTP Transmitted Intensity Versus Wavelength	17
2.9	The NaCl Gain Spectrum	18
2.10	The Total Main Cavity Filter Response	18
2.11	Pulse Traveling through Saturable Gain	20
3.1	Graphical Analysis of the Logistic Equation	36
3.2	Graphical Interpretation of the Logistic Equation	37
3.3	Logistic Equation Trajectories	37
3.4	Fixed Point Stability Analysis for a Simple Laser	41
3.5	Bifurcation Diagram for Simplified Laser	42
3.6	The Lorenz System Strange Attractor	45
3.7	The x-z Lorenz Attractor	46
3.8	The Lorenz Attractor: Sensitive Dependence	47
3.9	The Divergence of Nearby Trajectories	48
3.10	Lyapunov Exponent Calculation for the Lorenz Attractor	49
3.11	The Logistic Map: Period-One	51
3.12	The Logistic Map: Period-Two	51
3.13	The Logistic Map: Period-Four	52
3.14	The Logistic Map Bifurcation Diagram	53
3.15	Constructing the Koch Curve	55
3.16	The Ikeda Attractor	59
3.17	The Reconstructed Ikeda Attractor	60
4.1	The Steady-state Output of the Simulated APM Laser	65
4.2	Experimental Instabilities in the APM Laser	66
4.3	Stable Design: APM Output Energy vs. Fiber Length	67
4.4	A Fiber Length APM Laser Bifurcation Diagram	69
4.5	A Quasiperiodic APM Output Time Series	70

4.6	Phase Portrait of APM Quasiperiodicity	70
4.7	Deformation of the APM Quasiperiodicity	71
4.8	A Period-Doubling APM Laser Bifurcation Diagram	73
4.9	Period-two Pulses in the Main and External APM Cavities	74
4.10	A Magnification of the Period-Doubling and Chaos in the APM Bifurcation Diagram	76
4.11	Embedding Dimension Calculation for Chaos in Figure 4.8	77
4.12	An APM Chaotic Attractor: one of two at $l = 16.258$ cm	78
4.13	An APM Chaotic Attractor: two of two at $l = 16.258$ cm	79
4.14	An APM Chaotic Attractor: one of two at $l = 16.71$ cm	80
4.15	An APM Chaotic Attractor: two of two at $l = 16.71$ cm	81
4.16	An APM Chaotic Attractor: one of four at $l = 16.722$ cm	82
4.17	An APM Chaotic Attractor: two of four at $l = 16.722$ cm	83
4.18	An APM Chaotic Attractor: three of four at $l = 16.722$ cm	84
4.19	An APM Chaotic Attractor: four of four at $l = 16.722$ cm	85
4.20	Chaotic Pulses in the Main and External APM Cavities	87
4.21	Chaotic Transient in the APM Output Near $l = 16.3$ cm	91
4.22	Chaotic Transient in the APM Output Near $l = 16.72$ cm	93
4.23	The APM Fiber-coupling Bifurcation Diagram	95
4.24	A Magnified Fiber-coupling Bifurcation Diagram	96
4.25	Embedding Dimension Calculation for Chaos in Figure 4.23, $\gamma_1 >$ 0.315	97
4.26	An APM Chaotic Attractor: one of two at $\gamma = 0.316$	98
4.27	An APM Chaotic Attractor: two of two at $\gamma = 0.316$	99
4.28	The APM Laser Gain Bifurcation Diagram	100
4.29	Quasiperiodicity in the APM Gain Bifurcation Diagram	101
4.30	The APM Gain Bifurcation Diagram for Increased Fiber Coupling	102
4.31	A Magnified View of the Increased Fiber Coupling Gain Bifurcation Diagram	103
5.1	Simulator Pulse Discontinuity Due to Extreme Bandwidth	107
5.2	Discontinuity in the APM Simulation Output	108
5.3	A Typical NaCl High Reflector: the solid curve represents the re- sponse of an actual NaCl laser mirror scanned with a spectropho- tometer, and the dashed curve is the filter function used in the numerical simulations	108
5.4	Erroneous Dynamics in the APM Bifurcation Diagram	110

Chapter 1

Introduction

1.1 Historical Perspective

Mode-locked lasers have played an increasingly important role in scientific study in the past few decades. The predictable generation of ultrashort optical pulses has made possible the probing of ultrafast processes in semiconductors, the near delta-function excitation of optically absorbing materials, and ultrafast spectroscopy. As a result, mode-locked lasers undergo constant scrutiny for the purposes of better understanding, improved performance, and more robust control.

One common configuration called the additive-pulse mode-locked (APM) laser, was invented in 1984 by Mollenaeur and Stolen [1] under the name of the soliton laser. Since then, this same cavity configuration has been extensively studied and perfected. It has been found that this type of laser also operates in regimes that do not support solitons, and a more inclusive interferometric model has been adopted to describe this laser. With all of the efforts in perfecting the APM laser however, the more complicated, unstable nonlinear behavior has only recently attracted significant interest [2, 3]. Currently, a more detailed study of APM dynamics is

still lacking, and could provide some important clues to the limited stability of the laser itself. This thesis develops an iterative model to describe the APM operation, and studies the behavior of this model under several parameter variations. The results can aid in future APM designs, and help researchers to either exploit or avoid more complicated dynamics in the APM output.

1.2 Organizational Outline

Chapter 2 discusses the general design and physical cavity specifications of the APM laser. The chapter then studies the physical processes which form the basis for APM laser operation, and the combination of these processes to form modulated pulses. Based upon the interferometric model of the APM laser, four steady-state equations are then developed to express the propagation of pulses through the laser.

Chapter 3 begins by explaining the fundamentals of nonlinear dynamics. It explains the concepts of bifurcations, chaos, and strange attractors. This chapter also addresses iterative mappings, routes to chaos, and the phase-space reconstruction of attractors. Much of this introductory development follows Strogatz [17], and the interested reader can look there for a more detailed treatment. The quantitative measures of fractal dimension and Lyapunov exponents are presented, with practical analysis methods as they will relate to the APM laser.

The APM model is revisited in Chapter 4, where the original, stable, steady-state laser of Chapter 2 is studied and verified. Next, the APM equations are used to demonstrate the more complicated dynamics of this laser, including period-two and greater behavior as well as chaos. The analytical techniques developed in Chapter 3 are then used to better characterize the APM dynamics.

Finally, Chapter 5 presents approximations and limitations of the APM model as developed in this thesis. This chapter also discusses future applications of this work, including several experimental ideas for improved APM performance.

Chapter 2

The Additive-Pulse Modelocked Laser

2.1 An Introduction to Modelocking

Modelocking methods can in general be classified into one of two categories: active and passive. The active case typically refers to driven lasers, where some kind of intracavity element modulates the optical loss with some multiple of the round-trip cavity time. As a result, pulses form which pass through the modulator during a peak in the transmission temporally narrow until they experience minimal loss from the modulator. Equivalently, in the frequency domain, each of the concurrent longitudinal modes of the laser acquires modulation sidebands which, when the modulator operates at some harmonic of the cavity frequency, overlap with and injection lock neighboring modes. As a result, most of the longitudinal modes lock together to “mode-lock” the laser.

In contrast, passive modelocking involves the use of some intracavity element which passively favors pulsed operation. For example, several passive schemes uti-

lize a saturable absorber, which acts as loss for low-intensity (CW) light, but saturates for high-intensity pulses. Other techniques utilize special material properties or particular cavity configurations to encourage pulsing. The Kerr lens modelocking technique, for example, relies on the optical Kerr effect to form a lens within the gain medium which varies in strength for low or high-intensity fields. The laser cavity is then designed with the help of apertures to favor the high-intensity case, so as to encourage pulsed behavior. In general, passive modelocking techniques generate shorter pulses, because material properties generally act on faster timescales than active modulation electronics.

The additive-pulse modelocked (APM) laser falls into the passive category, because it relies on the process of self-phase modulation (SPM) within an optical fiber to favor pulses. In addition, this technique utilizes two coupled cavities: the main cavity contains the gain and tuning elements which form the laser oscillator, and the external cavity houses an optical fiber which provides the SPM. A fraction of the light from each pulse in the main cavity couples to the external cavity, obtains a phase chirp while traveling through the fiber due to SPM, then interferometrically recombines with the main cavity pulses to form narrower, compressed pulses. The remainder of this chapter presents a typical APM laser design in detail, including a mathematical examination of the physical processes just summarized, which connect SPM with short pulse generation.

2.2 The Laser Cavity

A schematic of the NaCl additive-pulse modelocked (APM) laser is shown in Figure 2.1. The laser consists of main and external cavities, each ~ 187.5 cm in length, to establish an 80 MHz output pulse repetition rate. The main cavity con-

sists of the NaCl gain medium, birefringent tuner plate (BTP), focusing optics, a high reflector on one end, and an output coupler on the other. The NaCl crystal is ~ 1.75 mm thick, and mounted at Brewster's angle ($\sim 57^\circ$) on a copper cold finger, held at 77 °K to prevent thermal degradation of the active defects in the crystal. Two $f = 5$ cm lenses are used to form a very tight ($\sim 10\mu\text{m}$) beam radius in the gain medium. The BTP is a 0.3 mm thick crystal quartz optic, used both to wavelength tune and bandwidth-limit the laser's output pulse spectrum.

The external cavity, delimited by the main cavity output coupler on one end and its own high reflector on the other, contains a short length of optical fiber. We used Corning Corguide dispersion-shifted ($D = 0$ at $\lambda = 1.55\mu\text{m}$) fiber, with a core diameter of $\sim 10\mu\text{m}$. Because of this small core diameter, the light focused into the fiber attains high intensities, and experiences a nonlinear phase shift upon propagation. At each end of the fiber, 5 mm diameter AR-coated coupling spheres help to mode-match the optical mode of the external cavity to that in the fiber core. Index-matching gel fills the gap between the coupling sphere and fiber, to minimize reflection losses at the fiber ends. The external cavity high reflector is mounted on a PZT translator, in order to dynamically adjust the length of the external cavity, and thus control the relative phase between the main and external cavities.

Using ABCD matrix formalism, the beam waist can be determined everywhere within the main cavity (see Appendix A). This not only confirms the stability of the cavity, but also yields the beam waists in the gain and at the output coupler. These parameters are essential to numerically simulating the laser behavior, described later in Section 2.5. The results of the ABCD analysis are shown in Figure 2.2.

The lenses surrounding the NaCl crystal have been positioned quite close to

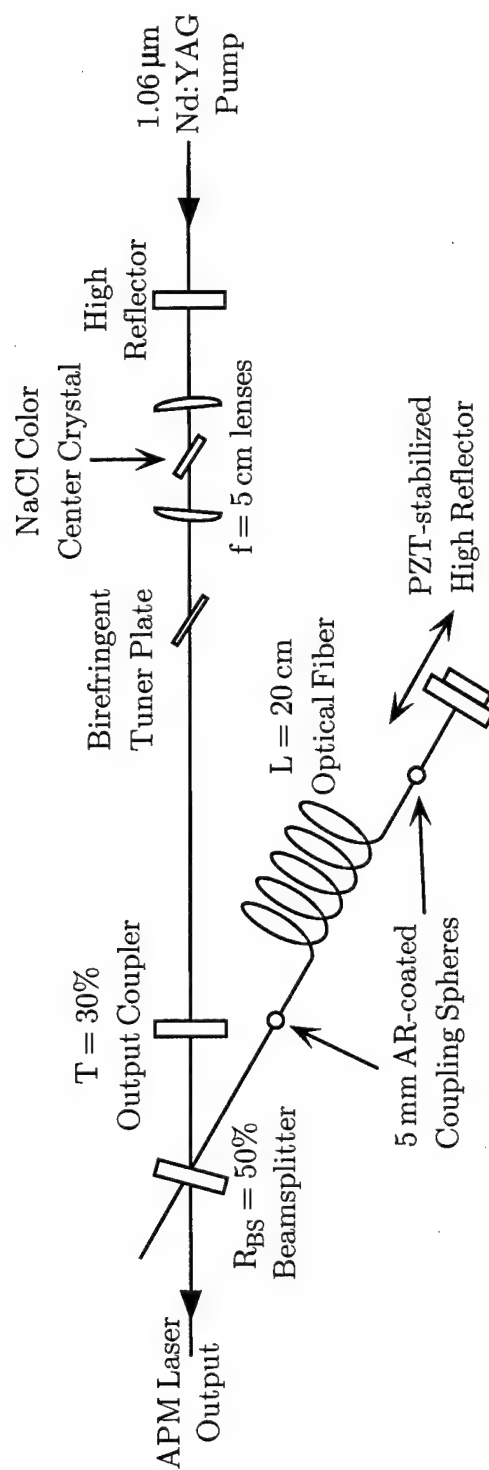


Figure 2.1: The NaCl APM Laser Cavity

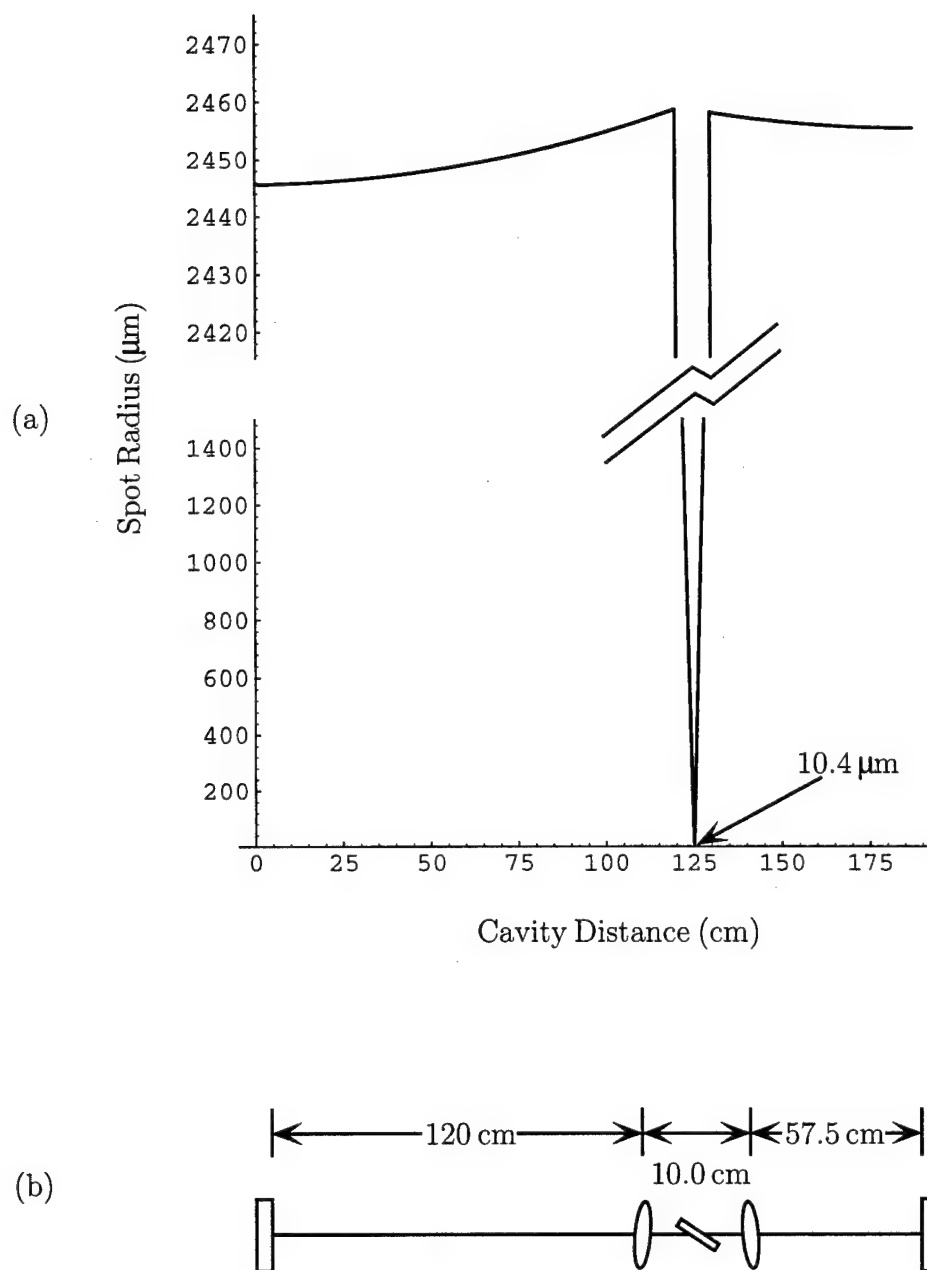


Figure 2.2: Main Cavity Beam Waists (a) shows the beam radius as a function of cavity location as calculated by an ABCD matrix evaluation, and (b) gives the corresponding schematic representation of the cavity

the crystal, in order to generate the tight, $10\text{ }\mu\text{m}$ beam waist inside the gain. This positioning, shown in Figure 2.2 b, creates a cavity near the edge of stability, which additionally generates the large, $\sim 5\text{ mm}$ output beam diameter. An experimental NaCl APM laser can easily be operated in this regime, by carefully adjusting the lenses as close as possible to the gain. These cavity dimensions, particularly the tight beam waist in the gain, enhance the complicated nonlinear dynamics explored in Chapter 4, and provide a large parameter space for the observation of laser bifurcations and chaos. Moreover, the knowledge that a tight gain beam waist provides such a large parameter space can assist future APM cavity design, especially toward encouraging complicated nonlinear output. Several other ways of accomplishing this enlarged parameter space exist, including the use of very short optical fiber in the external cavity, or different focusing lenses in the main cavity, but the simple cavity alignment used in Figure 2.2 is most easily implemented.

2.3 Theory

2.3.1 The NaCl Laser

The APM laser has two coupled cavities, as described in section 2.2 above. The main cavity is essentially an “ordinary” laser, in the sense of being a simple optical oscillator, and is responsible for providing laser output in the $1.5\text{--}1.7\text{ }\mu\text{m}$ range.

The gain medium is a NaCl crystal, containing intentional defects called color centers. The fundamental building block of color centers in alkali halides is the F-center, an electron trapped in an anion vacancy. An F_2^+ -center is an F center adjacent to another anion vacancy without a trapped electron. The particular color center in the NaCl lattice is the $F_2^+O_2^-$ defect, which involves an F_2^+ center

adjacent to an O^{2-} substitutional impurity (replaces a Cl^- ion) [4, 5, pp. 8,23].

An energy band diagram for the NaCl crystal with the $F_2^+O_2^-$ defect contains states resulting from the allowed energies of the trapped F center electron, combined with vibronic states due to the NaCl lattice. Using the configurational coordinate model [6, 7], the NaCl gain medium can be shown to act as a 4-level system [5, pp. 10-17] (see Figure 2.3). The radiative lifetime of the system is τ_2 while τ_1 and τ_3 characterize very fast, nonradiative transitions. The actual values of these lifetimes will be considered in Section 2.5.3, after a detailed analysis of the gain in Section 2.4.3.

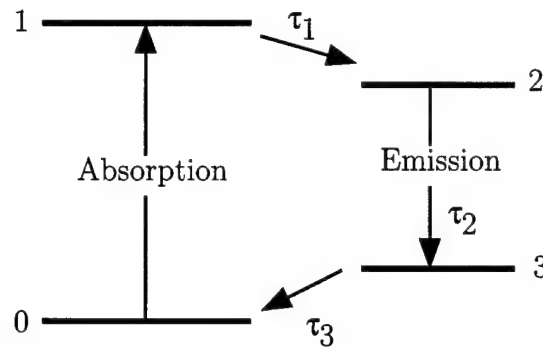


Figure 2.3: A Four-level Energy Band Schematic

2.3.2 Self-Phase Modulation

In almost any material, under conditions of high electric field, the polarization response of the material to the field will be at least weakly nonlinear. The polarization (or, more specifically, the susceptibility) can then be expressed in a series expansion:

$$\mathbf{P} = \epsilon_0(\chi_1 + \chi_2\mathbf{E} + \chi_3\mathbf{E}\mathbf{E} + \cdots)\mathbf{E} \quad (2.1)$$

Under this expansion, the first (χ_1) component accounts for all of linear optics, the second term for sum and difference frequency generation and Pockel's effect, while

the third term (χ_3) accounts for phenomenon like third-harmonic generation and self-phase modulation. Only materials with non-centrosymmetric crystal structure can exhibit χ_2 effects, such as second-harmonic generation. Third-harmonic generation, on the other hand, is possible in almost all materials, but for any appreciable effect requires precise phase matching conditions on the optical k-vectors, which are rarely satisfied.

Unlike third-harmonic generation, self-phase modulation (SPM) is a commonly observed χ_3 effect, since it does not require any explicit phase-matching efforts. With SPM, the polarization leads to an intensity-dependent index of refraction ($I \propto |E|^2$):

$$n(I) = n_0 + n_2 I \quad (2.2)$$

n_0 is the usual (linear) index of refraction, and the n_2 value is usually positive and quite small ($3.2 \times 10^{-16} \text{cm}^2/\text{W}$ in fused silica [8, pg. 201]), so this effect is not commonly observed under terrestrial conditions. In the case of optical fibers, an optical field can easily be large enough to induce SPM, because the small fiber core diameter leads to relatively high intensities.

When a pulse experiences SPM, the leading and trailing edges of the pulse travel faster than the center of the pulse, since the center has a larger $n(I)$, and therefore a smaller phase velocity, $v_p = c/n$. For this reason, the optical carrier wave on the leading side of the pulse is stretched (frequency decreased), while the wave is compressed (frequency increased) on the trailing edge of the pulse, creating a monotonically increasing frequency “chirp” across the entire pulse.

Examining the effect of SPM on a Gaussian pulse envelope:

$$E(t) = E_0 e^{-at^2} \quad \text{or} \quad I(t) = I_0 e^{-2at^2} \quad (2.3)$$

In traveling a length L , this pulse would normally accumulate phase as

$$e^{-jkL} = e^{-jL \frac{2\pi n_0}{\lambda_0}} \quad (2.4)$$

while SPM would add the additional phase

$$e^{-j\delta\phi} = e^{-j(\frac{2\pi L}{\lambda_0}) n_2 I(t)} \quad (2.5)$$

Since the additional phase depends only on the intensity of the pulse, phase will accumulate linearly with the distance traveled. From this expression of the additional SPM phase, the frequency chirp is given by

$$\delta\omega(t) = \frac{d}{dt} \delta\phi(t) = \frac{2\pi n_2 L}{\lambda_0} \frac{dI(t)}{dt} \quad (2.6)$$

where $\frac{dI(t)}{dt} = (-4at)e^{-2at^2}$. This relationship between a Gaussian pulse and the chirp due to SPM is seen in Figure 2.4. The central region of the pulse acquires essentially linear phase.

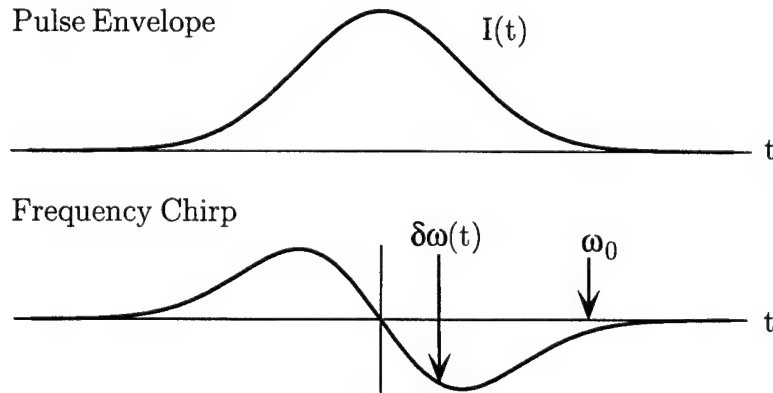


Figure 2.4: A Gaussian Pulse and SPM-induced Phase Chirp

The optical fiber plays a special, nonlinear role in the APM laser. The external cavity is passive, and optical pulses are simply guided through fused silica, then reinjected back into the main cavity. Because of the small core diameter of the fiber however, SPM becomes significant, and each pulse acquires a phase chirp. Section 2.3.3 describes how this phase chirp contributes to modelocked behavior.

2.3.3 Pulse Shortening and Steady State

Any laser oscillator contains some noise, from spontaneous emission in the gain to stray optical radiation or even mechanical vibration perturbing the laser cavity. It is these same noise sources that make laser oscillation, and especially modelocked operation, possible. When the laser is first "turned on," i.e., the gain medium is excited, but no laser oscillation is present, a single noise photon will pass through the cavity with just the right alignment to cause the cascade of stimulated emission which forms the laser's output. In the case of modelocked operation, essentially the same process occurs, but the cavity has been designed to favor pulses.

In the APM laser, for example, a noise spike from the main cavity will enter the external cavity fiber and obtain a chirp. When this small phase-chirped pulse from the external cavity strikes the output coupler of the main cavity, it interferometrically combines with the original, main cavity noise spike (pulse). Figure 2.5 shows a sample result of the combination process. Because the chirped pulse has faster and slower frequency components on its wings as compared to the center, when properly phase adjusted it will destructively interfere with the main cavity pulse on the wings, but constructively interfere at the peak. This pulse will repeatedly circulate in the main cavity, become amplified, and be reinjected into the external cavity, each time getting temporally shortened. Thus, the self-phase modulation of the optical fiber in the external cavity of the APM laser will help to produce short, modelocked pulses.

A steady state is established when the pulse shortening effect of the SPM is balanced by spectral filtering and dispersion in the APM cavity. As explained by the uncertainty principle, overall spectral narrowing will in general be accompanied by temporal broadening, and vice-versa. The familiar Heisenberg uncertainty

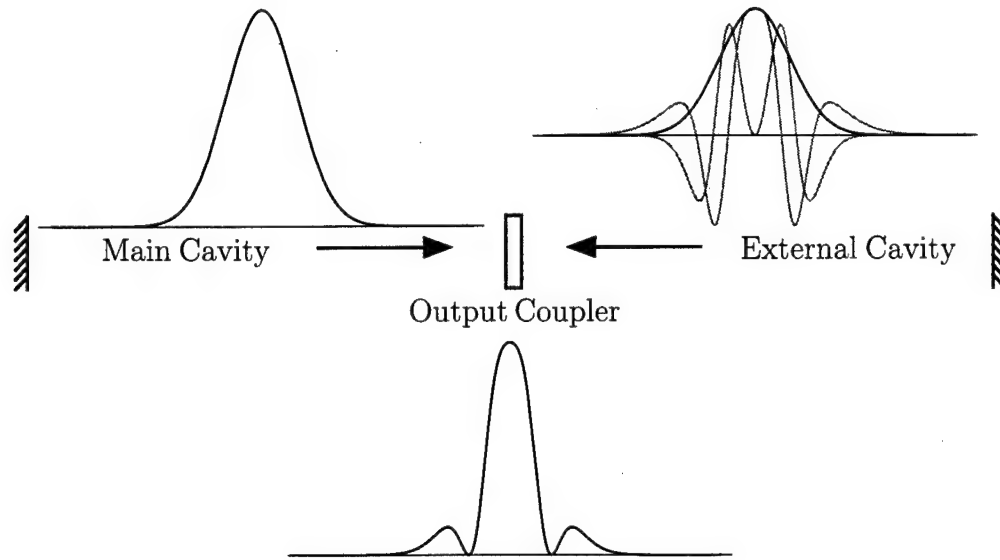


Figure 2.5: A schematic of interferometric recombination of APM Pulse intensities: the main cavity pulse with no phase chirp combines with the SPM-chirped control cavity pulse (shown with real and imaginary field components), to produce an interferometrically compressed pulse

relation

$$\Delta E \Delta t \geq \hbar/2 \quad \Rightarrow \quad \Delta \nu \Delta t \geq \frac{1}{4\pi} \quad (2.7)$$

relates a pulse's spectral width $\Delta \nu$ to its temporal duration τ . Thus, the bandwidth of the filtering process in the main cavity ultimately determines the shortest achievable modelocked pulsewidths. This filtering can arise from a number of processes, but it generally involves a tuning element (such as a birefringent tuner plate), the finite gain bandwidth of the NaCl crystal, or simply uncompensated group velocity dispersion within the laser cavity.

2.4 Modeling

2.4.1 Overview

A model of the APM laser which incorporates the above concepts relies upon the combination of the main and external cavity pulses at the output coupler, as defined in Figure 2.6. The incident and reflected field amplitudes on either side of

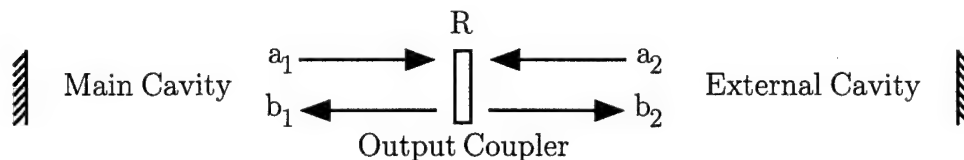


Figure 2.6: A Schematic of the Field Amplitudes in the APM Laser

the output coupler can be simply related through the reflection and transmission coefficients of the output coupler:

$$b_1 = a_1\sqrt{R} + a_2\sqrt{(1-R)} \quad (2.8)$$

$$b_2 = a_1\sqrt{(1-R)} - a_2\sqrt{R} \quad (2.9)$$

where R is the intensity reflectivity of the output coupler. The elements of the main and external cavities will determine the relationships between a_1 and b_1 , and a_2 and b_2 . Sections 2.4.2 and 2.4.3 will describe the function of the main cavity, and Section 2.4.4 will formulate this into a main cavity operator. Similarly, Section 2.4.5 will formulate the effects of SPM on the pulses defined in Figure 2.6, and express this as an external cavity operator. These operators, combined with (2.8) and (2.9), will form a complete model of the APM laser's behavior.

2.4.2 Spectral Filtering

The main cavity contains the filtering mechanism and the laser gain. Filtering in the laser of Figure 2.1 is performed both by a birefringent tuner plate (BTP), and the finite gain bandwidth of the NaCl crystal. We can consider both of these in turn.

A schematic of the intracavity BTP, displayed in Figure 2.7, shows the relevant BTP parameters: θ , the angle formed by the surface of the plate and the cavity optic axis, and ϕ , the angular deviation of the plate's extraordinary axis \vec{a} from vertical when rotated around an axis normal to and passing through the center of the plate.

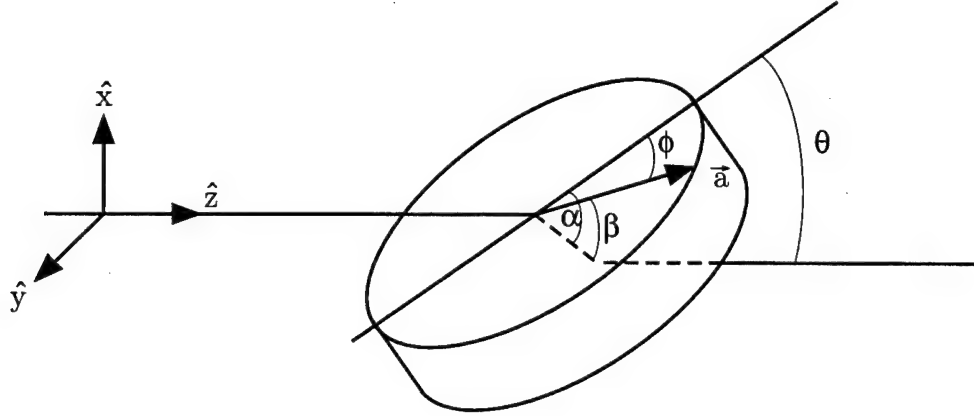


Figure 2.7: An Intracavity Birefringent Tuner Plate

A detailed analysis of tuner plate transmission as a function of orientation was performed elsewhere, to obtain the following expression for the TM-polarized intensity versus wavelength [9],

$$I_T(\lambda) = 1 - \sin^2(2\phi) \frac{n_0^4 - n_0^2 \cos^2 \theta}{(n_0^2 - \cos^2 \phi \cos^2 \theta)^2} \times \sin^2 \left(\frac{\pi t}{\lambda} \left\{ \frac{n_e [1 + \cos^2 \theta \cos^2 \phi (\frac{1}{n_e^2} - \frac{1}{n_0^2})]}{[1 - \cos^2 \theta (\frac{\sin^2 \phi}{n_e^2} + \frac{\cos^2 \phi}{n_0^2})]^{1/2}} - \frac{n_0}{[1 - \frac{\cos^2 \theta}{n_0^2}]^{1/2}} \right\} \right) \quad (2.10)$$

where n_0 and n_e are the ordinary and extraordinary indices of refraction for the

birefringent plate (crystalline quartz in this case), respectively, and t is the plate thickness. A typical BTP response function is shown in Figure 2.8 for $t = 1.75$ mm.

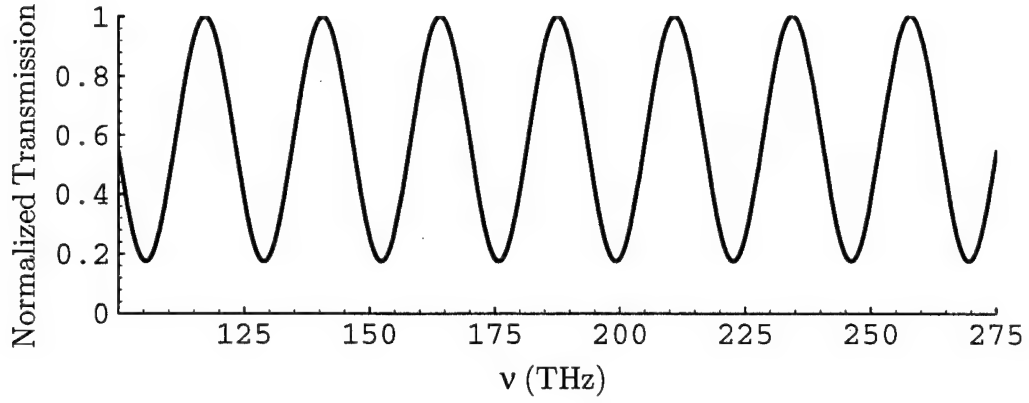


Figure 2.8: Typical BTP Transmitted Intensity Versus Wavelength

Given that the BTP is positioned in the laser cavity at Brewster's angle,

$$\tan \theta_B = n \quad \Rightarrow \quad \theta_B = 56.8^\circ \quad (2.11)$$

the TM-polarized light will experience no amplitude loss due to Fresnel reflections. Also, given the 8 Brewster surfaces per round trip in the main cavity, we can assume that the surviving TE component of the intracavity laser mode is negligible. Thus, (2.10) is the (one pass) frequency response of the main cavity.

The bandwidth of the NaCl crystal also contributes to filtering in the main cavity. Due to the coupling of the NaCl crystal's lattice vibrations with the F-center's unperturbed energy band structure, the gain emission spectrum is Gaussian in shape [5]. Given a gain bandwidth of $\delta\nu = 45$ THz [10] centered at $\nu_0 = 1.875$ THz ($1.60 \mu\text{m}$), the normalized gain versus frequency can be expressed as

$$G(\nu) = e^{-4 \ln 2 (\nu - \nu_0)^2 / \delta\nu^2} \quad (2.12)$$

This gain spectrum is shown in Figure 2.9.

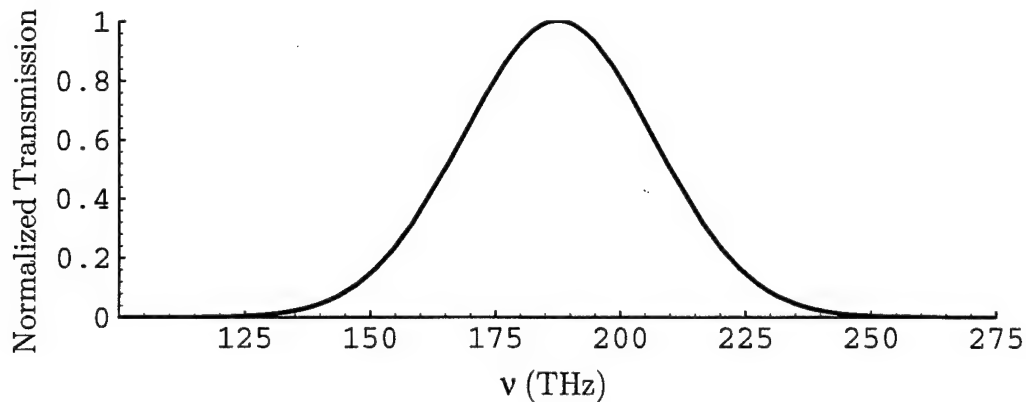


Figure 2.9: The NaCl Gain Spectrum

Modeling the filtering of both the BTP and the gain can then be achieved by taking the Fourier transform of some input pulse, $p(t)$, multiplying by both frequency responses, (2.10) and (2.12), then taking the inverse Fourier transform. Thus, the main cavity filter operator $\hat{\mathcal{F}}$ becomes

$$\hat{\mathcal{F}}(p(t)) = \frac{1}{2\pi} \int_{-\infty}^{\infty} e^{j\omega t} I_T(2\pi c/\omega) G(\omega/2\pi) \left[\int_{-\infty}^{\infty} e^{-j\omega t} p(t) dt \right] d\omega \quad (2.13)$$

The combined filter response, $I_T(2\pi c/\omega) G(\omega/2\pi)$, is shown in Figure 2.10

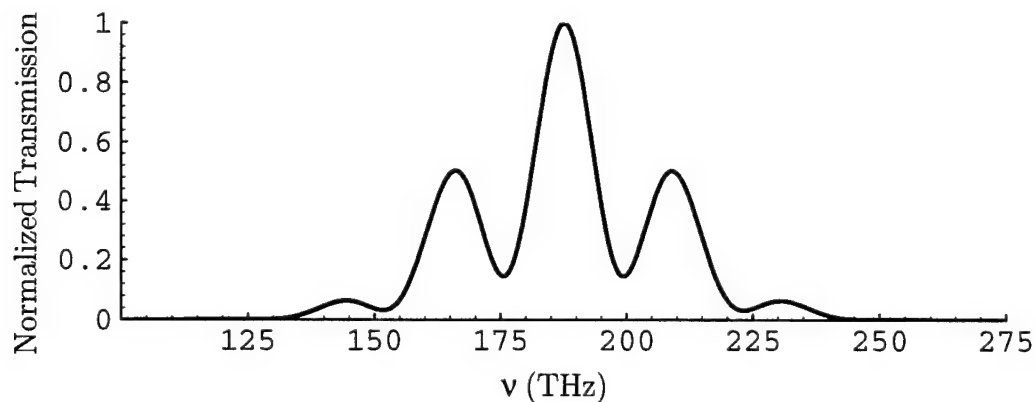


Figure 2.10: The Total Main Cavity Filter Response

2.4.3 The Main Cavity: Gain

To analyze the effects of saturable gain on short pulses, we can use the technique of Seigman [11, pp. 363–368], with the following assumptions:

- 1) Although the pulses are quite short, the rate equation approximations for analysis of the gain are still valid, being dominated by the extremely fast dephasing time of the excited state.
- 2) The pulse duration is short enough that stimulated emission is the only significant process altering the upper lasing level population; i.e, pumping, spontaneous emission, and non-optical transitions from the upper level are negligible during this time.

To begin the analysis, we can define several terms relevant to laser gain, starting with the population inversion density ΔN , and the stimulated emission cross-section σ . The cross-section represents the effective area per excited state for interaction (transition) with an optical field. Thus, for a field with intensity I incident upon the gain medium, the net rate of transitions to the lower laser state per unit length is given by $W = (I/\hbar\omega)\sigma \Delta N$. We can also define a useful quantity, optical field energy density, as $\rho = I/c$ ([energy]/[volume]).

In order to understand time dependent gain saturation, we now consider a small segment of the gain, $\Delta\hat{z}$, as seen in Figure 2.11. The use of the hats in this and the following variable definitions pertains to simplifying future, more complicated expressions after a change of variables. With this in mind, the rate of change of the energy density in this segment is equal to the input energy flux minus the output energy flux, plus the net stimulated emission rate.

$$\frac{\partial}{\partial t}[\hat{\rho}(\hat{z}, \hat{t})\Delta\hat{z}] = \hat{I}(\hat{z}, \hat{t}) - \hat{I}(\hat{z} + \Delta\hat{z}, \hat{t}) + \sigma\Delta\hat{N}(\hat{z}, \hat{t})\hat{I}(\hat{z}, \hat{t})\Delta\hat{z} \quad (2.14)$$

In the above equation, \hat{z} and \hat{t} refer to *global* time and space coordinates, or those with respect to the laboratory. Substituting \hat{I}/c for $\hat{\rho}$ and taking the limit of (2.14) as $\Delta\hat{z} \rightarrow 0$ gives

$$\frac{\partial \hat{I}(\hat{z}, \hat{t})}{\partial \hat{t}} + c \frac{\partial \hat{I}(\hat{z}, \hat{t})}{\partial \hat{z}} = c \sigma \Delta \hat{N}(\hat{z}, \hat{t}) \hat{I}(\hat{z}, \hat{t}) \quad (2.15)$$

Additionally, given the approximations described above, we can express the change in the gain population inversion,

$$\frac{\partial \hat{N}(\hat{z}, \hat{t})}{\partial \hat{t}} = - \left(\frac{2\sigma}{\hbar\omega} \right) \Delta \hat{N}(\hat{z}, \hat{t}) \hat{I}(\hat{z}, \hat{t}) \quad (2.16)$$

The factor of 2 above arises from a consideration of properties specific to the NaCl gain medium. In a two level laser, when an atom relaxes from the upper to lower level, the net population inversion changes by 2. In NaCl, a 4-level system, lasing occurs between levels 2 and 3 (see Figure 2.3), and centers in the lower laser level then decay into the ground state. If this decay is immediate, the population inversion would only change by one for each emitted photon. If, however, this decay is slow with respect to the laser pulse, the system is said to be “bottlenecked” by the lower level, and the inversion effectively changes by two for each emitted photon. It so happens that the lower laser level decay rate for NaCl is $\sim 0.5ps$, which is

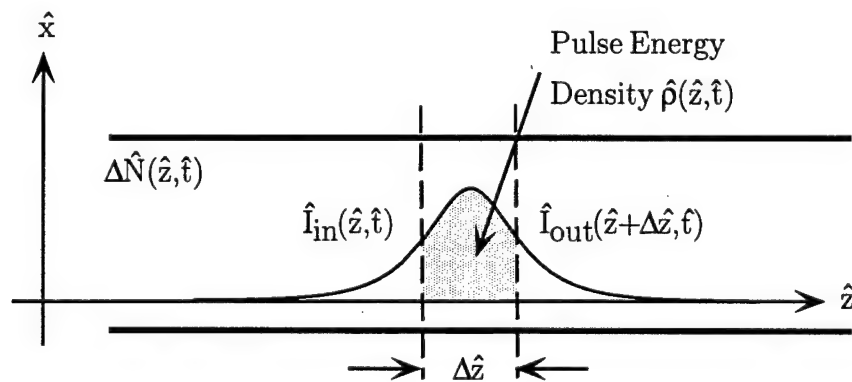


Figure 2.11: Pulse Traveling through Saturable Gain

slow compared to the typical 100fs APM laser pulse (see Section 2.5).

Solution of the two basic equations, (2.15) and (2.16), is greatly simplified with a change of coordinates. Selecting a reference frame that moves with the pulse, we define local time and space coordinates $t = \hat{t} - \hat{z}/c$ and $z = \hat{z}$, where the chain rule gives

$$\frac{\partial}{\partial \hat{t}} = \frac{\partial}{\partial t} \frac{\partial t}{\partial \hat{t}} + \frac{\partial}{\partial z} \frac{\partial z}{\partial \hat{t}} = \frac{\partial}{\partial t} \quad (2.17)$$

$$\frac{\partial}{\partial \hat{z}} = \frac{\partial}{\partial t} \frac{\partial t}{\partial \hat{z}} + \frac{\partial}{\partial z} \frac{\partial z}{\partial \hat{z}} = -\left(\frac{1}{c}\right) \frac{\partial}{\partial t} + \frac{\partial}{\partial z} \quad (2.18)$$

The intensity and population inversion can now be rewritten in terms of the new coordinate system as

$$I(z, t) = \hat{I}(\hat{z}, \hat{t}) \quad \text{and} \quad \Delta N(z, t) = \Delta \hat{N}(\hat{z}, \hat{t}) \quad (2.19)$$

In this new, local coordinate system, the basic equations (2.15) and (2.16) become

$$\frac{\partial I(z, t)}{\partial z} = \sigma \Delta N(z, t) I(z, t) \quad (2.20)$$

$$\frac{\partial \Delta N(z, t)}{\partial t} = -\left(\frac{2\sigma}{\hbar\omega}\right) \Delta N(z, t) I(z, t) \quad (2.21)$$

Rearranging, the first equation can be integrated over the length of the gain,

$$\int_{I_{in}(t)}^{I_{out}(t)} \frac{dI}{I} = \sigma \int_{z=0}^{z=L} \Delta N(z, t) dz \quad (2.22)$$

noting the limits in the left-hand side integral as the input pulse (before entering the gain), and the output pulse (after exiting the gain). Now, if we define a “total” population inversion,

$$\Delta N_{tot}(t) = \int_{z=0}^{z=L} \Delta N(z, t) dz \quad (2.23)$$

then (2.22) can be solved to yield an expression for the gain,

$$I_{out}(t) = I_{in}(t) e^{\sigma \Delta N_{tot}(t)} = G(t) I_{in}(t) \quad (2.24)$$

The second basic equation (2.21) can also be integrated over the length of the gain with the help of (2.20) and (2.23),

$$\frac{\partial}{\partial t} \int_{z=0}^{z=L} \Delta N(z, t) dz = \frac{\partial \Delta N_{tot}(t)}{\partial t} = - \left(\frac{2}{\hbar\omega} \right) \int_{z=0}^{z=L} \frac{\partial I(z, t)}{\partial z} dz \quad (2.25)$$

This further simplifies to

$$\frac{\partial \Delta N_{tot}(t)}{\partial t} = - \left(\frac{2}{\hbar\omega} \right) [I_{out}(t) - I_{in}(t)] \quad (2.26)$$

Equations (2.24) and (2.26) describe the time-dependent gain and population inversion in the local coordinate system, which can be combined as

$$\frac{\partial \Delta N_{tot}(t)}{\partial t} = - \left(\frac{2}{\hbar\omega} \right) I_{in}(t) [e^{\sigma \Delta N_{tot}(t)} - 1] \quad (2.27)$$

$$= - \left(\frac{2}{\hbar\omega} \right) I_{out}(t) [1 - e^{-\sigma \Delta N_{tot}(t)}] \quad (2.28)$$

We can rearrange (2.27) and integrate from some time t_0 before the arrival of the pulse, to time t ,

$$\int_{\Delta N_0}^{\Delta N_{tot}(t)} \frac{d\Delta N_{tot}}{e^{\sigma \Delta N_{tot}} - 1} = - \left(\frac{2}{\hbar\omega} \right) \int_{t_0}^t I_{in}(t) dt \quad (2.29)$$

where ΔN_0 is the initial population inversion of the gain,

$$\Delta N_0 = \int_{z=0}^{z=L} \Delta N(z, t_0) dz \quad (2.30)$$

The integral on the right-hand side of (2.29) is an expression for the accumulated input pulse energy per unit area, and is called the input *energy fluence*:

$$U_{in}(t) = \int_{t_0}^t I_{in}(t) dt \quad (2.31)$$

We can likewise define an output energy fluence, and a saturation energy per unit area, or *saturation energy fluence*,

$$U_{out}(t) = \int_{t_0}^t I_{out}(t) dt \quad (2.32)$$

$$U_{sat} = \frac{\hbar\omega}{2\sigma} \quad (2.33)$$

The saturation energy fluence differs from the saturation intensity by a factor of τ , the upper laser level lifetime, and the additional factor of 2, resulting from the consideration of “bottlenecking” above. Saturation fluence represents the amount of energy per unit area that must flow past a section of gain medium to reduce the gain to 1/2 its unsaturated value.

With these definitions, (2.29) can be integrated and expressed as

$$\ln \left[\frac{1 - e^{-\sigma \Delta N_0}}{1 - e^{\sigma \Delta N_{tot}(t)}} \right] = U_{in}(t)/U_{sat}(t) \quad (2.34)$$

Given the expression for the time-dependent gain, (2.24), we can re-write (2.34) as

$$\ln \left[\frac{1 - 1/G_0}{1 - 1/G(t)} \right] = U_{in}(t)/U_{sat}(t) \quad (2.35)$$

where G_0 is the initial unsaturated gain,

$$G_0 = e^{\sigma \Delta N_0} \quad (2.36)$$

The expression (2.35) can finally be rearranged to give the time-dependent gain as a function of the input energy fluence:

$$G(t) = I_{out}(t)/I_{in}(t) = \frac{G_0}{G_0 - (G_0 - 1)e^{-U_{in}(t)/U_{sat}}} \quad (2.37)$$

This gives the value of the saturable gain for any time t across the input pulse.

Considering the inclusion of this gain term into a model of the APM laser, we can make a simplification which greatly reduces the effort required to calculate the saturable gain. Since we are mainly interested in the laser output pulsewidth and energy, we can define a pulse-averaged, saturable gain which does not affect the laser pulshape. Such a simplification would not alter the dynamics of the laser, but merely neglect the pulshaping effects of the gain. This will effectively prevent the pulses from becoming asymmetric, as well as “walking” forward in time,

due to preferentially amplified leading edges. In terms of a numerical simulation with a vector pulseshape, this represents a great simplification, eliminating the need for any “re-centering” of the pulse. Moreover, since we have no easy way to experimentally observe the true, asymmetric pulseshape of a femtosecond pulse (the predominant measurement technique, pulse autocorrelation, is symmetric), we could not easily verify the results of a consideration of full gain saturation.

For these reasons, we can derive a pulse-averaged gain, starting with (2.37) and a similar equation involving $U_{out}(t)$, derived from (2.28) with the same steps used for (2.29)–(2.37):

$$G(t) = I_{out}(t)/I_{in}(t) = 1 + (G_0 - 1)e^{-U_{out}(t)/U_{sat}} \quad (2.38)$$

Defining U_{in} , U_{out} , and G_f as the corresponding time-varying quantities as $t \rightarrow \infty$, we can immediately express the pulse-averaged gain from (2.37) and (2.38) as

$$G_p = U_{out}/U_{in} = \frac{\ln \frac{G_0-1}{G_f-1}}{\ln \frac{G_0-1}{G_f-1} - \ln \frac{G_0}{G_f}} \quad (2.39)$$

With the pulse-averaged gain specified, we can now summarize the effects of the main cavity gain in the form of an operator, remembering that our APM model propagates pulse amplitudes, not intensities. Considering some main cavity pulse, $p(t)$, incident upon the gain medium, a gain operator $\hat{\mathcal{G}}$ can be defined as

$$\hat{\mathcal{G}}(p(t)) = p(t)\sqrt{G_p} \quad (2.40)$$

2.4.4 The Main Cavity: Net Model

The filtering and gain functions defined in Sections 2.4.2 and 2.4.3 correctly model the passage of a light pulse through the main cavity, but only for one pass through the gain and BTP. In order to model a complete trip through the main cavity

and thereby relate the pulses a_1 and b_1 of Figure 2.6, we must take each operator twice. In our cavity, the BTP is between the gain and the output coupler, and the high reflector is assumed to be $R = 100\%$. Starting from the output coupler in Figure 2.6, the main cavity operator which operates on b_1 to yield a_1 becomes

$$\widehat{MC} = \hat{F} \hat{G} \hat{G} \hat{F} \quad (2.41)$$

2.4.5 The External Cavity: SPM

Light from the main laser cavity is directed into an optical fiber via a beam splitter (see Figure 2.1). When the laser is well aligned, the output mode has a Gaussian profile (TEM_{00}), and the light can be optimally coupled into the fiber through the AR-coated coupling sphere and index-matching gel. Due to reflections and mode-mismatch, only a fraction of the incident intensity can generally be coupled. This fraction is referred to as the (power) coupling coefficient, γ , and is typically 50%.

A pulse launched into the optical fiber will acquire a phase chirp due to SPM. The pulse is retroreflected (see Figure 2.1) back through the fiber, and a portion returns to the main cavity. This process involves another coupling coefficient, γ_2 , and another fiber phase shift due to SPM. With a good high reflector and coupling sphere, $\sim 80\%$ of the retroreflected light can typically be coupled back into the fiber.

In order to analyze the net effect of the fiber, we start with the pulse just before the fiber, $E_0(t)$. For harmonic fields, Poynting analysis gives

$$I_0(t) = \frac{1}{2\eta} |E_0(t)|^2 \quad (2.42)$$

where η is the characteristic impedance of the medium. In air, η is given by

$$\eta = \sqrt{\frac{\mu}{\epsilon}} \approx \sqrt{\frac{\mu_0}{\epsilon_0}} = 377 \, \Omega \quad (2.43)$$

After coupling and SPM, the pulse exiting from the first pass through the fiber can be expressed as

$$E_1(t) = \sqrt{\gamma} E_0(t) e^{-j(\frac{2\pi L}{\lambda_0}) n_2 \gamma I_0(t)} \quad (2.44)$$

with corresponding intensity

$$I_1(t) = \gamma I_0(t) \quad (2.45)$$

This proportional relationship between input and output intensities is a direct consequence of the absence of dispersion in the special fiber. Now, including the second pass through the fiber, the final output pulse becomes

$$\begin{aligned} E_2(t) &= \sqrt{\gamma} \sqrt{\gamma_2} E_1(t) e^{-j(\frac{2\pi L}{\lambda_0}) n_2 \gamma_2 I_1(t)} \\ &= \gamma \sqrt{\gamma_2} E_0(t) e^{-j(\frac{2\pi L}{\lambda_0}) n_2 \gamma I_0(t)} e^{-j(\frac{2\pi L}{\lambda_0}) n_2 \gamma \gamma_2 I_0(t)} \\ &= \gamma \sqrt{\gamma_2} E_0(t) e^{-j(\frac{2\pi L}{\lambda_0}) n_2 \gamma (1+\gamma_2) I_0(t)} \end{aligned} \quad (2.46)$$

where the additional (amplitude) coupling coefficient, $\sqrt{\gamma}$, has been included to express the loss from the fiber mode coupling back into the laser mode. Note that in the limit of perfect retroreflection ($\gamma_2 \rightarrow 1$), this expression reduces to that of a single fiber doubled in length, as it should.

Together with the power reflection coefficient of the beamsplitter, R_{BS} , equations (2.42), (2.43), and (2.46) can be combined into an external cavity operator, \hat{S} , which relates a_2 and b_2 of Figure 2.6:

$$\hat{S}b_2(t) = R_{BS} \gamma \sqrt{\gamma_2} b_2(t) e^{-j\left(\Phi_0 + \frac{L 2\pi n_2 \gamma (1+\gamma_2) R_{BS} |b_2(t)|^2}{2\eta_0 \lambda_0}\right)} \quad (2.47)$$

where $b_2(t)$ is the pulse amplitude injected into the external cavity, and the static phase Φ_0 has been added to express any phase mismatch between the main and external cavities.

2.5 Numerical Model

2.5.1 Introduction

The analysis of the preceding sections has outlined a model to propagate laser pulses through an APM cavity. In particular, equations (2.8), (2.9), (2.41), and (2.47) combine with the proper inputs in an iterative model,

$$b_1^n = a_1^n \sqrt{R} + a_2^n \sqrt{(1-R)} \quad (2.48)$$

$$b_2^n = a_1^n \sqrt{(1-R)} - a_2^n \sqrt{R} \quad (2.49)$$

$$a_1^{n+1} = \widehat{MC} b_1^n = \hat{\mathcal{F}} \hat{\mathcal{G}} \hat{\mathcal{G}} \hat{\mathcal{F}} b_1^n \quad (2.50)$$

$$a_2^{n+1} = \hat{\mathcal{S}} b_2^n = \gamma k \sqrt{k_2} b_2^n e^{-j \left(\Phi_0 + \frac{L 2\pi n_2 k (1+k_2) \gamma |b_2^n|^2}{2\eta_0 \lambda_0} \right)} \quad (2.51)$$

and fully describe the round-trip pulse propagation.

In order to numerically implement these equations as a computer simulation, the laser parameters must be specified. These parameters include the initial pulse of the simulation, gain constants, and BTP filter specifications. To accurately specify model parameters, I used the output specifications of a typical NaCl APM laser [12] combined with the output beam radius determined in Section 2.2, all shown in Table 2.1.

2.5.2 The Simulation Seed Pulse

For the simulation we can use a Gaussian seed pulse, since Gaussian functions are mathematically tractable and in fact a fair approximation to the actual laser pulse shape:

$$E(t) = A e^{-2 \ln 2 (t-t_0)^2 / \delta t_0^2} \quad \text{V/cm} \quad (2.52)$$

Table 2.1: Typical NaCl APM Laser Output Specifications

Average output power	100 mW
Output beam radius	2.45 mm
Pulse repetition rate	80 MHz
Pulse width (FWHM)	100 fs
Pulse bandwidth	4.5 THz
λ_0	1.60 μm

Using (2.42) and (2.43), this becomes an expression for the pulse intensity,

$$I(t) = (A^2/2\eta_0) e^{-4 \ln 2 (t-t_0)^2/\delta t_0^2} \text{ W/cm}^2 \quad (2.53)$$

where δt_0 = full width at half maximum (FWHM). Considering a chain of such pulses as the main cavity output pulse train, the average output power can be calculated from the pulse power, averaged over one period of the pulse train, τ ,

$$P_{avg} = \frac{1}{\tau} \int_{-\tau/2}^{\tau/2} P(t) dt \text{ W} \quad (2.54)$$

where the interval τ is centered around the pulse. For the typical 80 MHz pulse train ($\tau = 12.5$ ns) and 100 fs pulses, the pulse itself accounts for only 0.0008% of the interval. Since the power dies off exponentially around the pulse center, it is safe to integrate the pulse over all time,

$$P_{avg} = \frac{1}{\tau} \int_{-\infty}^{\infty} P(t) dt = \frac{\pi(0.245\text{cm})^2}{12.5\text{ns}} \int_{-\infty}^{\infty} I(t) dt \text{ W} \quad (2.55)$$

where the output beam radius has been used to convert the pulse power to intensity.

Inserting the expression for the pulse intensity,

$$P_{avg} = \frac{\pi(0.245\text{cm})^2}{12.5\text{ns}} \int_{-\infty}^{\infty} (A^2/2\eta_0) e^{-4 \ln 2 (t-t_0)^2/\delta t_0^2} dt \quad (2.56)$$

$$= \frac{\pi(0.245\text{cm})^2 A^2}{2 \eta_0 12.5\text{ns}} \sqrt{\frac{\pi \delta t_0^2}{4 \ln 2}} \text{ W} \quad (2.57)$$

From Figure 2.1, we see that the average intracavity power is the average output power divided by both the output coupler and external cavity beam splitter power transmission coefficients, or $P_{out}/P_{cav} = R R_{BS}$, since the laser radiation must pass through both of these mirrors to be output. Together with the values for η_0 and δt_0 , and the other laser parameters from Table 2.1, we arrive at the pulse field amplitude factor,

$$A = \left(\frac{2 \eta_0 12.5 \text{ns } 667 \text{mW}}{\pi (0.245 \text{cm})^2} \sqrt{\frac{4 \ln 2}{\pi \delta t_0^2}} \right)^{1/2} = 17.7 \text{ kV/cm} \quad (2.58)$$

One should note that this amplitude factor applies to the *free-space* intracavity field. Thus, in expressing the input field to the gain or the optical fiber (external cavity) operators defined in Section 2.4, I must take into account their different (and much tighter) beam waists. From Figure 2.2, we see that the beam radius inside the gain medium is $\approx 10.4 \mu\text{m}$. Thus, the ratio of the pulse intensity inside the gain to the free-space intracavity intensity is

$$\frac{I_{gain}}{I_{FS}} = \frac{(0.245 \text{cm})^2}{(10.4 \times 10^{-4} \text{cm})^2} = 55.5 \times 10^3 \Rightarrow \frac{E_{gain}}{E_{FS}} = 236 \quad (2.59)$$

Similarly, the field inside the optical fiber, which has a $10 \mu\text{m}$ core diameter, will be much higher.

$$\frac{I_{fiber}}{I_{FS}} = \frac{(0.245 \text{cm})^2}{(5 \times 10^{-4} \text{cm})^2} = 240 \times 10^3 \Rightarrow \frac{E_{fiber}}{E_{FS}} = 490 \quad (2.60)$$

2.5.3 Gain Constants

Section 2.3.1 discussed the structure and properties of the NaCl gain medium. The $\text{F}_2^+:\text{O}_2^-$ defect has been studied in detail, and has the laser parameters listed in Table 2.2 [13, 10, pp. 20–21], where the τ_n parameters represent the energy level lifetimes shown in Figure 2.3.

Table 2.2: Laser Gain Parameters

Center	λ_0 (μm)	τ_1 (psec)	τ_2 (nsec)	τ_3 (psec)	$\Delta\nu$ (THz)	σ (10^{-16}cm^2)	I_{sat} (kW/cm^2)
$\text{F}_2^+:\text{O}_2^-$	1.6	0.5	160	0.5	45	0.9	9.0

From Tables 2.1 and 2.2, we see that the pulse bandwidth accounts for only 10% of the gain linewidth, and in the presence of the much narrower BTP linewidth, we can neglect the gain's dependence on frequency. The gain is thus adequately modeled by (2.37), and only the parameters G_0 and U_{sat} remain to be determined.

Given the values for σ and λ_0 , we can proceed to calculate the saturation fluence from (2.33):

$$U_{sat} = \frac{hc/\lambda}{2\sigma} = 690 \mu\text{J}/\text{cm}^2 \quad (2.61)$$

In order to determine the steady-state, unsaturated gain coefficient, G_0 , we must take into account both the gain and loss mechanisms of a pulse. A pulse $I(t)$ traveling through the main cavity will experience the saturable gain twice, then the output coupler loss before returning to its original position. In order to have a steady state, the power gained by the pulse per round trip must equal the power lost, i.e., the output power. Considering a pulse $I_{in}(t)$ embarking upon two gain passes,

$$I_{out}(t) = \hat{\mathcal{G}}\hat{\mathcal{G}} I_{in}(t) \quad (2.62)$$

Additionally, we must remember that the beam radius in the gain is tighter than the free-space radius. Using (2.59), we can relate the gain input pulse to the free-space input, as well as the free-space output pulse to the gain output, to obtain

$$I_{out,FS}(t) = \frac{1}{55.5 \times 10^3} \hat{\mathcal{G}}\hat{\mathcal{G}} [55.5 \times 10^3 I_{in,FS}(t)] \quad (2.63)$$

where $I_{in,FS}$ is just the simulation seed pulse, given by (2.53) and (2.58). Since we

know the average output power of the NaCl APM laser, we can use an expression like (2.54) to calculate the free-space averages \tilde{I}_{out} and \tilde{I}_{in} . Then, the power gained is given by

$$\left(\frac{\text{output beam}}{\text{area}} \right) \times (\tilde{I}_{out} - \tilde{I}_{in}) = \pi(0.245\text{cm})^2 (\tilde{I}_{out} - \tilde{I}_{in}) \quad (2.64)$$

In this manner, the expression (2.64) depends only upon G_0 , and when equated with the average main cavity output power, will determine G_0 uniquely. It is important to note that the average output power listed in Table 2.1 (100 mW) is the total APM output power, meaning that the main cavity output power used to evaluate (2.64) is this value divided by the beamsplitter transmission coefficient, $1 - R_{BS}$.

Since the operator $\hat{\mathcal{G}}$ is a complex function of the input intensity, (2.63) is most easily solved numerically with a computer. Doing this calculation and equating the resulting power gained with the average main cavity output power, I arrive at the value of G_0 for my numerical model,

$$G_0 = 1.76 \quad (2.65)$$

2.5.4 BTP Filter Specifications

From the analysis of Section 2.4.2, we have an expression for the transmitted intensity of the birefringent tuning plate versus wavelength, (2.10). The indices of refraction for crystalline quartz are given in several references [14], and for $\lambda = 1.5414$, $n_o = 1.52781$ and $n_e = 1.53630$. The parameter θ was already specified in Section 2.4.2 as Brewster's angle, or $\theta = 56.8^\circ$. The only remaining parameters in the BTP specification are ϕ , the rotation of the plate (see Figure 2.7), and t , the plate thickness.

Typically, the plate thickness ranges from 0.5–5 mm, depending upon the desired output pulse width, where thicker plates yield longer pulses, from (2.10). Because several other parameters, including the coatings of the optics used in the particular laser, combine with the BTP to determine the ultimate pulsewidth, the thickness used experimentally may not match the theoretical value. We can use 1.75 mm for the numerical model of this thesis, since it falls in the typical experimental range, and the simulations of Chapter 4 will show that this thickness yields ~ 100 fs pulses.

To determine the proper value of ϕ , we must examine (2.10). Adjusting ϕ will essentially alter the center wavelength of the laser, by altering the zero-loss wavelength of the BTP. From (2.10), we see that two conditions will cause $I_T(\lambda) = 0$: either $\phi = (m\pi/2)$, or the quantity in parenthesis being an integral multiple of π . The first of these will cause $I_T(\lambda) = 0$ for all λ , and is therefore not useful. The second condition can be written as

$$\frac{t}{\lambda} \left\{ \frac{n_e [1 + \cos^2 \theta \cos^2 \phi \left(\frac{1}{n_e^2} - \frac{1}{n_o^2} \right)]}{[1 - \cos^2 \theta \left(\frac{\sin^2 \phi}{n_e^2} + \frac{\cos^2 \phi}{n_o^2} \right)]^{1/2}} - \frac{n_o}{[1 - \frac{\cos^2 \theta}{n_o^2}]^{1/2}} \right\} = m \quad (2.66)$$

where m is an integer. With all other quantities specified ϕ can easily be determined with a computer. For $t = 1.75$ mm, the only valid m is 8, meaning that the BTP can tune over only ~ 1 “order” in the neighborhood of $\lambda = 1.60\mu\text{m}$. Using $m = 8$, we find $\phi = 48.0^\circ$.

Thus, the model BTP is completely specified, and the transmission response versus wavelength completely known. All of the BTP parameters are summarized in Table 2.3.

In specifying the initial simulation pulse, gain constants, and BTP parameters, we have completed the numerical model (2.51) for the APM laser. Chapter 4 will use this model to simulate both steady-state APM behavior, and APM nonlinear

Table 2.3: Model BTP Parameter Specifications

n_o	n_e	t mm	θ °	ϕ °
1.52781	1.53630	1.75	56.8	48.0

dynamics. First however, Chapter 3 will discuss the study of nonlinear dynamics, and introduce valuable graphical and quantitative techniques to characterize system dynamics.

Chapter 3

An Overview of Nonlinear Dynamics and Chaos

3.1 Nonlinear Differential Equations and Phase- plane Analysis

The discovery of strange attractors, chaos, and even fractals originated in the study of weather, which involved a simple set of nonlinear differential equations. Since the original discoveries, chaotic behavior has been found in even the most basic of mathematical systems. Indeed, most processes in the real world are inherently nonlinear at some level, but the lack of good mathematical tools for handling such equations has historically encouraged mathematicians and engineers alike to make linear approximations. Take, for example, the simple pendulum problem from introductory physics. The full description of the pendulum comes from Newton's Second Law, $F = ma$, where the governing force (due to gravitation) is tangent to

the pendulum. Thus, we have

$$mL\ddot{\theta} = -mg \sin \theta \quad \Rightarrow \quad \ddot{\theta} + \frac{g}{L} \sin \theta = 0 \quad (3.1)$$

for a pendulum of length L and mass m , where θ is the angular displacement of the pendulum arm from vertical. This can be re-written as the following set of first-order, coupled differential equations

$$\dot{\theta}_1 = \theta_2 \quad (3.2)$$

$$\dot{\theta}_2 = -\frac{g}{L} \sin \theta_1 \quad (3.3)$$

Although they look simple, these equations are nonlinear and require significant effort to be solved analytically. Traditionally, the equations are linearized by assuming the pendulum's excursions from vertical (rest) are small, and thus $\sin \theta_1 \approx \theta_1$.

Although nonlinear systems of equations are difficult to solve analytically, a qualitative, graphical approach generally yields the important behaviors of the system, while keeping the problem tractable. The approach commonly used, called *phase-plane* analysis, involves graphing system variables against their derivatives (such as position and velocity). Thus, one avoids actually solving the system of differential equations, and with correct interpretation, can determine general and even limiting system behaviors.

For an example, we can study the so-called logistic equation,

$$\dot{x} = rx \left(1 - \frac{x}{K}\right) \quad (3.4)$$

This equation was originally used to describe biological populations, where r is the growth rate, and K the carrying capacity. Figure 3.1 shows a graph of \dot{x} versus x , where the velocity is positive for all $x < K$, negative for all $x > K$, and zero for $x = 0$ or $x = K$. Figure 3.2 demonstrates these movements by superimposing

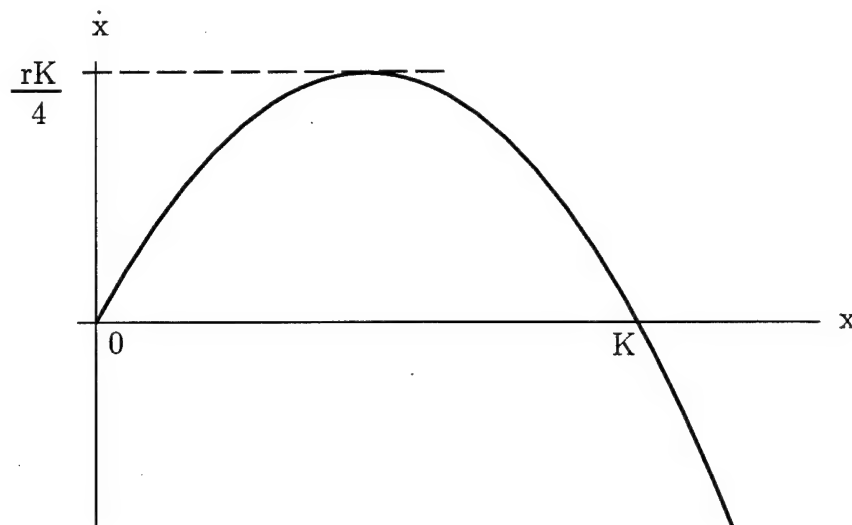


Figure 3.1: Graphical Analysis of the Logistic Equation

arrows on the x -axis in the direction of the velocity. Thus, starting with either $x < K$ or $x > K$, we see that x will move toward K . In this manner, K is easily identified as a fixed point of the system. This can also be seen by the fact that the velocity at $x = K$ is zero, so a system with $x = K$ will remain there indefinitely. $x = 0$ is also a fixed point, but since a small perturbation away from this point will yield a positive velocity (away from $x = 0$), it is an *unstable* fixed point, whereas $x = K$ is *stable*. This analysis can give a good qualitative picture of the actual time evolution of x , or the *trajectory*. Trajectories starting at the fixed points will remain at the fixed points; any other starting value will end up at $x = K$. This behavior is summarized by Figure 3.3. Moreover, the phase portrait in Figure 3.2 indicates that, for x values starting below $K/2$, the velocity will initially increase, then decrease before reaching the stable value of K . These velocity gradients translate to different concavities in the actual trajectories, as seen for initial values below $K/2$ in Figure 3.3.

Since a trajectory is a solution to a system of nonlinear differential equations,

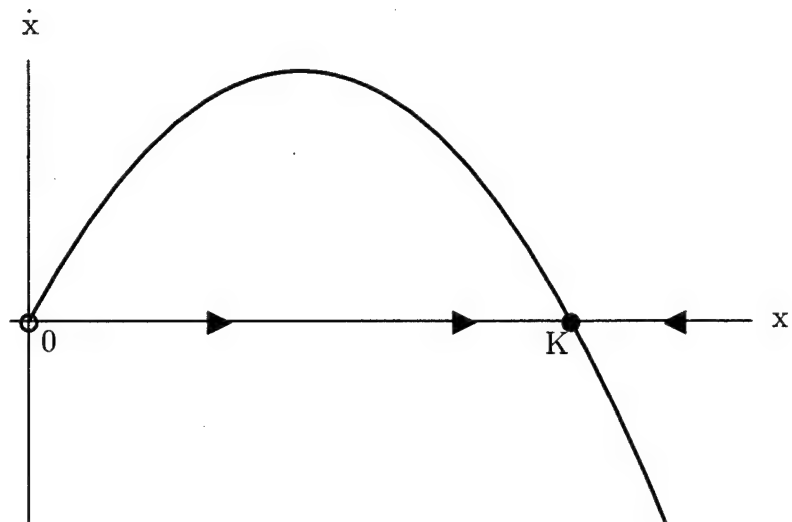


Figure 3.2: Graphical Interpretation of the Logistic Equation

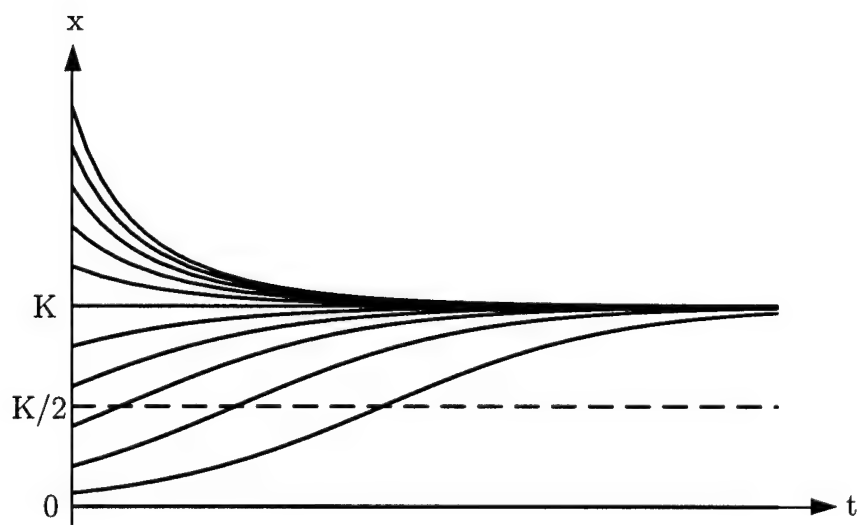


Figure 3.3: Logistic Equation Trajectories

certain existence and uniqueness theorems can be applied. For a large class of autonomous systems (systems without a time-dependent forcing) like the logistic equation above, the uniqueness theorem specifies that there can be only one solution to the system at each point in space [15]. Consequently, trajectories cannot intersect. For one-dimensional systems, this means that dynamics are relatively simple since every trajectory must flow monotonically toward or away from a fixed point. No oscillations are even possible, since this would necessitate overlapping trajectories.

Much more complicated dynamics can arise in higher dimensional systems. Two such cases are limit cycles (stable periodic orbits) and quasiperiodicity. Quasiperiodicity is a “combination oscillation” characterized by two, incommensurate frequencies. In this case, the orbit in phase space never closes upon itself, but wraps around indefinitely. Quasiperiodicity is often visualized as a trajectory orbiting around the surface of a torus, where the two characteristic circumferences are proportional to the two oscillation frequencies.

3.2 Bifurcations

Many experimental systems can exhibit several radically different behaviors, based upon certain control parameters. For example, pumping a laser either above or below threshold will result in totally different output. Altering this one parameter, i.e. the pump power, causes a change in the system. When a system’s dynamical behavior changes, it is said to have undergone a *bifurcation*. The varying parameter that causes the change is called the bifurcation parameter, and the value of this parameter where the change occurs is called the bifurcation point. The bifurcation point for the laser above is the threshold pumping level. More technically, the

system is not stable at the bifurcation point, since a perturbation in either direction would cause different dynamical system behavior.

Implicit in this description is a consideration of the stability of fixed points. In the case of a laser, there are two fixed points: off (no laser oscillation), and on (laser output, which follows some kind of output power versus pumping curve). Below threshold pumping, the "off" fixed point is stable and the "on" fixed point is unstable; above threshold pumping, the situation is reversed. To demonstrate this mathematically, consider a simplified laser model where p represents the number of photons in the laser mode. The change in this number for steady state can be represented by the gain minus the loss,

$$\dot{p} = \alpha N p - \beta p \quad (3.5)$$

where N is the population of the upper lasing level, and α and β are simply proportionality constants. Thus, the first term represents gain proportional to the population in the upper lasing level, and the second term is the round-trip cavity loss. Normally in steady state, (3.5) would be zero, but a varying pumping level will adiabatically change the value of the gain with respect to steady-state laser oscillation. The population of the upper lasing level can in turn be expressed as the steady-state population due to pumping, N_0 , minus a contribution to the steady-state laser mode which is proportional to the number of photons p in this mode, or

$$N = N_0 - \gamma p \quad (3.6)$$

where γ is related to the stimulated emission rate. Thus, the expression for p becomes

$$\dot{p} = (\alpha N_0 - \beta) p - \alpha \gamma p^2 \quad (3.7)$$

To obtain the fixed points, we set $\dot{p} = 0$, and find

$$p = 0 \quad \text{or} \quad p = \frac{-\beta}{\alpha\gamma} + \frac{1}{\gamma} N_0 \quad (3.8)$$

To determine the stability of these fixed points, we examine the graph of \dot{p} versus p for different values of pumping, N_0 , shown in Figure 3.4 (a)–(c). For $N_0 < \beta/\alpha$, the fixed point at the origin is stable and the other is unstable. For $N_0 = \beta/\alpha$, the two fixed points coalesce at the origin, and both are only *half stable*. For $N_0 > \beta/\alpha$, the graph looks much like the logistic equation in Figure 3.2, where the origin is unstable, and the fixed point at $p = \frac{-\beta}{\alpha\gamma} + \frac{1}{\gamma} N_0$ is stable. The results of this type of analysis are conveniently summed up with the bifurcation diagram in Figure 3.5, which plots p versus the bifurcation parameter, N_0 . The stable operating points are indicated by solid lines, the unstable are dashed, and the bifurcation point is easily identified as $N_0 = \beta/\alpha$, the value at which the two fixed points exchange stability. Being a simplistic laser model, it is not surprising that this figure looks just like the classic plot of output power versus pump power for an ideal laser.

The bifurcation shown in Figure 3.5 is more commonly known as a transcritical bifurcation. Numerous other types of bifurcations are possible, depending upon the number of fixed points in question, whether fixed points are created or destroyed during a bifurcation, the dimensionality of the system, and even symmetry considerations. Regardless of the type of bifurcation, the importance of the bifurcation diagram lies in its clear presentation of the different dynamical regions of operation for a system as some parameter is varied. Technically, a bifurcation diagram displays both stable and unstable orbits, as in Figure 3.5, but one more commonly encounters diagrams without the unstable orbits, under the same name. Although this special case is referred to as an *orbit* diagram, we can use the more common term, bifurcation diagram.

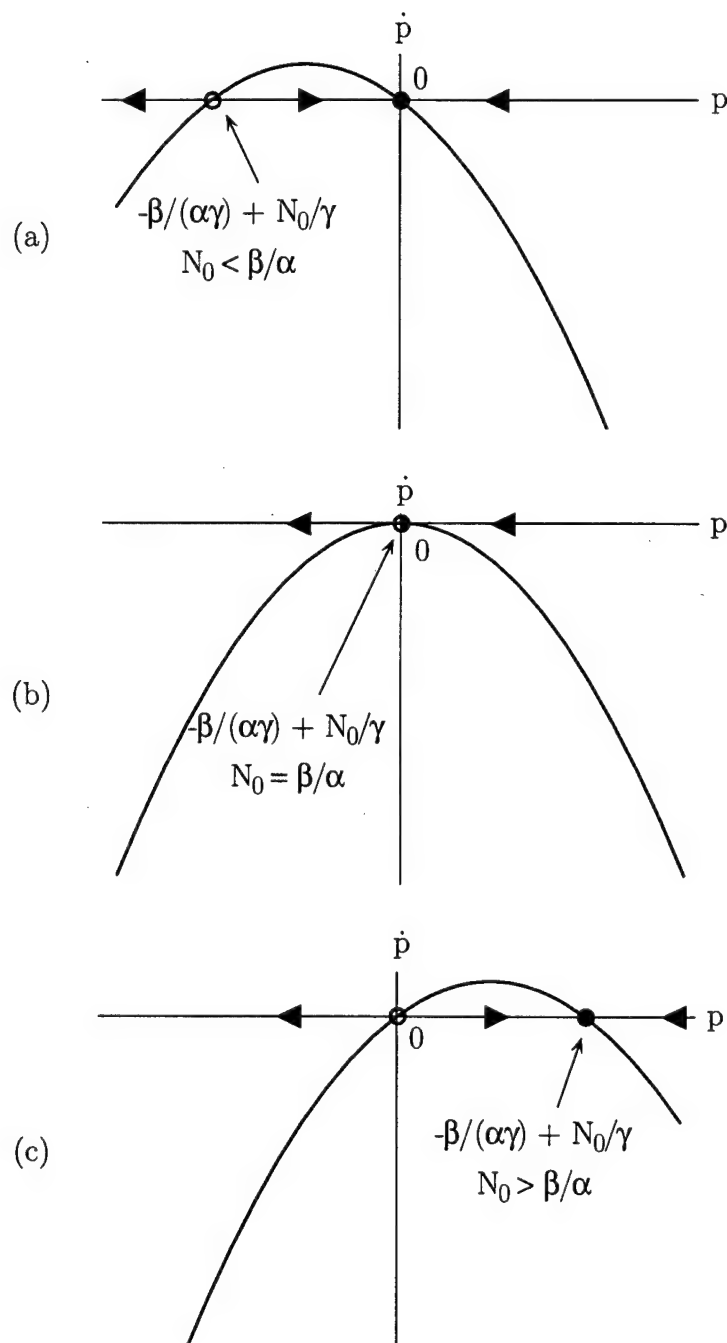


Figure 3.4: Simple Laser Fixed Point Stability Analysis (a) $N_0 < \beta/\alpha$ (b) $N_0 = \beta/\alpha$ (c) $N_0 > \beta/\alpha$

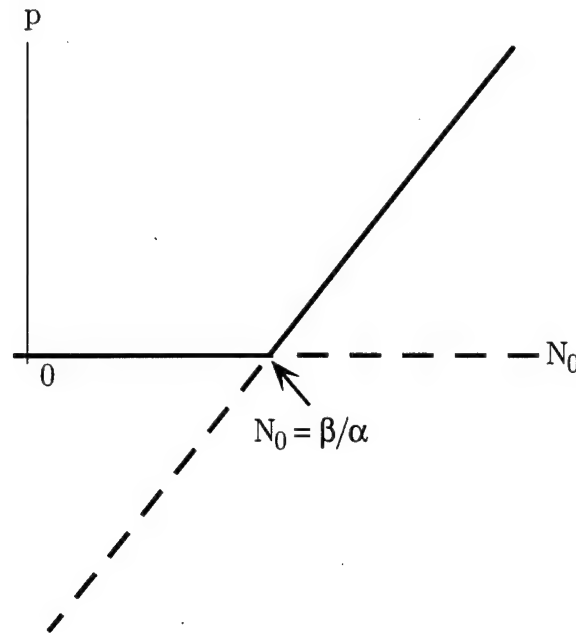


Figure 3.5: Bifurcation Diagram for Simplified Laser

Most interesting systems studied today contain more than just stable fixed points. Stable periodic orbits are desired for numerous purposes in communication or laser systems. Like fixed points, periodic orbits can also experience bifurcations, being created, destroyed, or simply changing stability. This is an important point to keep in mind when studying such a complex system as the APM laser.

3.3 Chaos

3.3.1 Introduction

In the long history of nonlinear systems analysis, the phenomenon of chaos has only recently come to light. So new and complex is the behavior, the precise mathematical definition of 'chaos' has yet to be established. In spite of this, however, certain properties of chaotic systems have been agreed upon:

- 1) Chaos is an extremely complex, seemingly random, yet entirely deterministic behavior of a system in response to known, noiseless inputs.
- 2) All chaotic systems exhibit a sensitive dependence on initial conditions, where two arbitrarily close trajectories in phase space will exponentially diverge over time.
- 3) In a chaotic system, trajectories are aperiodic, and do not reduce to fixed points, limit cycles, or quasiperiodic orbits as $t \rightarrow \infty$.

Together with the discovery of chaos was the identification of the *strange attractor*, or the very complex, stable phase-space structure to which most trajectories converge in a chaotic system. The existence of such a structure reveals another subtle difference between chaotic and stochastic orbits: a purely random orbit would eventually visit every point in phase space, while a chaotic orbit remains confined to the attractor.

3.3.2 The Lorenz System

A good example of chaos and the strange attractor comes from the Lorenz equations, studied by Ed Lorenz in 1963 [16], to model convection rolls in the atmosphere. Without touching on the physical interpretation of the equations, the system is given by

$$\begin{aligned}
 \dot{x} &= \sigma(y - x) \\
 \dot{y} &= rx - y - xz \\
 \dot{z} &= xy - bz
 \end{aligned}
 \tag{3.9}$$

The constants σ , r , $b > 0$ are parameters of the system. In studying these equations, Lorenz performed transformations, identified fixed points, and did stability

analyses for different values of the parameters. For certain ranges of values, he proved that the trajectories did not exhibit limit cycle or fixed point behavior, yet they remained bounded within a finite volume. This apparent paradox was somewhat explained when Lorenz integrated the equations numerically, and plotted the solutions in xyz space, shown in Figure 3.6.

Many remarkable features arise from this strange attractor, most notably that the structure is indeed limited in volume. Lorenz proved that his attractor not only has finite volume, but it in fact has no volume. Since the Lorenz system is also autonomous, this requires that no two trajectories intersect, yet each must still remain within a finite (zero) volume. These facts led Lorenz to deduce that his attractor was actually an infinite complex of surfaces, wrapping around phase space in a folding motion. An alternate view of the attractor (the x - z plane) in Figure 3.7 shows some more detail of this interleaving surface type of structure. This particular view inspired the name "Butterfly Attractor".

To demonstrate the feature of sensitive dependence on initial conditions which is unique to chaos, Figure 3.8 shows the time development of 1000 nearby initial conditions in the Lorenz system. A portion of the Lorenz attractor is superimposed on the initial conditions in each frame, as a reference. The different conditions initially appear to move in a similar manner, but rapidly diverge so that in a small amount of time the resulting orbits could be virtually anywhere on the attractor. Even quasiperiodic systems do not display such sensitive dependence: should two, nearby initial conditions propagate forwards in time, neither will form a closed orbit (loop) in phase space, but they will retain their proximity for all future times.

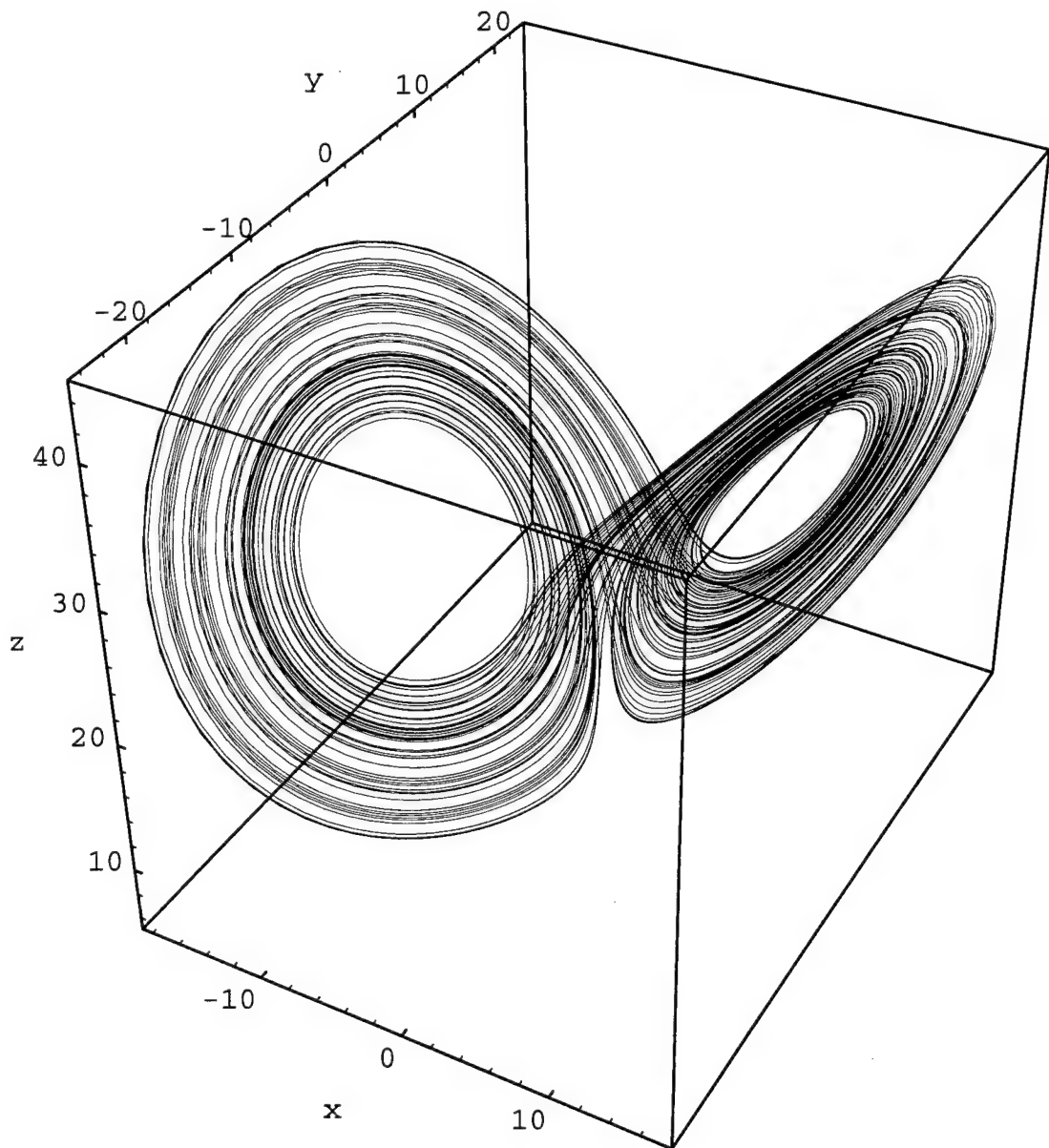


Figure 3.6: The Lorenz System Strange Attractor

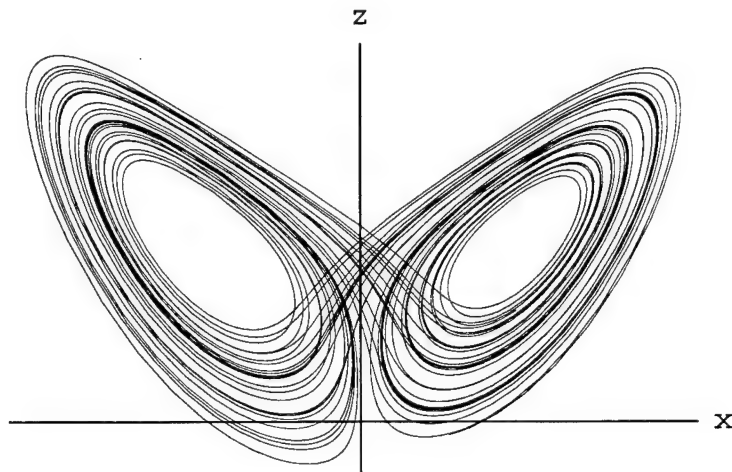


Figure 3.7: The x-z Lorenz Attractor

3.3.3 Lyapunov Exponents

Despite the beauty of the Lorenz attractor and all of the graphical analysis performed above, we still have yet to present any quantitative approach to identifying or characterizing chaos. Since one of the universally accepted criterion for identifying chaos is the feature of sensitive dependence on initial conditions, this would seem a good starting point for quantification. More specifically, sensitive dependence means that nearby trajectories will exponentially diverge over locally short times, in the form

$$\delta(t) = \delta_0 2^{\lambda t} \quad (3.10)$$

where δ is the distance between two nearby trajectories after time t , as shown in Figure 3.9. In (3.10), λ is known as the *Lyapunov exponent*, which is a measure of the predictability of the system. The choice of base 2 gives the appropriate units of bits/second, the rate at which information is lost. This means that a system with initial conditions measured to n bits of precision will be completely unpredictable after a time of $t \sim n/\lambda$. In general, most systems are characterized by several Lyapunov exponents, depending upon the dimensionality of the system. The signs

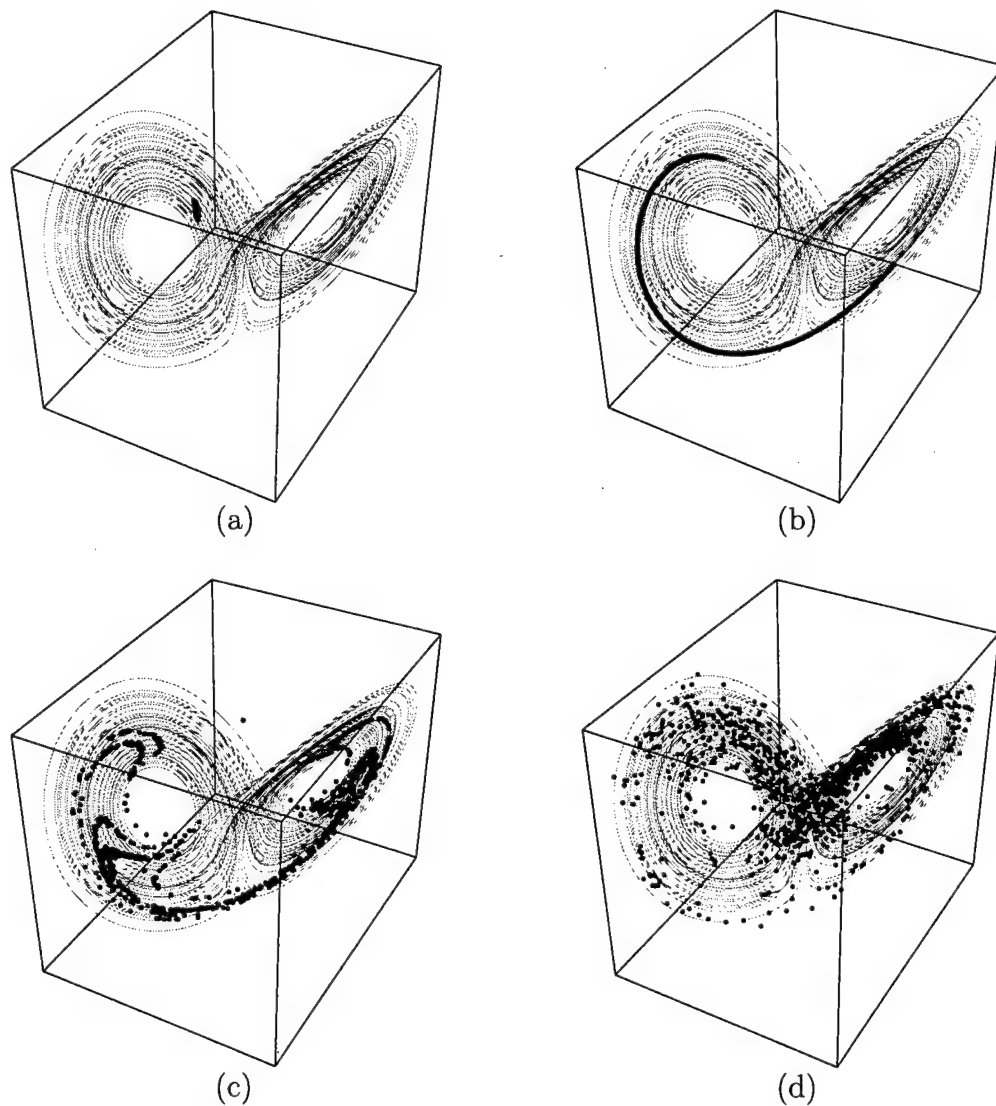


Figure 3.8: The Time Evolution of 100 Nearby Initial Conditions in the Lorenz System (a) $t = 1$ and the orbits seem to track each other fairly well (b) $t = 3$ and the orbits have separated into a long tail (c) $t = 6$ and several different groupings of outcomes are apparent (d) $t = 10$ and any one initial orbit could be anywhere on the attractor (inspired by a similar figure in Strogatz [17])

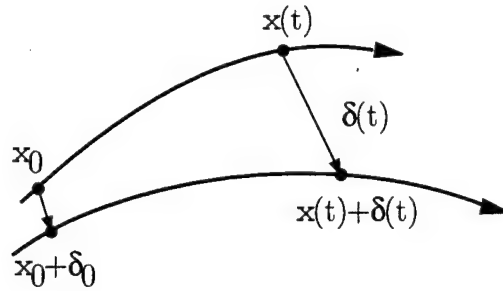


Figure 3.9: The Divergence of Nearby Trajectories

of the largest exponents indicate either converging ($\lambda < 0$), periodic ($\lambda = 0$), or chaotic ($\lambda > 0$) behavior. Although dissipative chaotic systems require at least one exponent in each of these regions ($\lambda > 0$ in the direction of chaotic exponential divergence, $\lambda = 0$ along the trajectory, and $\lambda < 0$ in the direction responsible for keeping the size of the attractor finite), only one positive exponent is required to exhibit chaos.

There are several analytical methods for determining a system's Lyapunov exponents, but many require prior knowledge of the differential equations governing the trajectories. Furthermore, not all exponents need to be determined to deduce chaotic behavior, only the largest one. A simple method to find this exponent uses the actual time evolution of two nearby trajectories. We begin with some trajectory on the chaotic attractor, and observe another nearly identical trajectory. The distance between these two should be quite small, on the order of $10^{-50}\%$ of the overall trajectory extent if possible. Next, we propagate both states forward in time, recording their relative distance. We can now plot the \log_2 of the distance $\|\delta(t)\|$ between the two trajectories versus time, and fit a line whose slope reveals the Lyapunov exponent.

As an example of such a calculation, the Lorenz system of Section 3.3.2 yields the logarithmic distance plot shown in Figure 3.10. The meandering of the dis-

tance function during its upward trend results from considering only one Lyapunov exponent when in fact, the trajectories move in more than one dimension. Also, the graph reaches a plateau, which is simply a consequence of the finite size of the attractor: two trajectories can only move as far apart as roughly the “diameter” of the attractor. Ignoring this plateau, the line fit to the graph indicates an exponent of 1.03, which is quite close to other published calculations [17].

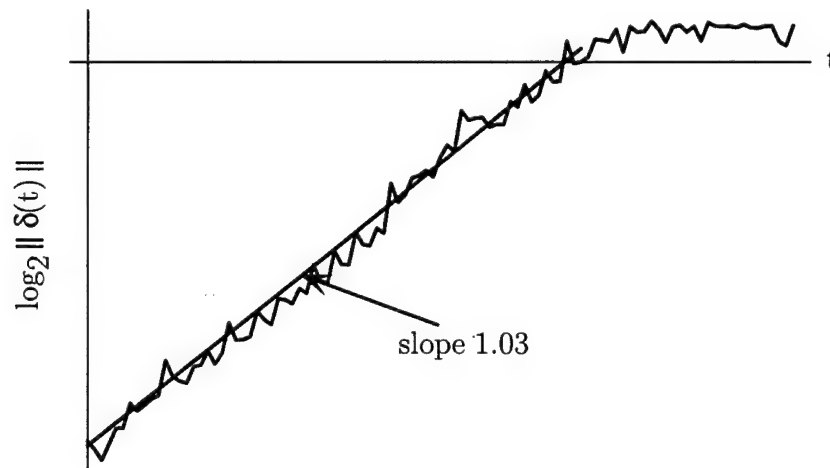


Figure 3.10: Calculation of the Largest Lyapunov Exponent for the Lorenz Attractor, derived from the slope of the $\log_2 \|\delta(t)\|$ vs. t curve

One must keep in mind that this calculation is local to a specific region of phase space, however, and because Lyapunov exponents are global properties of an attractor, this simplified technique will not in general represent the true Lyapunov exponent. Section 3.4.4 will discuss a better method to determine the largest Lyapunov exponent. In properly calculating a positive largest exponent, one can show convincing evidence of the existence of chaos.

3.4 Iterative Maps, Fractal Dimension, and Lyapunov Exponent Estimation

3.4.1 The Logistic Map

Up to this point, the treatment of nonlinear dynamics has assumed that the systems in question are continuous. That is, the system is governed by set of first-order nonlinear differential equations, and the trajectories are therefore continuous flows. Another class of problems involves discrete time, which can result from a logical necessity to treat time in discrete units, or simply from the construction of iterative mappings. Mappings involve a set of transformation rules to take the system from a current state to the next. A simple but dynamically rich example is the logistic map, which bears obvious resemblance to the logistic equation (3.4),

$$x_{n+1} = rx_n(1 - x_n) \quad (3.11)$$

For a given value of the parameter r , an input of x_n will yield some output x_{n+1} . Applying the mapping iteratively to this and successive outputs will generate a series of values which, assuming each iterate is offset in time, forms a discrete time series of data. This type of interpretation directly applies to the model of the additive-pulse modelocked laser developed in Chapter 2.

Considering the logistic map (3.11), we can first observe that restricting the domain x_n to $[0,1]$ and r values to $[0,4]$ will force (3.11) to map onto itself. To explore the map's behavior under these assumptions, we can begin with $r = 2$ (r values between 0 and 1 are uninteresting, as they iteratively contract the map to zero). Choosing a value of x_0 , say 0.2, we iterate the map several (100) times to allow any initial transients die out. Next, we observe the map output for several

subsequent iterations, shown in Figure 3.11. The map has settled into a constant value, which is often referred to as period-one behavior, since one iteration can be taken as one period. The line connecting the points in Figure 3.11 merely serves to aid the eye, since the map provides discrete data.

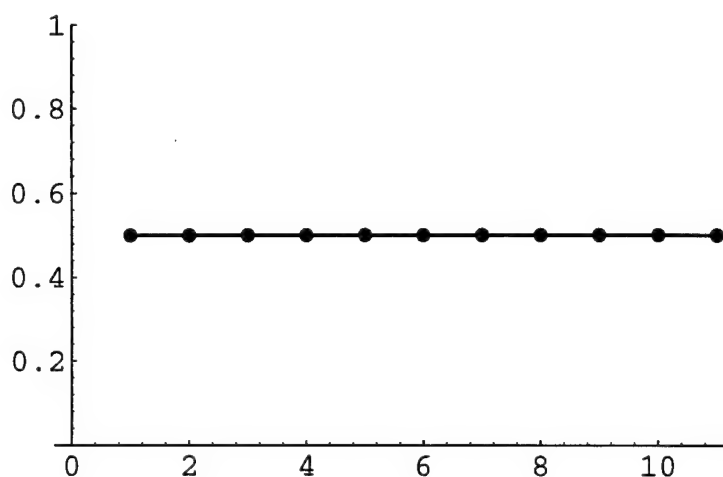


Figure 3.11: The Logistic Map Exhibiting Period-One Behavior: $r = 2$, $x_0 = 0.2$

Choosing the larger value of 3.3 for r , we see markedly different behavior. Figure 3.12 shows that the map has settled into a stable period-two cycle. Increasing the r value a bit more to 3.5, we see another period-doubling to period-four, shown in Figure 3.13.

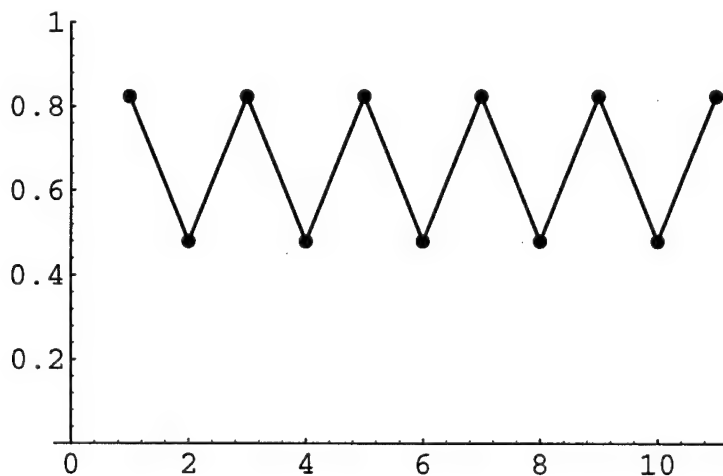


Figure 3.12: The Logistic Map Exhibiting Period-Two Behavior: $r = 3.3$

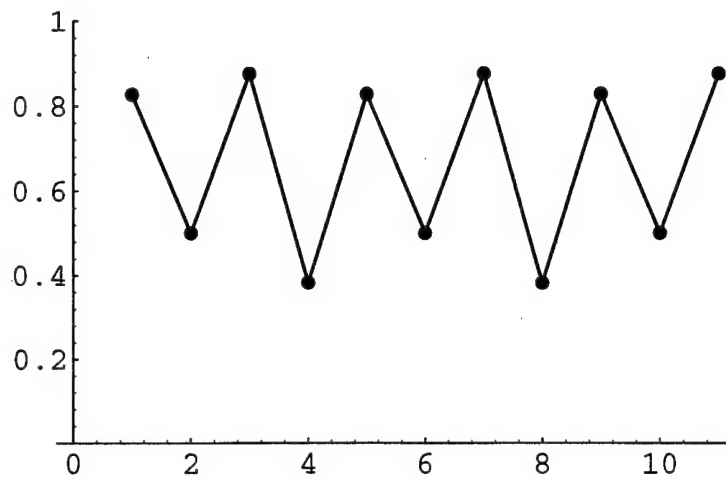


Figure 3.13: The Logistic Map Exhibiting Period-Four Behavior: $r = 3.5$

With such rapid changes in system dynamics, a bifurcation diagram can greatly simplify the analysis as the parameter r varies. To construct such a diagram for a map, one proceeds as above for Figures 3.11–3.13, performing the sequence of preiterations for each new value of r , then plotting 20 or so iterations (x_{n+1}) before re-modifying r . The result in the case of the logistic map is both complex and beautiful, shown in Figure 3.14.

The evolution of the logistic map as r is increased is referred to as the period-doubling route to chaos. The system begins in period-one, then doubles to period-two, four, eight, and so on until it becomes chaotic around $r = 3.57$. This chaotic region is characterized by what appears to be a noisy smear on the bifurcation diagram. Although no proof of chaos for the logistic map is given here, a positive Lyapunov exponent can be determined analytically [17].

The logistic map bifurcation diagram also reveals much more than just several period-doublings and a chaotic region. For instance, there is a large window of period-three behavior located around $r = 3.84$, signifying the existence of stable oscillations in the very midst of chaotic parameter space. One may also note that each of the period three orbits period doubles in the same manner as the overall

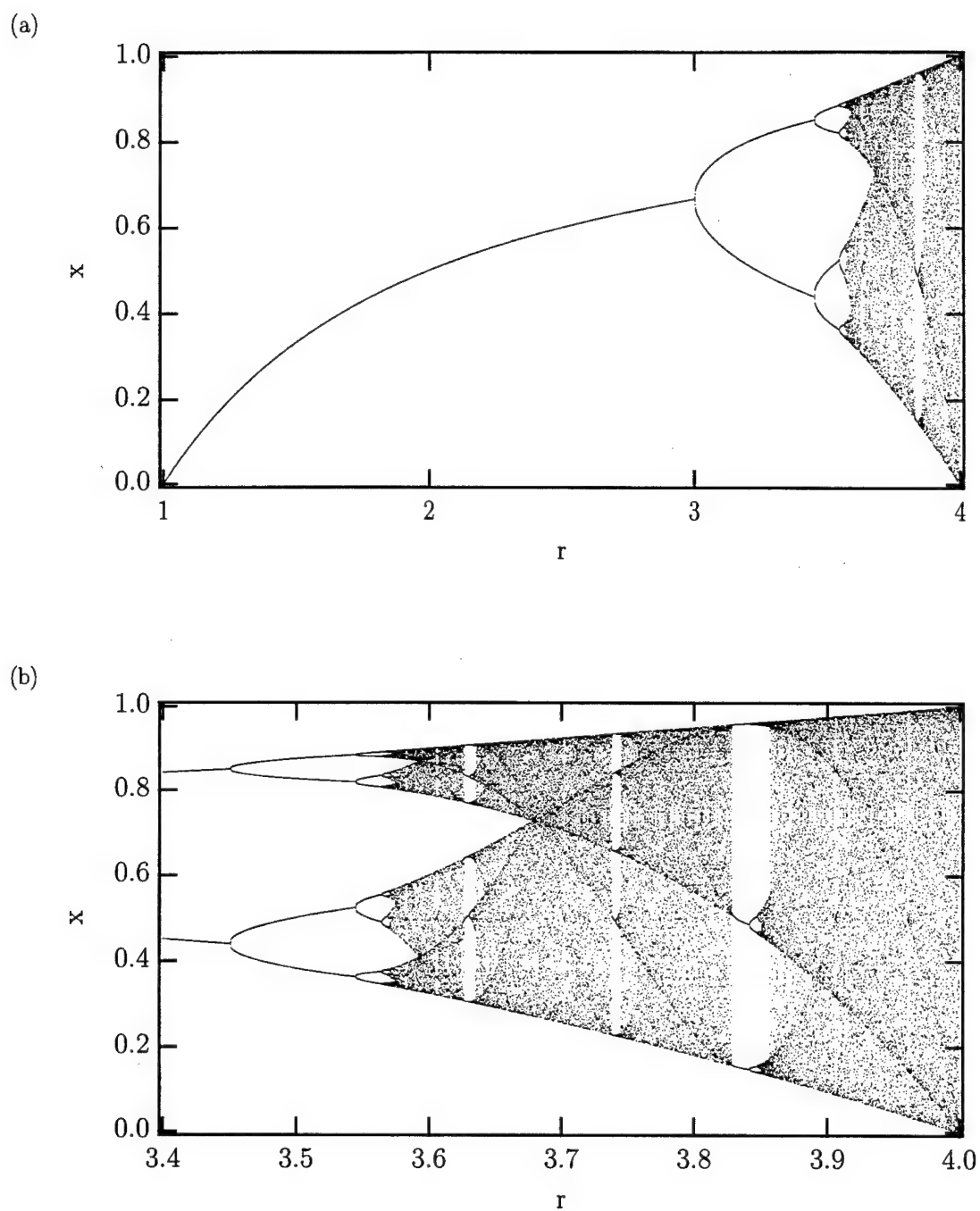


Figure 3.14: The Logistic Map Bifurcation Diagram, shown in (a) full-scale and (b) a closeup of the period-doubling and chaotic regimes

map, in fact producing exact replicas of the original figure. This observation reveals the feature of self-similar structure, a characteristic of chaos, since strange attractors are inherently fractal in nature. Section 3.4.2 will discuss fractal dimension, which is one of the identifiers and quantitative measures of fractal objects.

3.4.2 Fractal Dimension

The logistic map raises several issues about the nature of fractals and their relationship to chaos, especially the question of dimension. If a fractal structure is truly self-similar, then we could examine successively smaller and smaller portions of the structure, uncovering the same detail at each iteration. Measuring the physical dimension of the structure then seems a formidable task.

Starting from a simpler level, we can first consider the physical properties of more easily defined geometrical objects. A line of length L which occupies one-dimensional Euclidean space can be divided into n equal parts, each of length $l = L/n$. The smaller pieces are exact copies of the original line scaled by a factor $s = l/L = 1/n$. Likewise, a square occupies two dimensions, and can be divided into n equal squares scaled by a factor $s = l/L = 1/\sqrt{n}$, while a cube in three dimensions becomes n equal cubes scaled by a factor $s = 1/\sqrt[3]{n}$. Thus, the dimension D of the original object helps to relate the number of self-similar structures to their scaling as

$$n = 1/s^D \quad (3.12)$$

Based upon this observation, we can define a so-called similarity dimension as [18]

$$D = \frac{\log n}{\log \frac{1}{s}} \quad (3.13)$$

where n is the number of self-similar parts, scaled by s .

With this in mind we can examine the Koch curve, formed from a straight line segment by repeatedly replacing each line with four new lines, each of $1/3$ the length. Figure 3.15 shows this process, and the resulting fractal structure. To

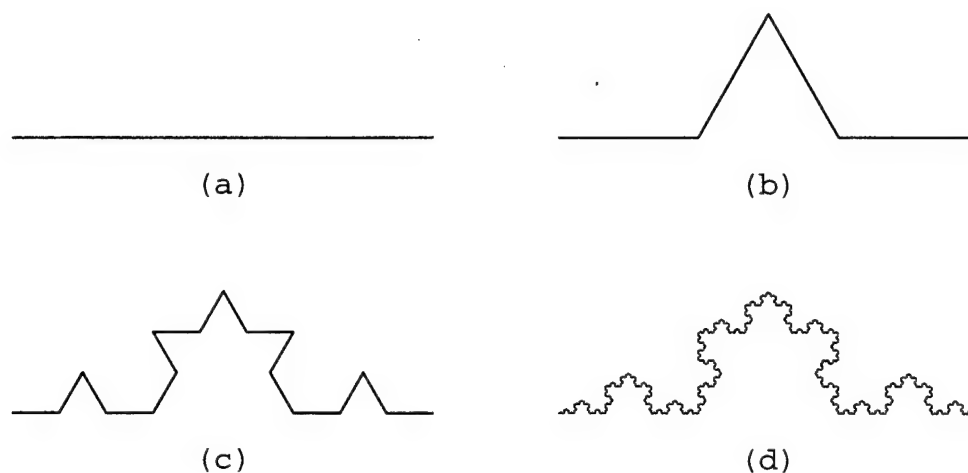


Figure 3.15: Constructing the Koch Curve: (a) shows the simple line segment “initiator” of the Koch curve, (b) shows the result of one iteration which replaces the original line with 4 new lines of $1/3$ the original length, (c) shows the second iteration, and (d) shows the more fractal-like Koch curve after only six iterations

calculate a similarity dimension, we use $n = 4$ parts with a scaling of $s = 1/3$, yielding

$$D = \frac{\log 4}{\log 3} = 1.26185 \dots \quad (3.14)$$

which is not integral in value. In fact, one of the identifying features of fractals is non-integer dimension. Comparing a one-dimensional line segment to the Koch curve, the Koch curve retains the properties of the line in terms of being divisible by a single break, yet the Koch curve requires more than one-dimension to contain its infinite structure. Hence, non-integer dimension aptly describes fractal objects.

Practically speaking, however, we cannot directly use (3.13) to calculate the dimension of more complicated structures such as the Lorenz attractor since local scaling cannot be precisely determined, but a more generalized box-counting ap-

proach can be employed. We can divide the phase space containing the attractor with a grid of side length l , then count how many boxes, N , of the grid actually contain some of the attractor. Since $N = 1/s^D$ and $s \propto l$ from the above discussions,

$$D \propto \frac{\log N}{\log \frac{1}{l}} \quad (3.15)$$

Thus, we can calculate N for several different grid sizes l , plot $\log N$ versus $\log l$, and estimate the fractal dimension from the linear slope.

We are concerned with the fractal dimension of attractors mainly because the calculation of the largest Lyapunov exponent relies on some knowledge of the attractor phase space, in order to correctly map the behavior of two neighboring trajectories. Given a simple time series, such as the output of the APM model developed in Chapter 2 however, we have no direct knowledge of the attractor or its phase space variables. Section 3.4.3 will discuss how to expand the concept of fractal dimension to a practical embedding dimension for the proper reconstruction of unknown chaotic attractors. For more information concerning fractals and fractal dimension, the interested reader can turn to several good publications [19, 20].

3.4.3 The Ikeda Map and Attractor Reconstruction

In order to properly calculate a largest Lyapunov exponent for an experimental system, we must have some knowledge of the system's phase-space portrait. For example, in performing even the simple exponent calculation for the Lorenz attractor in Section 3.3.3, we iterated two initial conditions in the full xyz phase space to determine their accumulated separation. The APM laser modeled in this thesis however, yields only a time series of the laser output. Based upon the complexity of the system, we have every reason to believe that the actual dynamics

occur in much more than one dimension. We are thus faced with the problem of “reconstructing” the phase portrait of the laser from only this time series.

Fortunately this problem has been addressed previously, as early as 1936, when H. Whitney discussed the mapping of manifolds [21]. Based upon his work, it can be shown that, given a single-variable time series, $x(t)$, one can construct an n -dimensional phase space from $x(t)$, $x(t - \tau_1)$, $x(t - \tau_2)$, ..., $x(t - \tau_n)$, for the proper choice of τ_k [22, 23, 24]. The idea behind this claim is that we simply need n *independent* system variables, not necessarily the true dynamical variables of the system, so that the reconstructed orbit will visit most of the system’s phase space, and thereby yield a complete phase portrait. Whitney’s contribution involved proving that the properties of the original attractor would be preserved if the phase-space embedding dimension, m (i.e., the Euclidean dimension within which we construct the attractor), were related to the true attractor dimension, D , by

$$m \geq 2D + 1 \quad (3.16)$$

More precisely, if this inequality holds, the mapping between the reconstructed and true attractor phase spaces will be one-to-one. If this is the case, we can use the reconstructed phase space to study the properties of the attractor, such as the fractal dimension or Lyapunov exponent spectrum.

The choice of the τ_k in the technique above was vaguely described as “proper.” More specifically, we need to choose the τ_k such that the delayed phase-space variables are roughly “independent” of each other. Several opinions have been voiced on the proper τ_k , and many originally believed that τ_k could be “almost arbitrary” [25, p. 295]. More recently, most researchers have agreed that the mutual information function of the time series should be used to determine for which delays will the variables be most uncorrelated [26]. The delay value for

the first minimum of this function is then used for τ . Setting all τ_k equal to this single value τ is also common, since the process of calculating several different delays is costly. Moreover, in the case of iterative mappings, the entire overhead of calculating the mutual information can be avoided because τ can be taken to be 1 iteration. One can choose $\tau = 1$ because each map iteration represents a long temporal evolution of the system (in the APM model, the pulses travel a complete round trip through the cavity), and thus successive iterations hold minimal mutual information.

To explore and verify the technique of attractor reconstruction, we can visit another iterative mapping, the Ikeda map [27, 28]. This map was first developed to express the transmitted light of a passive ring cavity containing a two-level absorber, and for this reason holds several similarities to the APM model of Chapter 2. More generally, it can be viewed as a mapping of the complex z plane to itself [26], and expressed as

$$z_{n+1} = p + Bz_n e^{\frac{i(\kappa+\alpha)}{1+|z_n|^2}} \quad (3.17)$$

For the parameter values of $p = 1.0$, $B = 0.9$, $\kappa = 0.4$, and $\alpha = 6.0$, the map exhibits chaotic behavior. Since the phase space is the complex plane, the attractor can be plotted in two dimensions, as shown in Figure 3.16. This swirling attractor has been shown to have fractal dimension $D \approx 1.8$ [29].

Even though (3.16) would require $2 \times 1.8 + 1 \rightarrow 5$ dimensions to properly embed the attractor, we can observe the results of using only two dimensions, since five would be difficult to visualize. We can reconstruct the attractor from $Re(z)$ in (3.17), by using $Re(z_n)$ and $Re(z_{n+1})$ ($\tau = 1$ from reasons discussed above for mappings). Figure 3.17 shows the reconstructed attractor which, although different from the original attractor, displays the same general properties with regards to

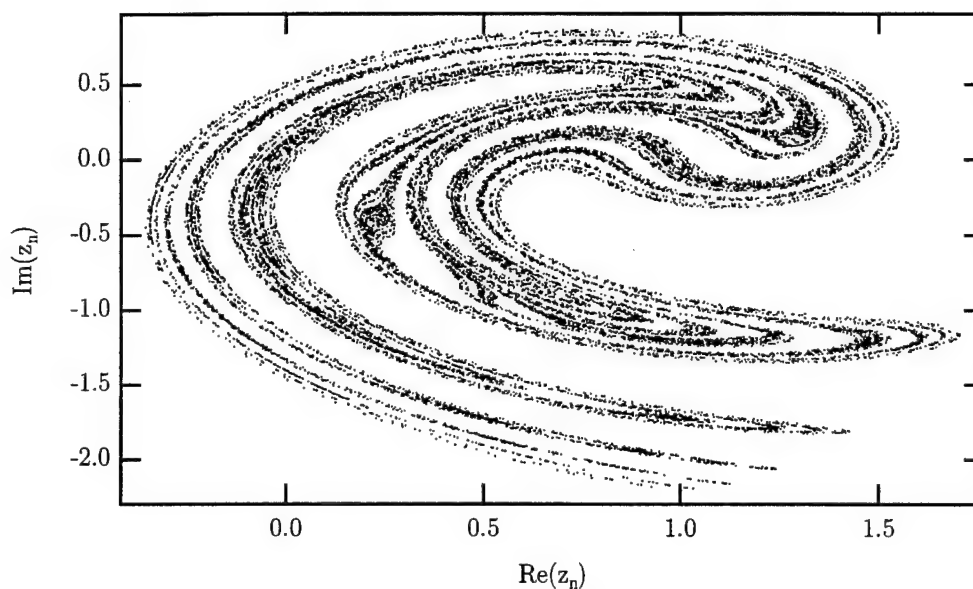


Figure 3.16: The Ikeda Attractor

the system dynamics.

Thus, to study the APM model, we can reconstruct the attractor in the appropriate dimensional phase space, simply with a time series of the output of the laser. Since we do not know the true dimension of the system beforehand however, we must use other techniques to estimate the proper embedding dimension. Abarbanel *et al.* have developed the so called method of false nearest neighbors for just the purpose of determining embedding dimension with data from a system with unknown phase space variables [29]. Nearest neighbors are simply points separated in phase space by a minimum distance. False nearest neighbors are neighbors which *appear* to be close to one another, as an artifact of projecting the attractor in an improper (too small) phase space. This can be visualized as follows: imagine projecting the Ikeda attractor of Figure 3.16 vertically onto a line. Every point from any given vertical slice of Figure 3.16 would then appear to be a nearest neighbor. Since a Lyapunov exponent calculation involves looking for nearest neighbors in

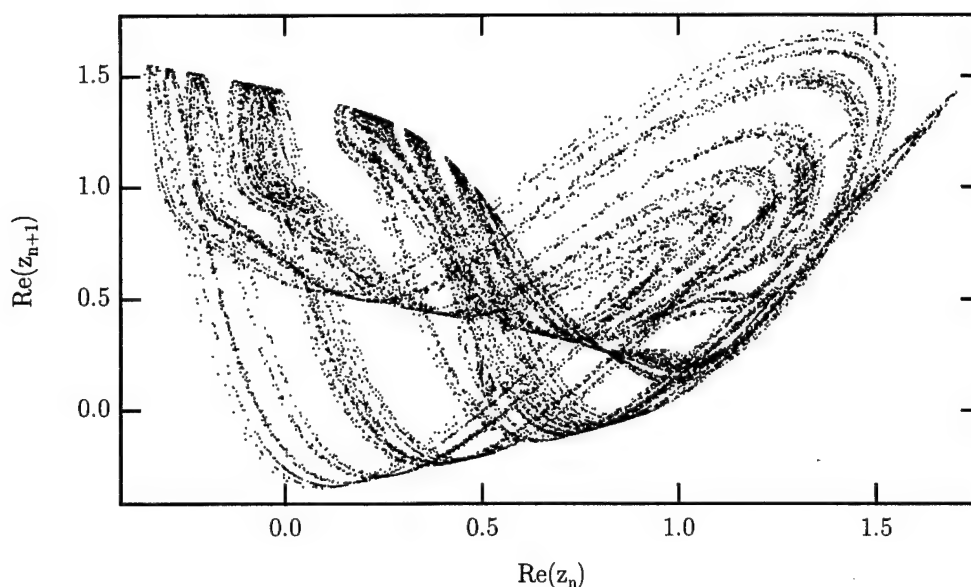


Figure 3.17: The Reconstructed Ikeda Attractor

phase space, so as to follow their divergence forward in time, the selection of false nearest neighbors can be catastrophic, because the two trajectories could actually have originated from opposite ends of the attractor. This would yield abnormally large Lyapunov exponents, since trajectories from opposite ends of the attractor are quite uncorrelated, and would likely diverge more rapidly than neighboring trajectories.

The method proposed by Abarbanel *et al.* tallies the total number of false nearest neighbors in phase space for a given dimension, d . By incrementally increasing the value of d , this number can be compared for larger and larger embedding dimensions, until the number of false neighbors decreases to zero. False neighbors are identified via two tests: given the distance between neighbors in dimension d , R_d , and $d + 1$, R_{d+1} , the neighbors are false if $R_{d+1} - R_d$ is large, or if R_{d+1} is comparable to the overall size of the attractor. The interested reader can consult the reference for the mathematical definitions of large and of the attractor size.

This reference also analyzes the method for several models and parameter ranges, concluding that the technique is quite robust.

We can see from Figure 3.17 that the two-dimensional Ikeda attractor reconstruction, although similar in dynamics to the original attractor, appears to suffer from exactly the false nearest neighbor epidemic discussed above. The once individual rings of the original attractor now cross in a complex pattern, which would surely confuse any attempt at a Lyapunov exponent calculation. The proper embedding dimension for the Ikeda attractor has in fact already been calculated by the method of false nearest neighbors discussed above [29], and been determined to be 4. With this information, we can now turn to a consideration of practical largest Lyapunov exponent calculation, and determine a largest exponent for the Ikeda map.

3.4.4 The Practical Lyapunov Exponent

A simplified calculation of the largest Lyapunov exponent for the Lorenz attractor was shown in Section 3.3.3. This technique, however, considered only one pair of neighboring trajectories, and therefore did not represent a global property of the attractor. Alan Wolf *et al.* have developed a more practical algorithm which essentially follows two trajectories completely around the attractor, so as to obtain a more global calculation [25].

The algorithm starts by selecting two nearest neighbor trajectories early in the time series. One is called the fiducial trajectory, and represents the particular trajectory which will be followed throughout the course of the algorithm. The problem with observing the long-range separation of the fiducial and its neighbor stems from local exponential divergence. The largest Lyapunov exponent characterizes

the small scale separation of trajectories with nearly identical initial conditions, and long evolution takes the trajectories to large separations (on the order of the attractor size), where the Lyapunov exponent no longer accurately models the separation. To prevent this, the Wolf algorithm monitors the separation of the fiducial trajectory and its neighbor only for a short amount of time (number of iterations in the case of a map). The algorithm then replaces the fiducial's neighbor with a different, closer neighbor. The new neighbor is selected based upon both its proximity to the fiducial, and the smallness of the angle it makes with the fiducial and the old neighbor. In this manner, the relationship between the fiducial and the old neighbor trajectories is retained to the highest accuracy. After such a replacement, the evolution of the fiducial and its new close neighbor are monitored for a fixed amount of time, at which point the process repeats.

Before each replacement, the initial and final separation between the fiducial and its neighbor trajectory are used to calculate the k^{th} local exponent through the relation

$$\lambda_k = \frac{1}{T} \log_2 \frac{\delta_{i,k}}{\delta_{f,k}} \quad (3.18)$$

where T is the total time (or number of iterations) since the last replacement. This is simply the same estimation of local slope as performed in Section 3.3.3. When the entire time series of data has been processed, all of the local exponents are averaged to find the global exponent. Since the initial trajectory has been monitored throughout the entire time series, this average will converge to the actual largest Lyapunov exponent as the time series length $\rightarrow \infty$.

The Wolf code takes several parameters to tailor the calculation to a specific data set. First is the minimum initial displacement between neighbors, used to prevent selection of neighbors closer than the noise level of the data. Next is the

maximum initial displacement between neighbors, to guarantee the selection of close neighbors (where “close” is attractor dependent). The evolution time, or fixed number of iterations between replacements is also required, and finally, the maximum allowable angle between replacements. Wolf *et al.* have investigated how each of these parameters affects the calculation, and found acceptable results for large parameter ranges. Generally, results are better with a smaller minimum replacement parameter (noise allowing), with a maximum on the order of less than 5% of the attractor extent, with an angle under 10° , and an evolution time on the order of the time it takes for a trajectory to orbit the attractor once.

Using a version of this Wolf algorithm, I calculated a largest Lyapunov exponent for the Ikeda map, using the method of delays described above to reconstruct the attractor in four dimensions from $Re(z)$. I specified the minimum and maximum initial displacements as 10^{-5} and 0.20 respectively, or about 0.00025% and 5% of the overall Ikeda attractor size (see Figure 3.16). Additionally, I specified the maximum angle as 5° , and the evolution time of 12 iterations, since it takes about 12 iterations to circle the attractor in Figure 3.16. Operating on a time series of 20,000 points from (3.17), I arrived at the averaged result $\lambda = 0.501$ bits/iteration, which is easily within 5% of published analytical results [26].

The calculation of a largest Lyapunov exponent made possible by attractor reconstruction, combined with the graphical analysis of bifurcation diagrams, especially as applied to the logistic and Ikeda maps in this section, will directly translate to the model of the additive-pulse modelocked laser. Chapter 4 will first discuss the APM model as a map, then apply the nonlinear dynamics concepts of this chapter to analyze the dynamical behavior of the laser under certain parameter variations.

Chapter 4

Simulated Additive-pulse Modelocked Laser Dynamics

4.1 Typical Operation

4.1.1 The Additive-pulse Modelocked Laser Model as a Map

The additive-pulse modelocked (APM) laser contains gain, a tuning element, and nonlinearity among other things, and is capable of several different, complex types of operation. Chapter 2 considered in detail the factors determining the operation of this laser, forming a set of equations (2.51) to describe the evolution of a femtosecond light pulse during one round-trip through the laser. In addition, based upon experimental examples of the laser, Chapter 2 calculated the laser parameters necessary to achieve the reported stable behavior.

Like the logistic map of Chapter 3, the APM model (2.51) takes the current state of the laser system to the next state. The state of the laser is recorded

as the two counter-propagating pulses a_1^n and a_2^n , and the output of the system is described by the output pulse energy. The first system state is given by the simulation seed pulse developed in Section 2.5.2 for a_1 , and $a_2 = 0$. In order to implement the model on a computer, the system state can be digitized, and each of a_1 and a_2 stored in 1024-point vectors. The model was coded in both MATLAB and the C programming language, which produced identical results.

The simulation produced a stable output train of 106 fs pulses, with an output power of 104 mW as calculated from the pulse amplitude and the relationships of Section 2.5.2. Figure 4.1 shows a typical pulse and its spectrum, with the measured pulse duration and bandwidth. The output energy of each pulse is calculated to be 6.91 nJ/cm², which corresponds to 104 mW, given the pulse width and output beam radius of 0.245 cm from Figure 2.2. With a time bandwidth product of 0.440, the laser produces transform-limited Gaussian pulses [11, p. 334]. These results are quite consistent with the design of Chapter 2.

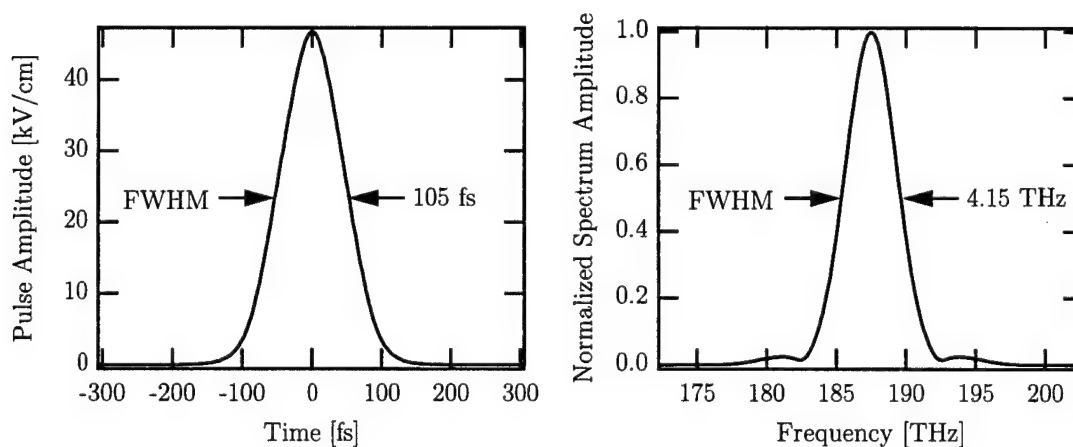


Figure 4.1: The Steady-state Output of the Simulated APM Laser

Although the APM simulations have produced meaningful output, the real value of the model lies in its ability to simulate the laser's behavior when design

parameters change. This thesis is primarily concerned with nonlinear dynamics, and the remainder of this chapter will explore nonlinear issues as the laser parameters change from the designed, stable APM operation.

4.1.2 Other Steady-state Experimental Observations

Although the APM laser has been experimentally perfected for many years to improve stability, it is inherently susceptible to complex and unstable operation due to its large nonlinearity. Other authors have already reported observations of period-doubling, quasiperiodicity, and even chaos in actively stabilized APM lasers [2, 3]. The femtosecond NaCl laser at Cornell University has verified these findings, as shown in Figure 4.2. The period-two behavior is quite pronounced, while the irregular behavior in (b) could be either quasiperiodicity or chaos, which can only be determined by a difficult analysis of the experimental data.

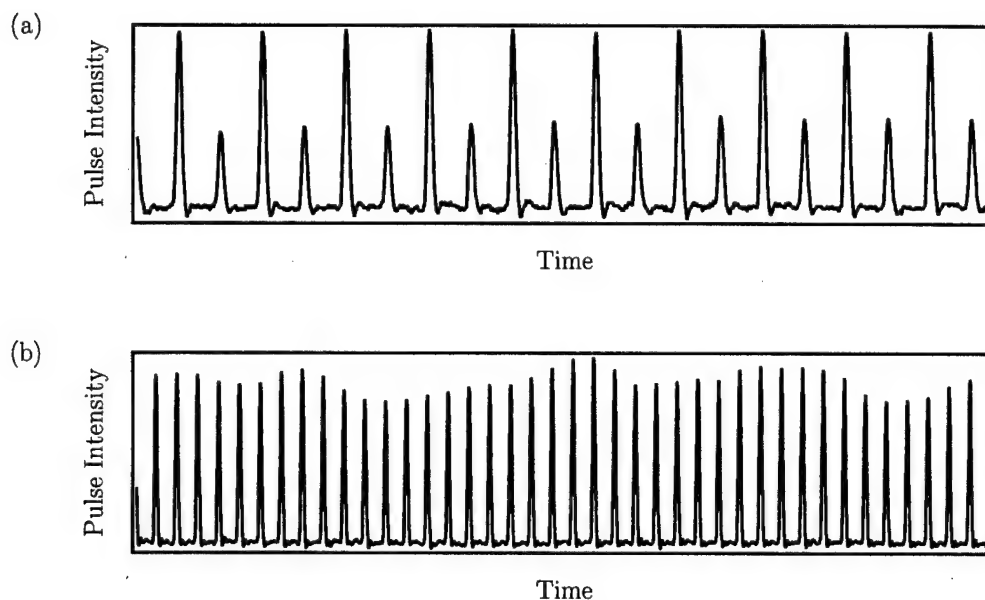


Figure 4.2: Experimental Instabilities in the APM Laser. (a) shows strong period-two behavior and (b) shows an even more complex yet deterministic output

While current publications discuss various instabilities in the APM laser, the effect of different laser designs has yet to be considered. Specifically, how do parameters such as the forward and backward fiber coupling coefficients, fiber length, and gain affect the laser dynamics? The APM laser is known to operate stably over a large range of parameters, and for this reason has been successfully used as a research tool. For example, Figure 4.3 shows the laser output energy versus fiber length, for a large range of lengths. Each separate length on the graph

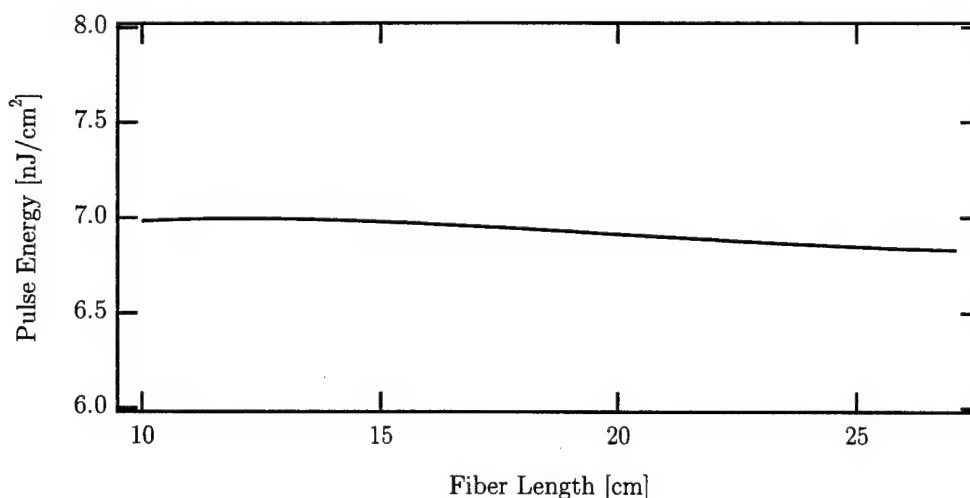


Figure 4.3: APM Output Energy vs. Fiber Length for the Design of Chapter 2

represents a unique simulation, showing 30 successive output pulse energies. Since the graph traces a line, each length considered exhibits stable operation (a constant pulse output energy). Despite this stable APM operation however, we will find in the remainder of this chapter that, for large regions of parameter space, the laser can be quite unstable.

4.2 Nonlinear Laser Dynamics

4.2.1 Quasiperiodicity in the Simulated Laser

To begin a more involved exploration of parameter space, we can lengthen the fiber beyond the study in Figure 4.3. The operation of the APM laser for lengths of 20–55 cm is shown in a bifurcation diagram, Figure 4.4. Beyond $l \sim 27$ cm, the output pulse energies begin to exhibit a large spread of values. To determine the nature of these variations, we can examine the evolution of the laser output pulse energies, shown in Figure 4.5. The output energies follow a sinusoidal path, with a period of about 20.5 iterations.

By creating a two-dimensional delayed-coordinate system as described in Chapter 3, we can observe the phase portrait of the output. Figure 4.6 shows the resulting closed loop, which indicates periodicity in addition to the fundamental (period-one) oscillations. The loop is continuous because the secondary oscillation frequency is not a multiple of the fundamental frequency. In other words, the two frequencies are incommensurate, and the laser is thus exhibiting quasiperiodicity. This type of plot, because it shows the n^{th} versus the $n + 1^{\text{th}}$ iteration, is often called a *first return map*, or a *Lorenz section*. A first return map, depending upon its complexity, can give information about the output dynamics, especially relating to prediction of future states. Figure 4.6 shows that the laser output is confined to a single loop in phase space for all time. The topologically linear orbit indicates a lack of fractal dimension, or equivalently, a lack of chaotic oscillations in the laser output.

If we examine sections of the APM output for the even longer fiber lengths displayed in Figure 4.4, we find that the output remains quasiperiodic, but the

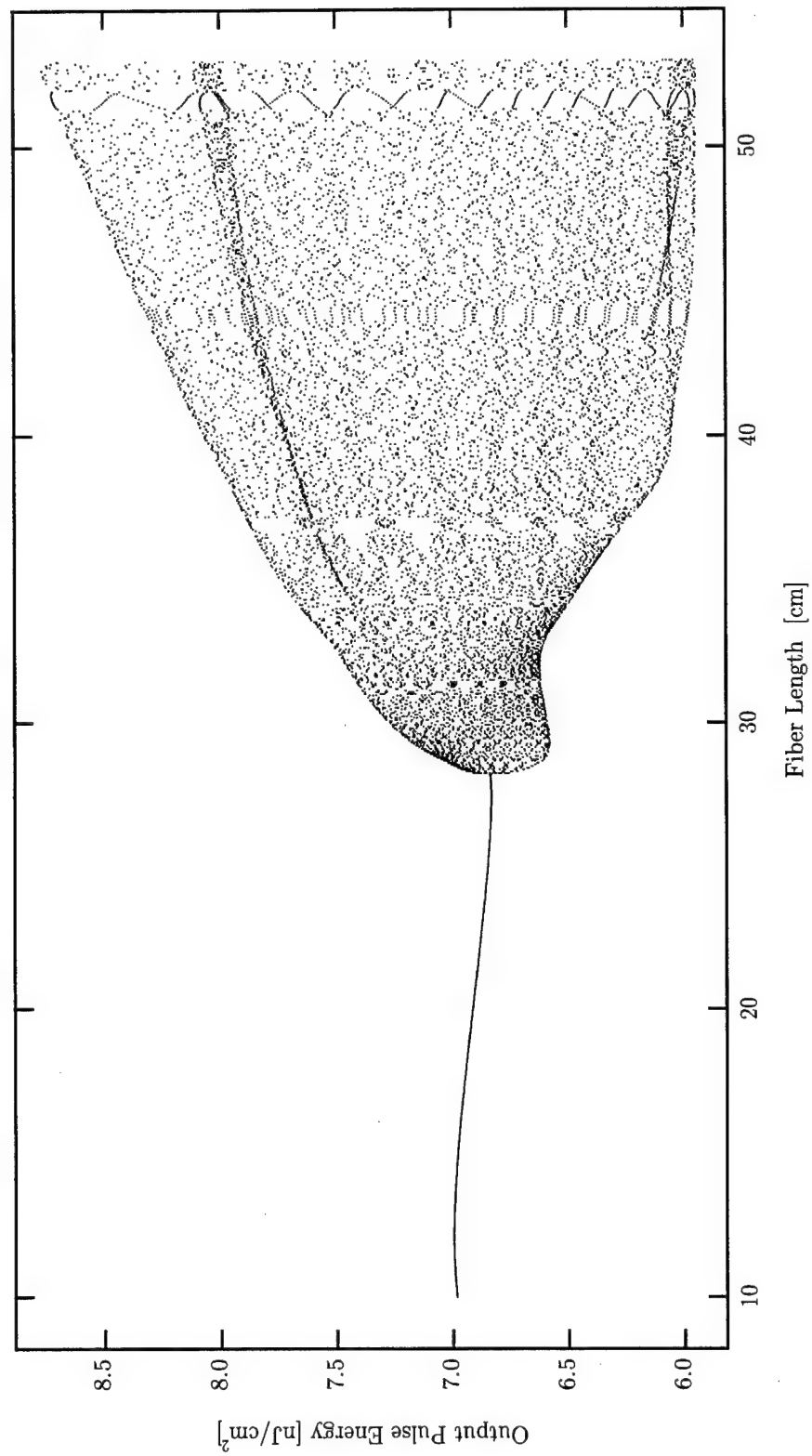


Figure 4.4: An APM Laser Bifurcation Diagram for Increased Fiber Length

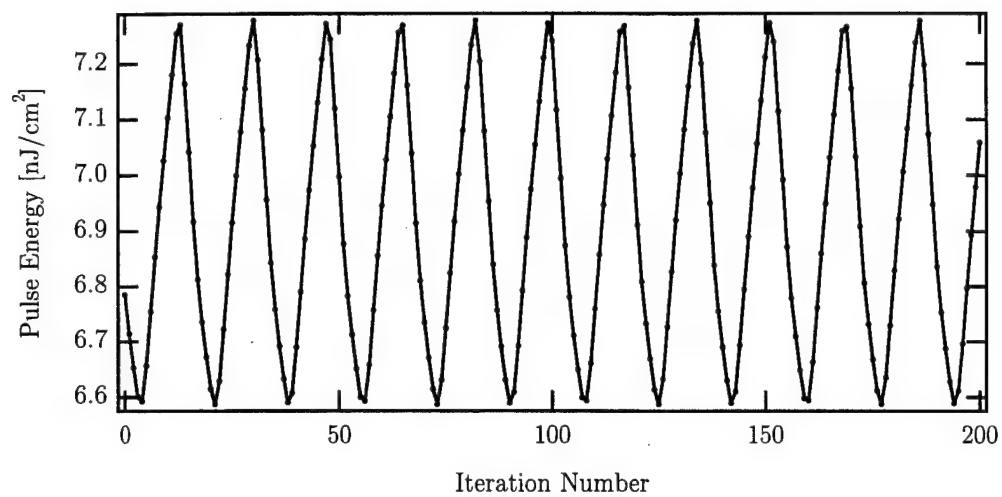


Figure 4.5: Quasiperiodicity in the APM Laser Output

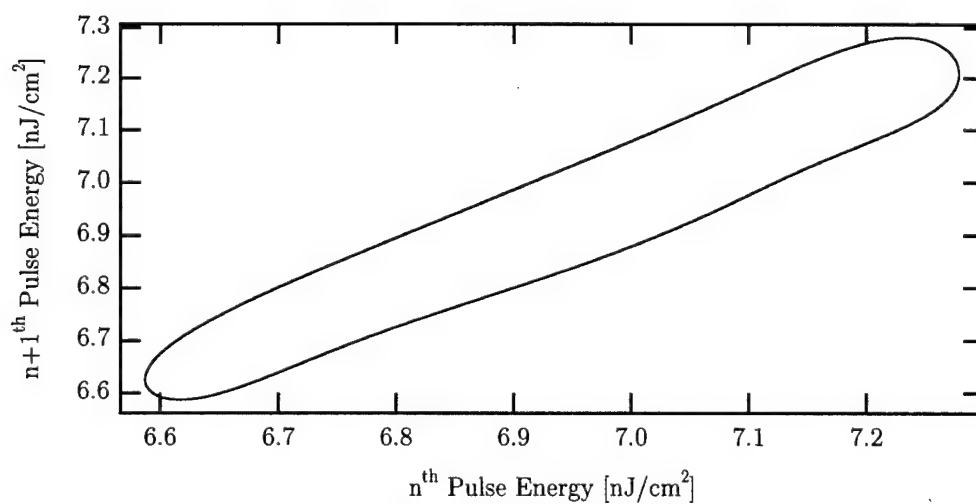


Figure 4.6: A Phase Portrait of the Quasiperiodic APM Output

phase-space orbit gradually deforms into more complex shapes. Figure 4.7 shows this trend, for lengths of 30, 40 and 50 cm.

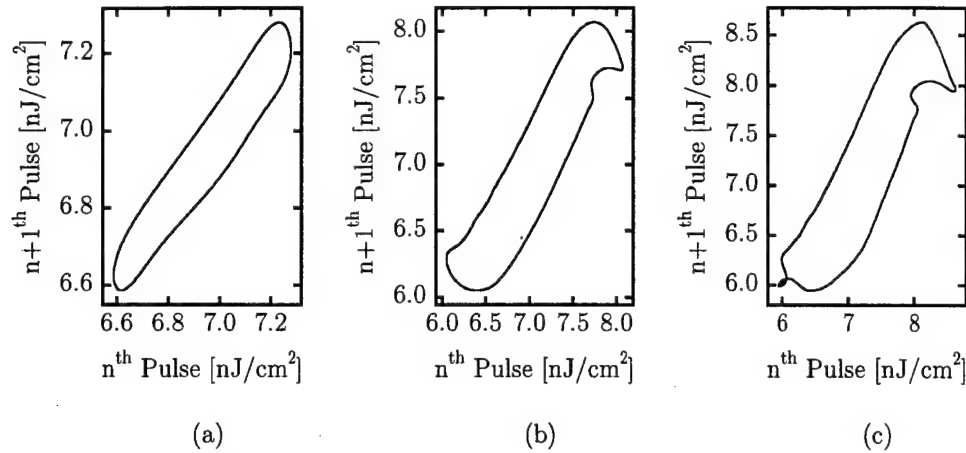


Figure 4.7: Quasiperiodicity in the APM Output for 3 Different Fiber Lengths: (a) $l = 30$ cm (b) $l = 40$ cm and (c) $l = 50$ cm

4.2.2 Period-doubling and Chaos in the Simulated Laser

With a large amount of experimental effort devoted to studying the additive-pulse modelocked (APM) laser, several improvements have been made, especially relating to fiber coupling. In particular, Yakymyshyn *et al.* reported that the main-to-external round-trip cavity coupling coefficient (i.e., the beamsplitter and fiber couplings, each taken twice) was typically ~ 0.2 . Currently, however, forward fiber couplings have been increased to $\sim 80\%$ with ball lenses and telescope configurations. Together with a beamsplitter reflectivity of 70–90% and fiber back-coupling of 90%, the total coupling coefficient can be as great as 0.68. Even modest increases in the coupling can have dramatic effects in the laser dynamics, since the coupling directly affects the amount of nonlinearity in the APM system.

With this in mind, we can again use the simulation developed in Chapter 2, but

with the fiber couplings increased: $\gamma = 0.8$, and $\gamma_2 = 0.9$. Increasing the coupling will affect overall laser performance, primarily by reducing the saturated gain, since more power will be coupled back from the external cavity into the main. Figure 4.8 shows the resulting bifurcation diagram for the laser with larger coupling, which is just a plot of output pulse energy versus fiber length, as in Figure 4.3. With these new couplings we see a bifurcation to period-two behavior at a fiber length of ~ 9 cm. Beyond this, each branch further period-doubles into a chaotic regime, to be verified in Section 4.2.3 by a Lyapunov exponent calculation, as performed for the Lorenz system and the logistic map in Chapter 3.

Before such a calculation, it is informative to examine the exact nature of the period-two pulse solutions. The bifurcation diagram shows both low and high-energy pulses at the output. Iterating the model at a period-two fiber length, say 10 cm, we can examine successive pulses in the main and external cavities (the output is just the external cavity pulse b_2 , scaled by the beamsplitter: see Figure 2.6). Figure 4.9 shows that the pulses in the main cavity alternate between high and low energies, in perfect antiphase with those of the external cavity. The two cavities in fact exchange some set amount of energy each round-trip. One may also note that the external cavity pulses contain much structure, quite unlike the picture presented by Figure 4.2. This is caused by nonlinear phase chirp and interferometric recombination of pulses, as opposed to a mere amplification process. The experimental data from Figure 4.2 is collected by a laboratory detector, which cannot possibly resolve a 100 fs pulse, but rather integrates the pulse intensity and provides output proportional to the pulse energy. As a result, laboratory time series data can yield only a single number to characterize each pulse, while the simulation in this thesis gives more evidence to the underlying dynamics.

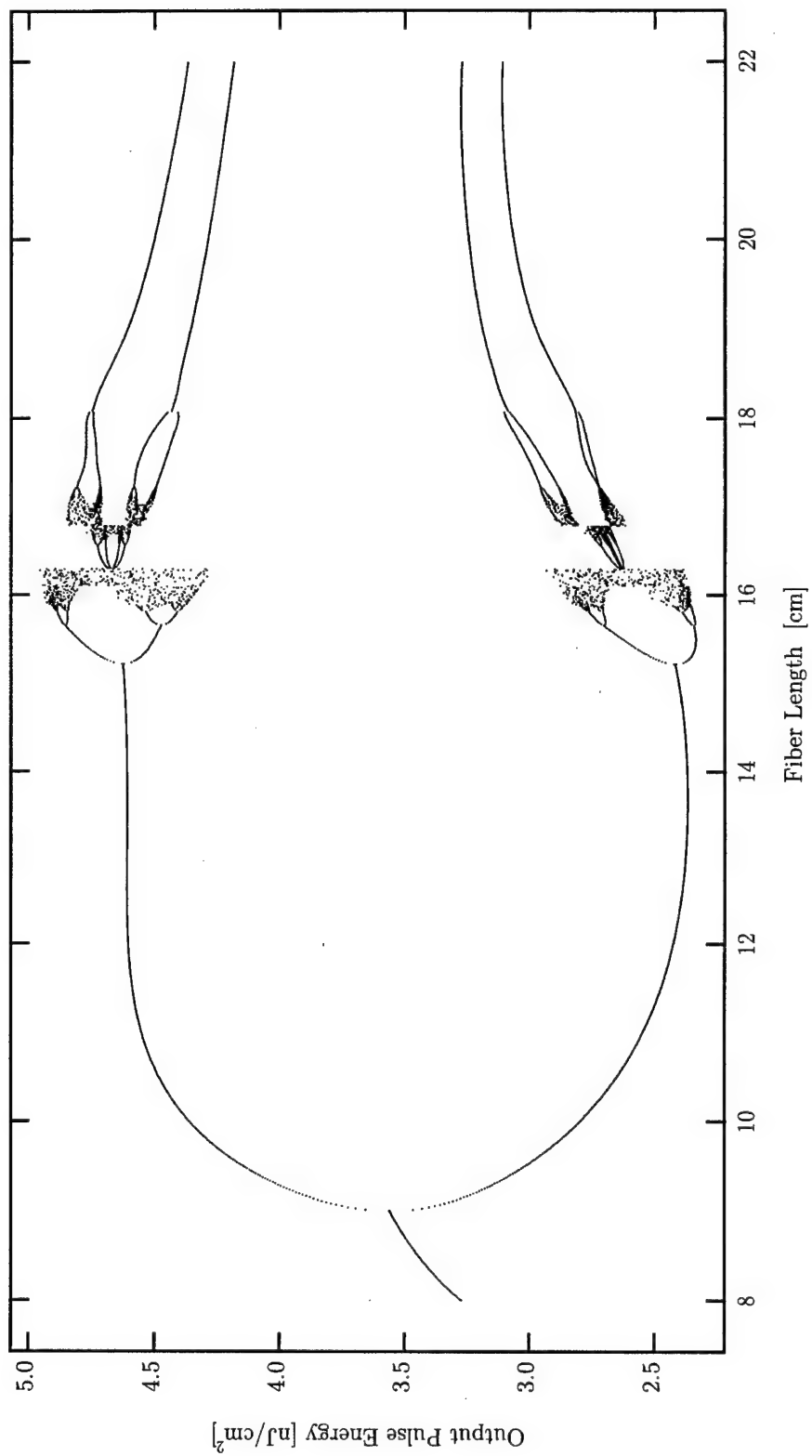


Figure 4.8: A Period-Doubling APM Laser Bifurcation Diagram: a plot of output pulse energy versus fiber length, for $\gamma = 0.8$ and $\gamma_2 = 0.9$

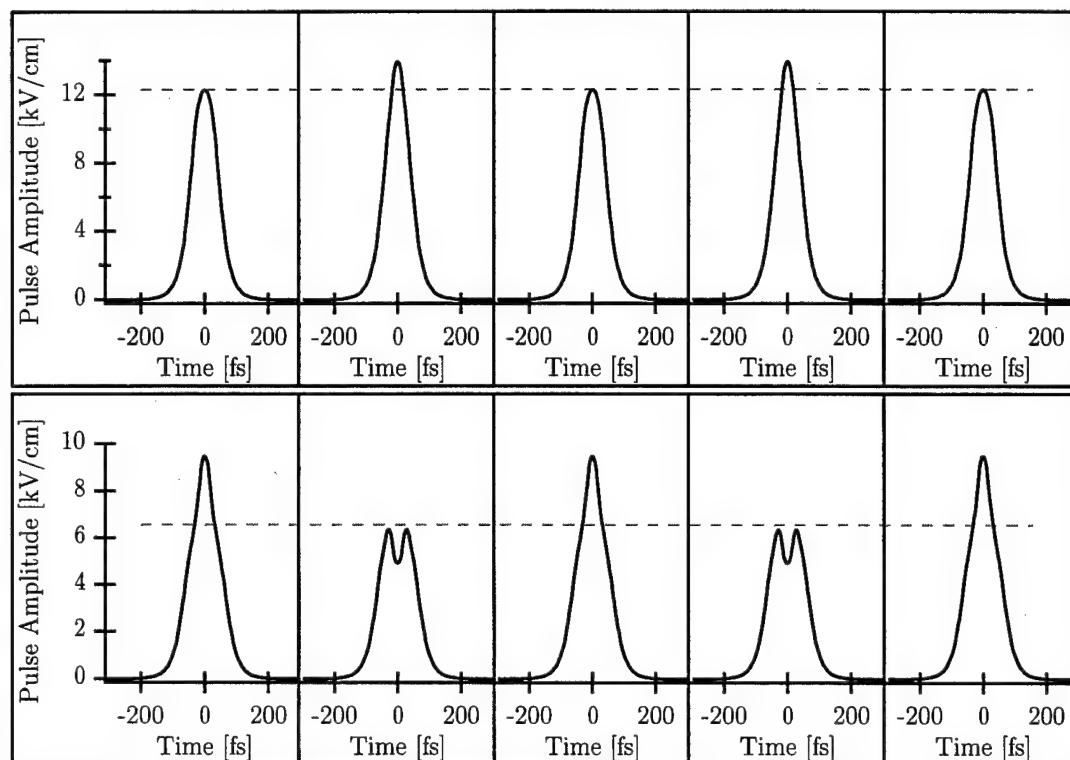


Figure 4.9: Period-two Pulses in the main (upper row) and external (lower row) APM cavities, for 5 successive iterations with a fiber length of 10 cm

Figure 4.10 shows a magnified view of the complicated APM bifurcations above $l \sim 15.85$ cm. Beyond the initial period-doubling and chaos, the magnified diagram shows that the output suddenly displays period-2 output again, at a length of ~ 16.3 cm, which then immediately bifurcates to period-8. The laser proceeds to period-double into another chaotic regime, around $l \sim 16.7$ cm. Beyond this, the chaotic regime abruptly changes size, and then *reverse bifurcates* back down to period 4. The abrupt changes in the bifurcation diagram are in fact *crises*, and will be explained and explored in more detail in Section 4.2.4. Additionally, the chaotic regions of Figure 4.8 will all be studied and verified by Lyapunov exponent calculations in Section 4.2.3.

4.2.3 Chaotic APM Behavior

Above a fiber length of about 15.85 cm, the laser exhibits very unstable behavior, which, from Figure 4.8 cannot be distinguished as either quasiperiodicity or chaos. There are in fact three separate regions on the bifurcation diagram which appear to exhibit large instabilities: $l \approx 15.9\text{--}16.3$ cm, $l \approx 16.67\text{--}16.76$ cm, and $l \approx 16.83\text{--}17.12$ cm. To verify the existence of chaos, we can perform a largest Lyapunov exponent calculation in each region, as done for the logistic map in Section 3.4.4. If the largest Lyapunov exponent is > 0 , we can conclude that these regions indeed exhibit a sensitive dependence on initial conditions, and are therefore chaotic.

Since the Wolf algorithm described in Section 3.4.4 requires a reconstructed attractor to calculate an exponent, we first calculated the proper embedding dimension for the APM attractor in each of the three regions, using the false-nearest neighbor technique described in Section 3.4.3. The Abarbanel code showed that the proper embedding dimension is 3 in each case, as seen in Figure 4.11, since the

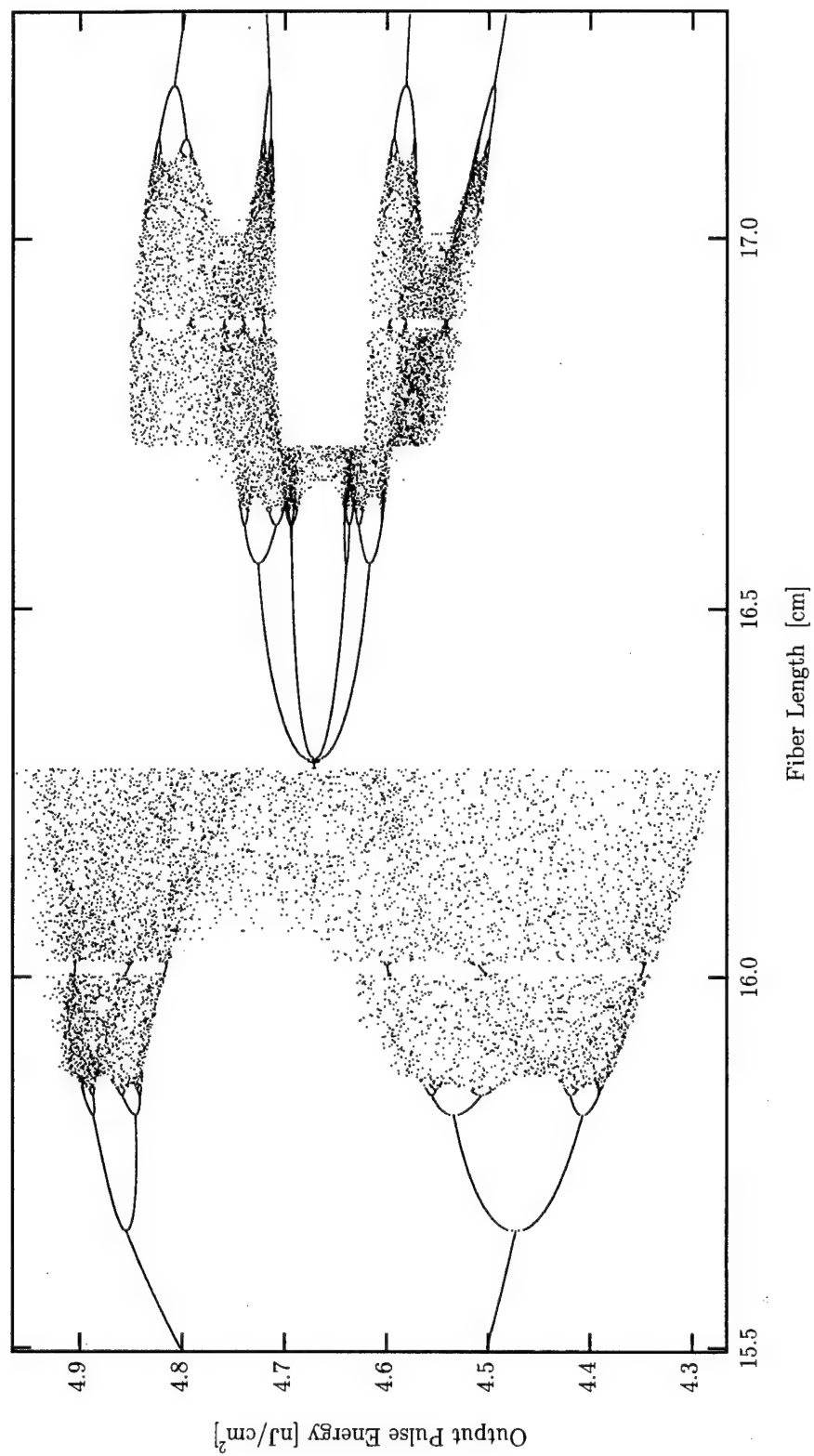


Figure 4.10: The APM Laser Bifurcation Diagram Magnified: output pulse energy versus fiber length

number of false-nearest neighbors drops to zero for 3 dimensions.

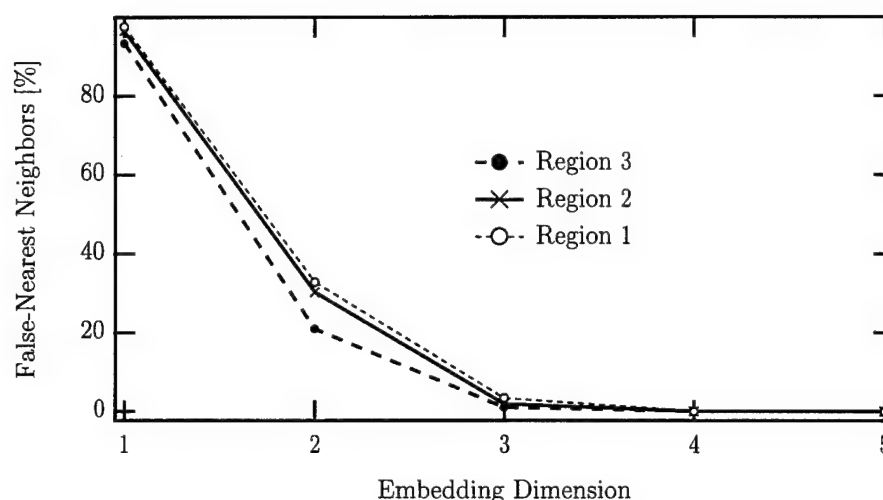


Figure 4.11: Embedding Dimension Calculation for Chaos in Figure 4.8

Knowing the proper embedding dimension, we reconstructed each region's attractor in three dimensions, using the delayed coordinate technique of Section 3.4.3. We first set the fiber length in the unstable region, then preiterated the APM model several thousand times to let any initial transients die out. Next, we iterated the APM simulator 32,000 times and recorded the output energies, generating a long output time series. Plots were then constructed by creating the delayed coordinates from the output time series: the n^{th} iterate, versus the $n+1^{\text{th}}$ iterate, versus the $n+2^{\text{th}}$ iterate. The results are shown in Figures 4.12–4.19, for each of the three chaotic regions shown in Figure 4.10. The first two chaotic regions, at $l \sim 16.2$ cm and $l \sim 16.7$ cm, each have two branches, due to the underlying period-two behavior (see the larger view in Figure 4.8). For this reason, there are two distinct attractors for each of these regions, shown in Figures 4.12–4.15. The third chaotic region, at $l \sim 16.8$ cm, likewise has four branches and therefore four distinct attractors, shown in Figures 4.16–4.19. Each attractor is easily visualized in three dimensions, which verifies the previous embedding dimension calculations.

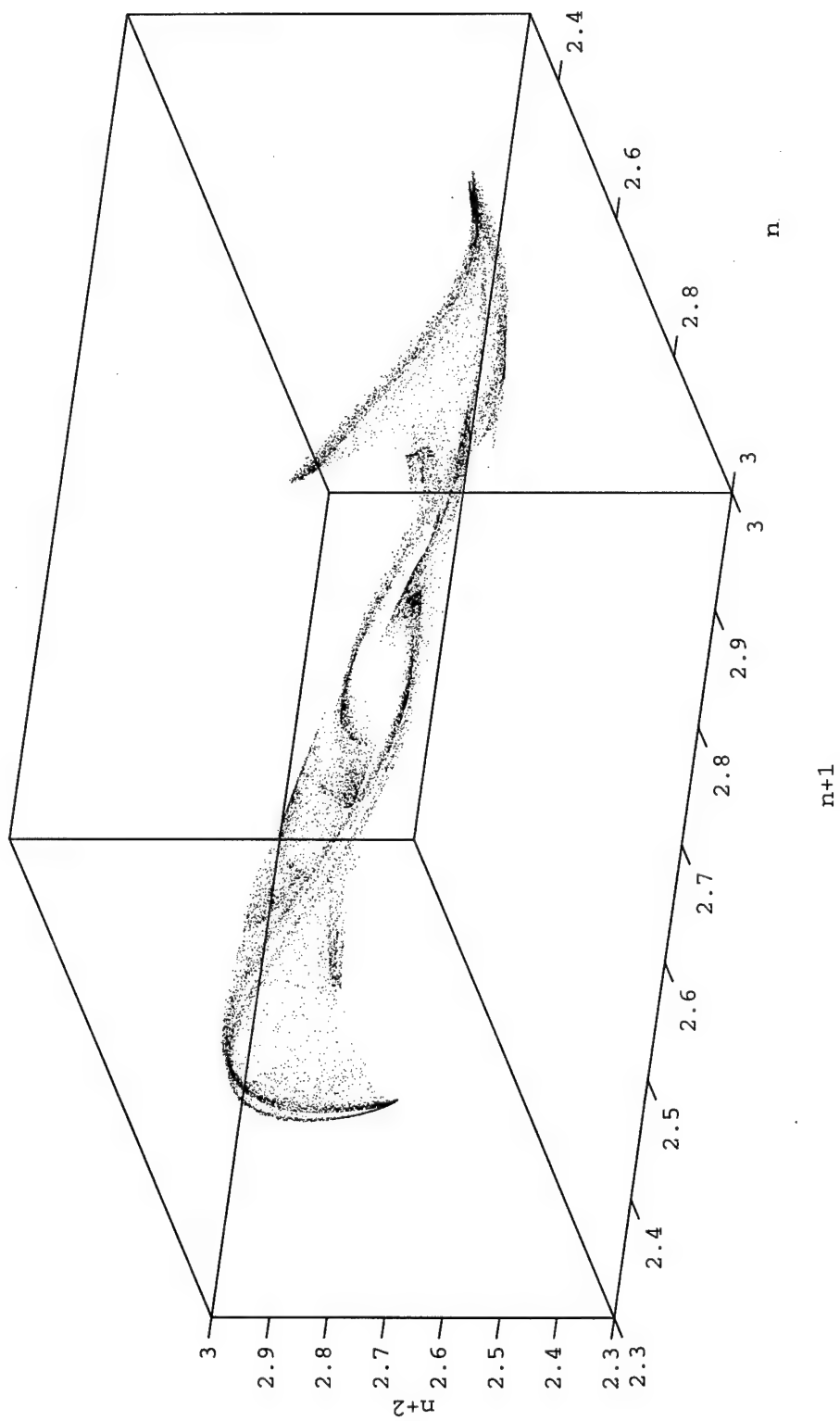


Figure 4.12: An APM Chaotic Attractor: one of two at $l = 16.258$ cm

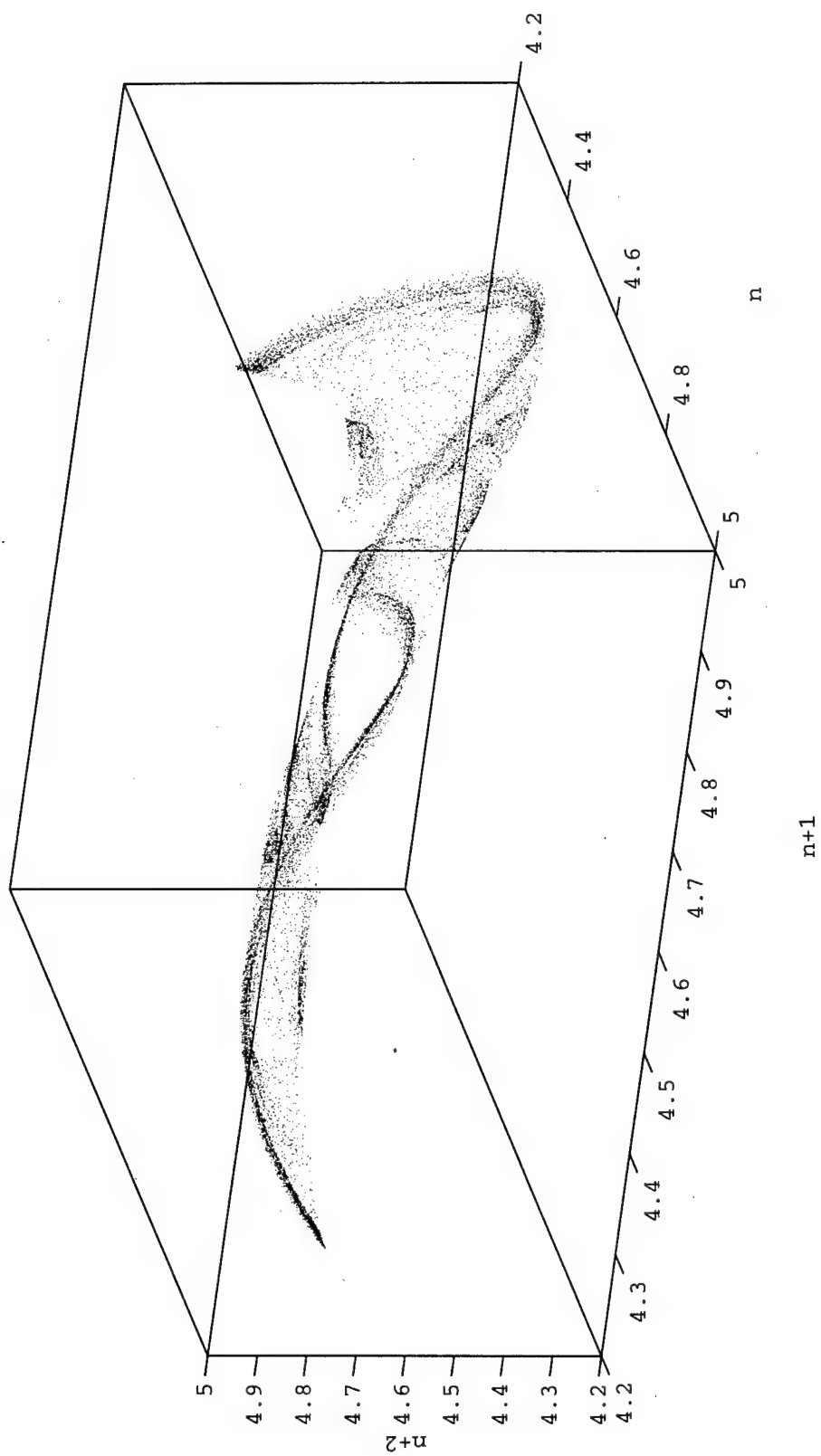


Figure 4.13: An APM Chaotic Attractor: two of two at $l = 16.258$ cm

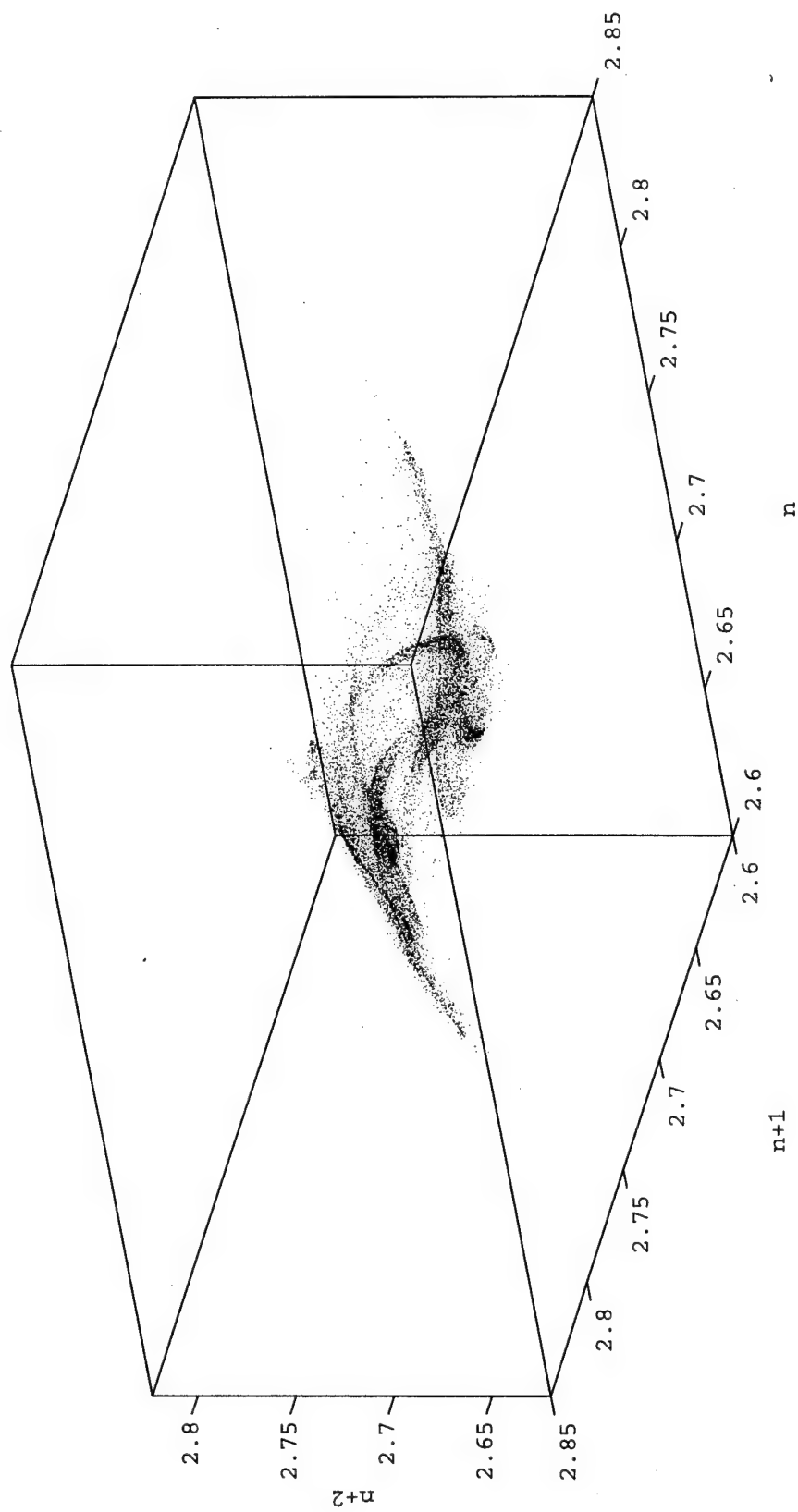


Figure 4.14: An APM Chaotic Attractor: one of two at $l = 16.71$ cm

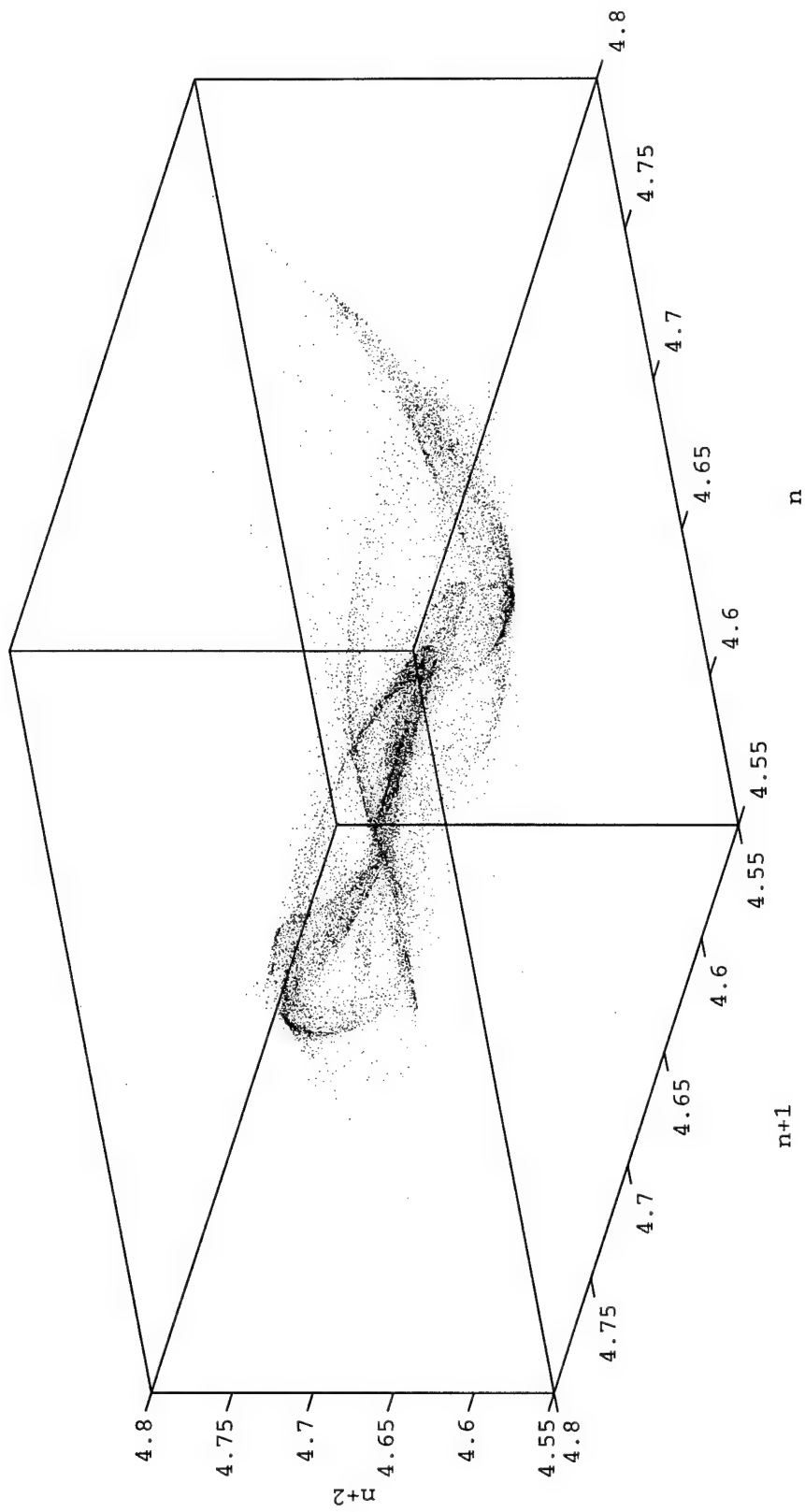


Figure 4.15: An APM Chaotic Attractor: two of two at $l = 16.71$ cm

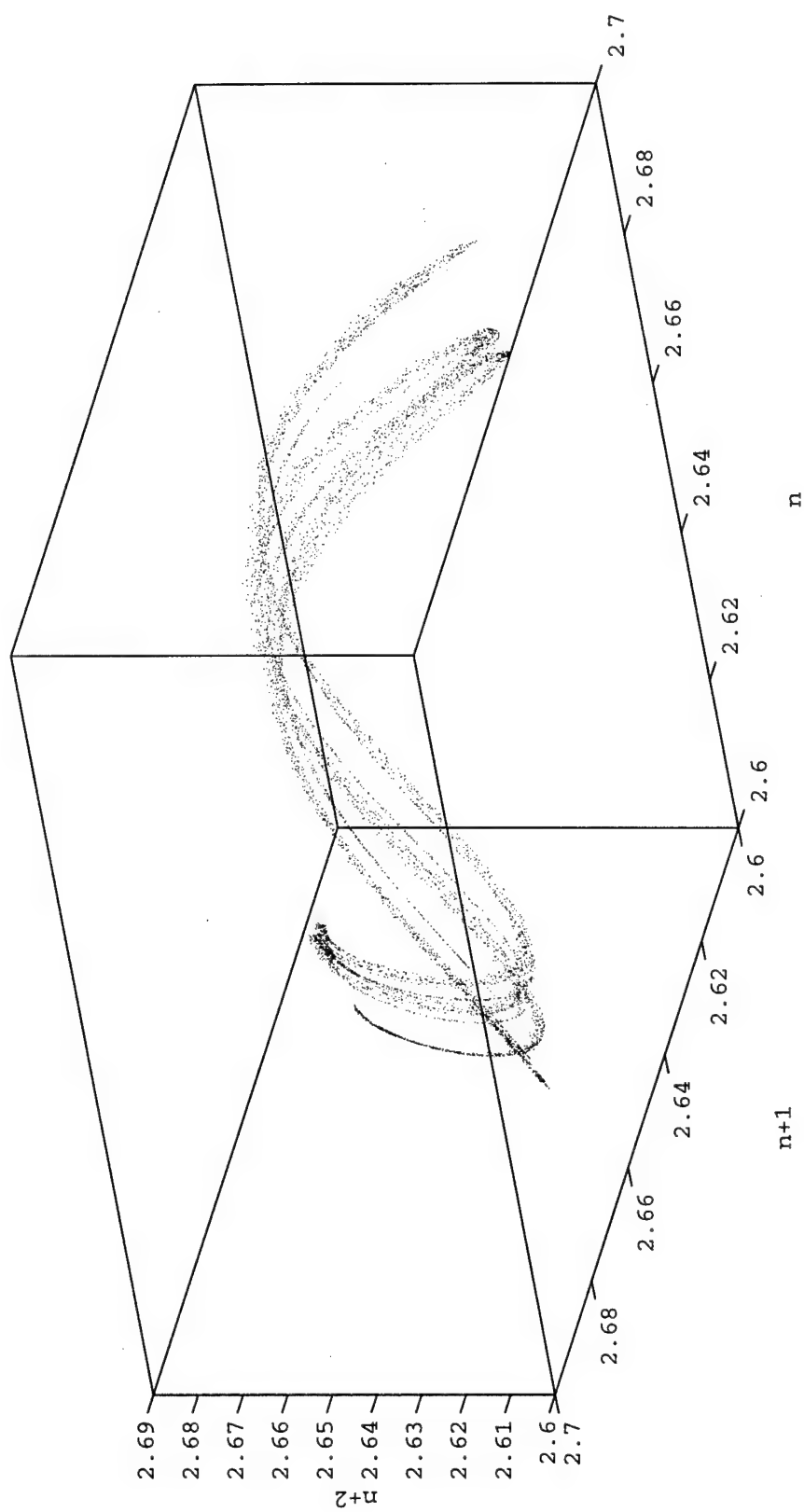


Figure 4.16: An APM Chaotic Attractor: one of four at $l = 16.722$ cm

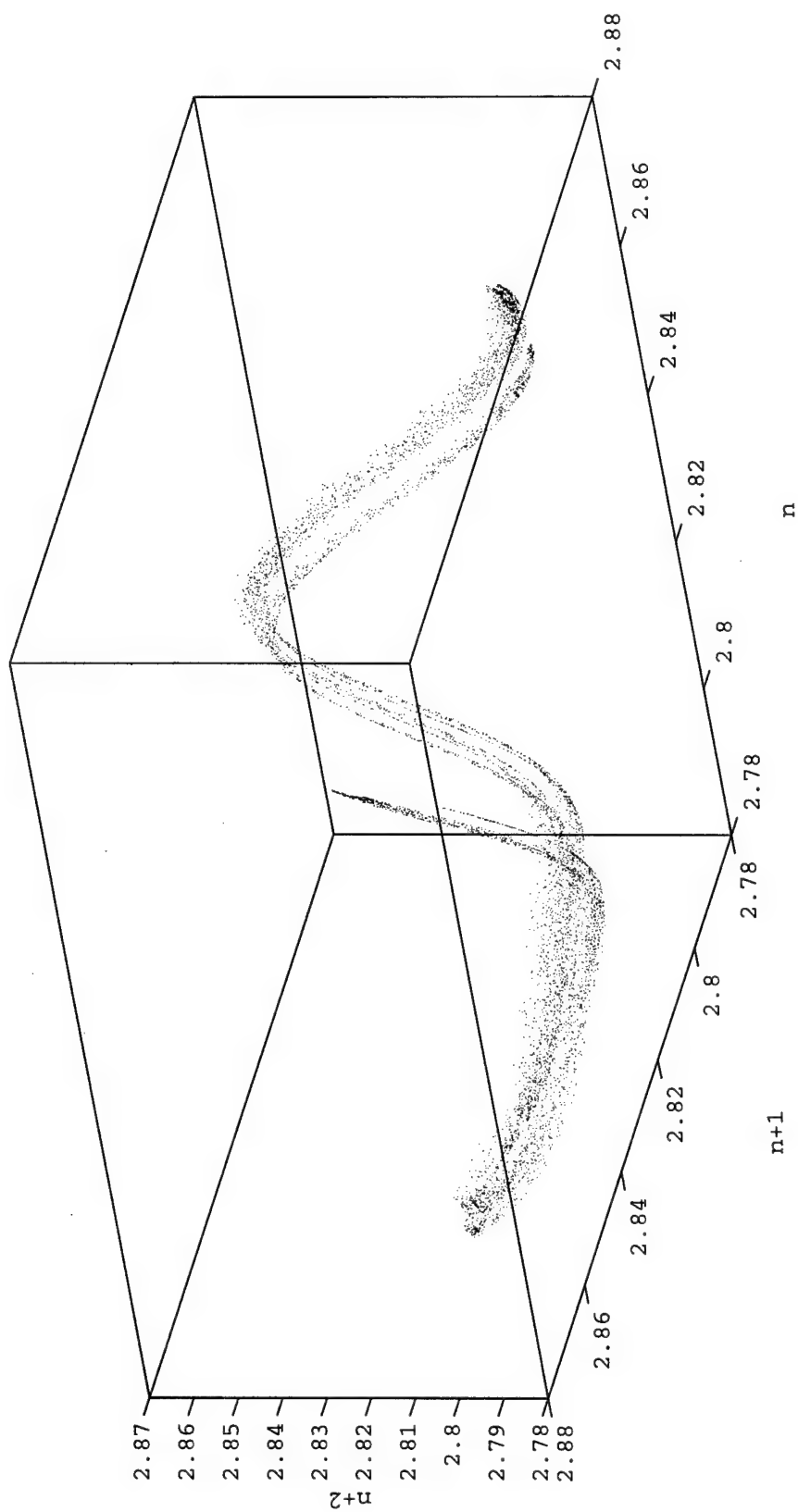


Figure 4.17: An APM Chaotic Attractor: two of four at $l = 16.722$ cm

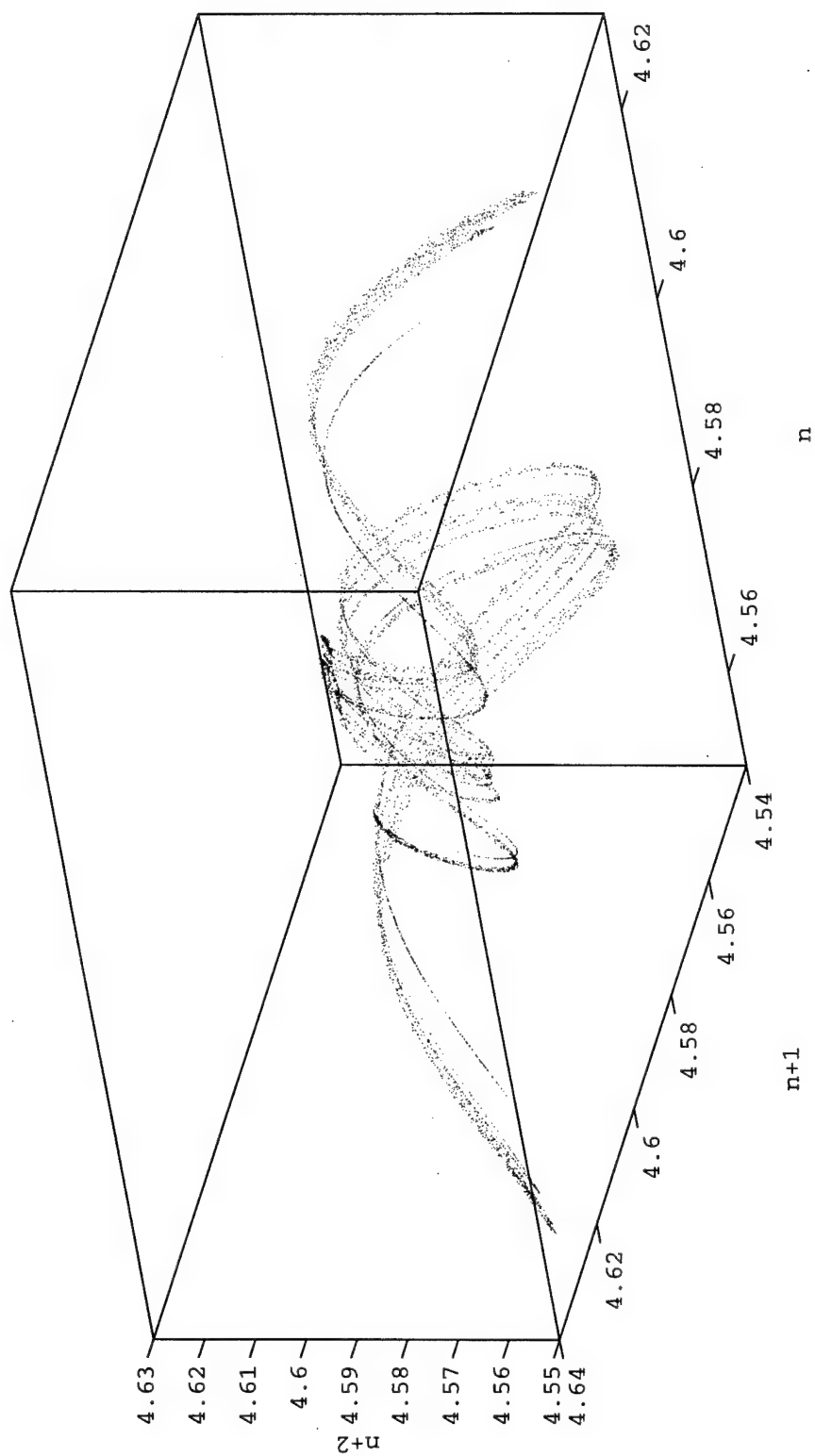


Figure 4.18: An APM Chaotic Attractor: three of four at $l = 16.722$ cm

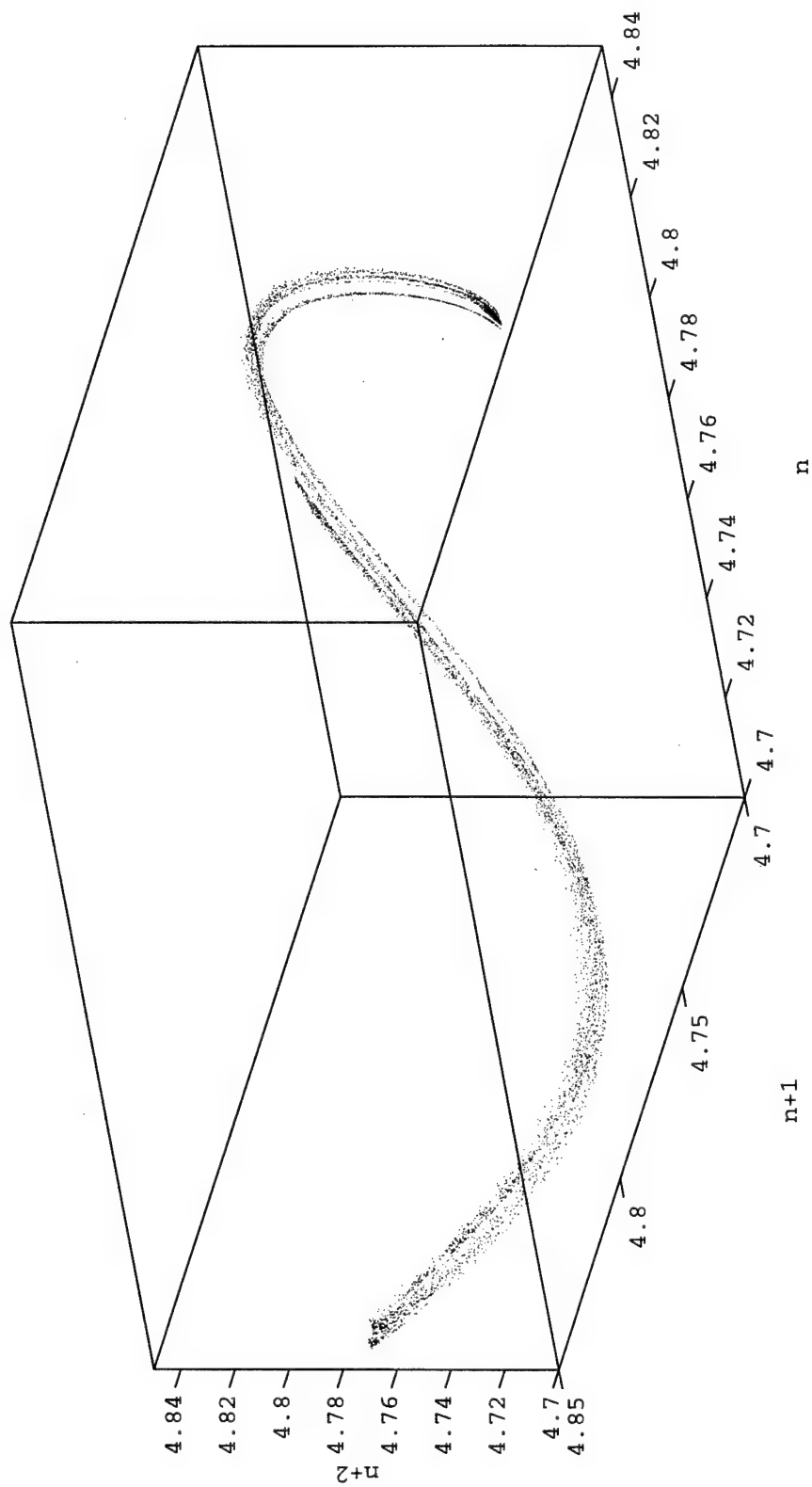


Figure 4.19: An APM Chaotic Attractor: four of four at $l = 16.722$ cm

Having reconstructed these attractors, we performed a largest Lyapunov calculation for each region. The Wolf code processed the each reconstructed attractor with a minimum initial displacement of $\sim 10^{-5}$ and a “largeness” condition on the final displacement of $\sim 10^{-2}$, thus allowing initial trajectories to diverge by three orders of magnitude before calculating local exponents. The computed average largest Lyapunov exponents were all positive, indicating that each region indeed exhibits chaos. Table 4.1 summarizes the largest Lyapunov exponent calculation for each region. We should also keep in mind that the largest exponent can vary

Table 4.1: Largest Lyapunov Exponents for APM Chaos

Region 1: $l = 16.258$	Region 2: $l = 16.71$	Region 3: $l = 16.722$
λ_1 [bits/sec]	λ_2 [bits/sec]	λ_3 [bits/sec]
0.24	0.14	0.15

within each chaotic region of the bifurcation diagram, since each new fiber length describes a different system.

As done in Section 4.2.2, we also observed the main and external cavity pulse structure for chaotic APM operation, around $l \sim 16.25$. Figure 4.20 shows the complex structure across the peak of the pulses. In fact, comparing this figure with Figure 4.9, we notice that the chaotic pulses also alternate between high and low pulse amplitudes, because the chaotic regions are still two, separate branches on the bifurcation diagram. In contrast to the period-two case where every second pulse is identical, all of the pulses in the chaotic region are different, reflecting chaotic pulse structure. Conclusively demonstrating that these pulses indeed have chaotic structure would of course involve further careful analysis of the pulse envelope evolution with time.

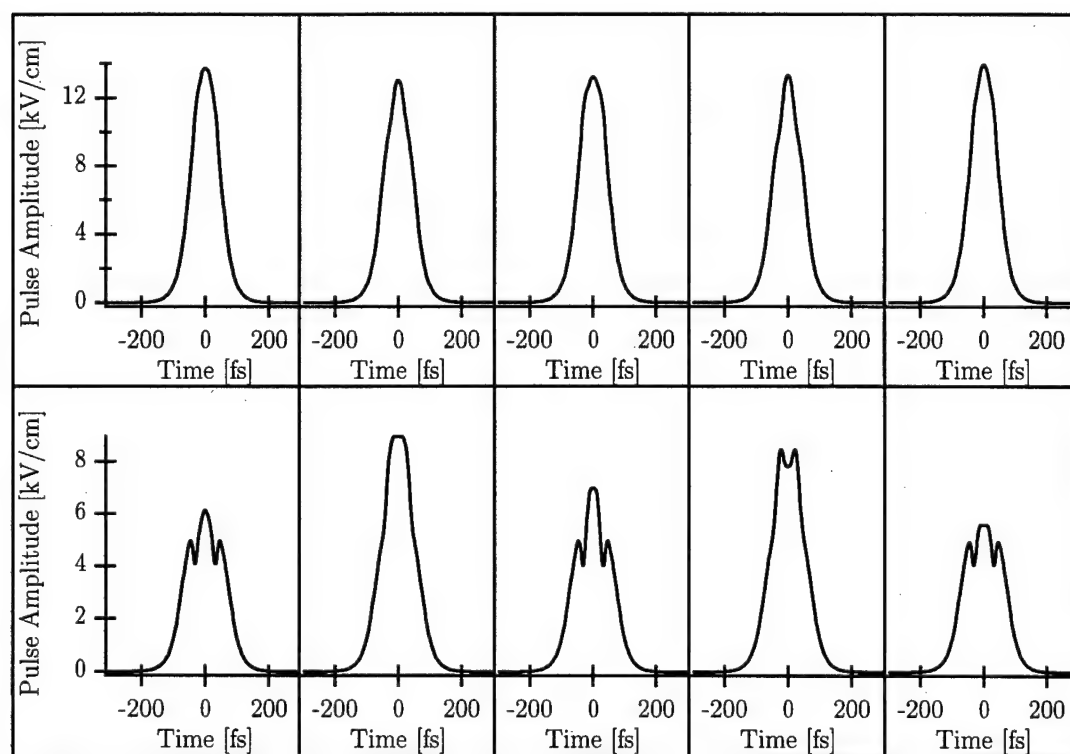


Figure 4.20: Chaotic Pulses in the main (upper row) and external (lower row) APM cavities, for 5 successive iterations with a fiber length of 16.25 cm.

4.2.4 Routes to Chaos

In discovering the phenomena of chaos in the APM laser, we must take a moment to think about the underlying dynamics which lead to this behavior. The means by which a system changes from a stable cycle to chaos is termed the *route to chaos*, and is one of the more fundamental properties of chaotic systems. As more and more scientists explore the nonlinear dynamics of systems, certain trends have begun to emerge. Four common routes to chaos have been identified and studied in real systems:

- 1) *Period-doubling*: the most commonly encountered route, where a period-one cycle bifurcates into period-two, four, eight, etc. before exhibiting chaos. This is the route encountered in the logistic map, seen in Figure 3.14. Each period-doubling involves the destabilization of the single state, concurrent with the emergence of two, new stable states, a process known as a pitchfork bifurcation (see Section 3.2 for a discussion of bifurcations). Thus, the system continues to period-double up to period- ∞ , which is essentially aperiodic (chaotic).
- 2) *Intermittency*: this is a process where, as the bifurcation parameter moves close to the chaotic regime, short bursts of chaos begin to repeatedly appear in the system output. Note that the system has not yet entered the chaotic region, nor has the output become completely chaotic. One can visualize a trajectory moving about on a periodic orbit in phase space, where a chaotic attractor is nearly stable. As the trajectory's orbit happens to wander close to the chaotic "ghost attractor," the trajectory may in fact be repeatedly pulled onto the attractor for a few cycles before escaping back onto the stable limit cycle. In this manner, as the bifurcation parameter is moved

ever closer to the chaotic region and the attractor becomes less and less unstable, the trajectory will tend to visit the attractor more often and for longer intervals of time, thus producing more frequent and longer bursts of chaos in the system output.

- 3) *Quasiperiodicity*: a system containing a stable torus defined by two incommensurate frequencies can destabilize as the nonlinearity is increased, either transitioning straight into chaos, or forming a three-torus if another characteristic frequency becomes involved. In this case certain perturbations can destabilize the three torus into chaos. It is also possible with a stable quasiperiodic orbit to undergo phase locking (where one frequency is pulled to oscillate as a harmonic of the other) as the nonlinearity is increased, before transitioning to chaos.
- 4) *Crisis*: this route is characterized by a sudden change in the system's attractor, especially where the sizes of the attractor before and after the crisis are disparate. As an example, considering the logistic map of Figure 3.14 near $r = 4$. For $r < 4$, the system rests on a stable chaotic attractor, while for $r > 4$, the orbit stays within $[0,4]$ for a few cycles, then falls toward $-\infty$. Thus, moving the parameter r across the value 4 from above causes the abrupt convergence to a stable chaotic attractor. In a similar manner, from the same figure we see the stable period-three window first period-double, then transition to three, separate chaotic regions. Just beyond this, the three chaotic regions suddenly transition via *internal* crisis to one, much larger chaotic attractor. The main characteristic of a crisis is *transient behavior* which can be summarized as follows. Even though a chaotic attractor destabilizes after a crisis, the system trajectory will remain on this attractor

for some finite number of orbits before moving to the new stable fixed point, limit cycle, or attractor. In other words, the system will exhibit a *chaotic transient* before settling onto the new, stable orbit.

Although these four routes have been identified and studied, they are by no means an exhaustive list of possible transitions to chaos. They merely serve to provide models for transitions in real systems, which quite often exhibit varied combinations of all the known routes.

In considering the APM laser bifurcation diagram of Figure 4.10, the initial period-one behavior is followed by an cascade of period-doubling bifurcations, and the laser thus follows the period-doubling route to chaos, much like the logistic map in Figure 3.14. In the middle of the first chaotic region, around a fiber length of 16 cm, we can also see a region of period-three behavior, again like the logistic bifurcation diagram.

Around a fiber length of 16.3 cm, the laser output suddenly drops from chaos into period-two behavior. The drastic change (disappearance) of the attractor would indicate a crisis, and further proof can be obtained from a time series of the output. Figure 4.21 shows three versions of an attractor reconstructed from 32000 iterations of the APM simulator with a fiber length of 16.3 cm. The simulator was preiterated 1000 times before recording output values. Plot (a) shows three-space reconstructed from 16000 output energies, which looks just like the chaotic attractor of Figure 4.12. Plot (b) is the same as (a), with the first 1250 iterations of the time series removed from the plot, yielding a much more "sparse" attractor. Plot (c) is also the same as (a), with the first 2500 iterations of the time series removed, revealing the correspondingly small cluster of periodic behavior present beyond the crisis. The initial chaotic orbits in Figure 4.21 comprise a chaotic transient.

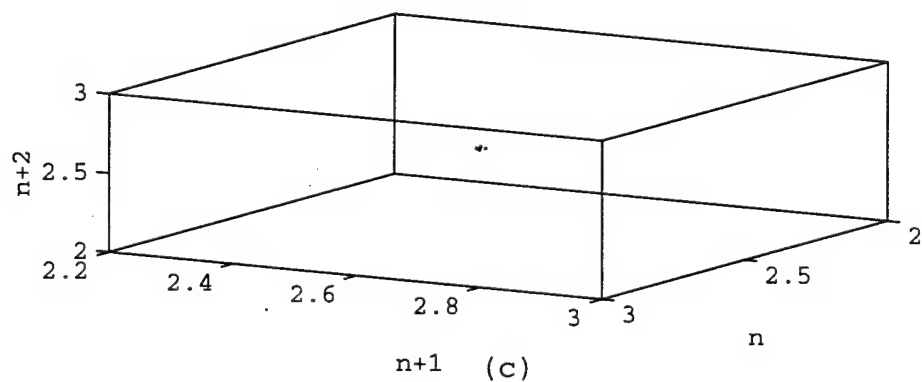
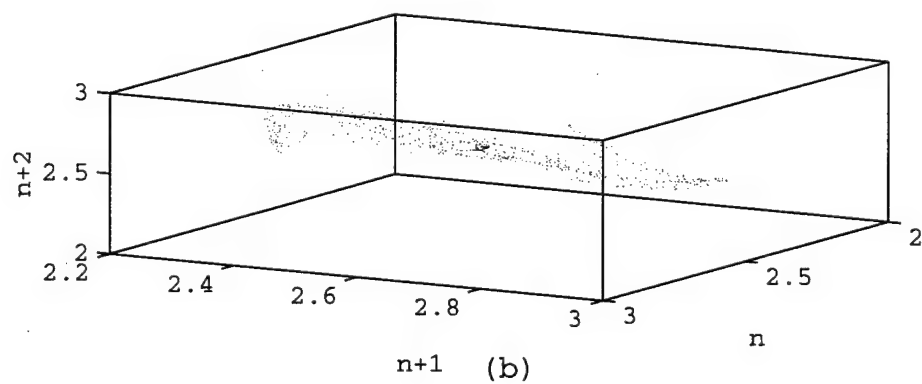
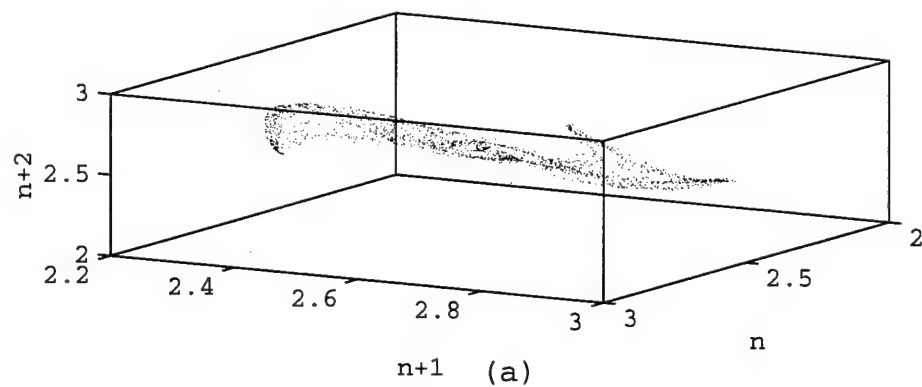


Figure 4.21: Chaotic Transient in the APM Output Near $l = 16.3$ cm: (a) shows iterations 1–16000, (b) shows 1251–16000, and (c) shows 2501–16000

Combined with the sudden change in the bifurcation diagram of Figure 4.10, this chaotic transient offers strong proof that the transition at $l = 16.3$ cm is indeed a crisis.

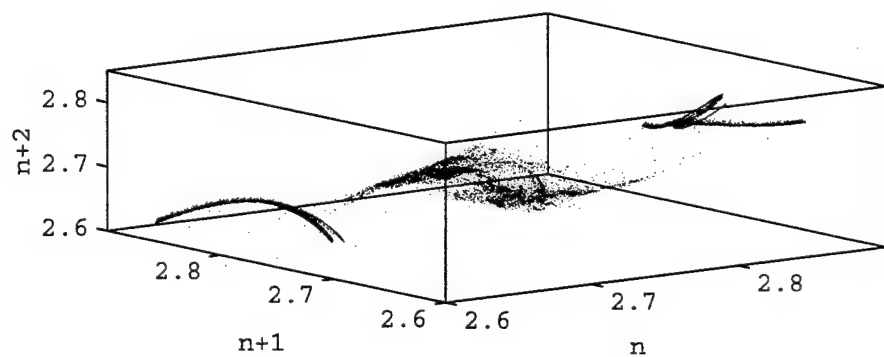
In a similar manner, the bifurcation diagram of Figure 4.10 displays another abrupt change, or crisis in dynamics around $l = 16.72$ cm. Figure 4.22 shows a reconstruction of a laser output time series for $l = 16.72$ cm, after 4000 preiterations. In plot (a) we see three co-existing attractors, representing a reconstruction of 12000 simulator iterations. These three attractors are from both sides of the crisis transition, and look the same as those in Figures 4.14, 4.16, and 4.17. In plot (b) the first 4000 iterations have been omitted, and the middle unstable attractor looks more sparse. In plot (c) the first 8000 iterations have been omitted, and the middle attractor has disappeared completely. This transient chaos provides reasonable proof that the transition at $l = 16.72$ is a crisis.

Identification of the period-doubling route to chaos in the APM laser is a significant finding in the characterization of the system. Currently, there are no published results exploring the route in detail for the APM configuration, nor are there any studies providing evidence of crises. Although more work must be done to conclusively verify the findings of this thesis, the results presented here represent the first theoretical characterization of the APM laser dynamics.

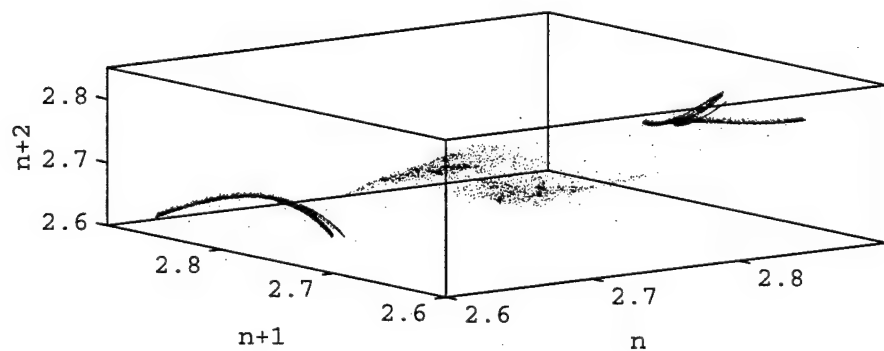
4.3 Exploring Parameter Space

4.3.1 Fiber Coupling Variations

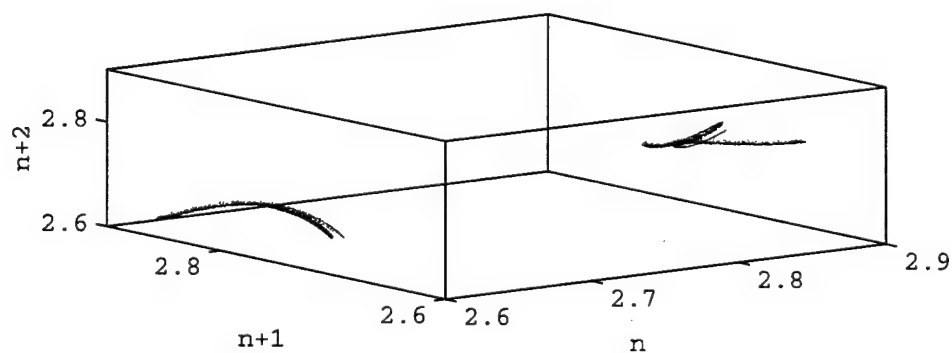
In varying the fiber coupling in the APM laser, we managed to create enough nonlinearity to cause a system bifurcation with increasing fiber length. The fact



(a)



(b)



(c)

Figure 4.22: Chaotic Transient in the APM Output Near $l = 16.72$ cm: (a) shows iterations 1–12000, (b) shows 4001–12000, and (c) shows 8001–12000

that period-doublings occur when the fiber couplings are varied indicates that the fiber length is not the only bifurcation parameter. We can run the simulation varying both γ_1 and γ_2 equally, while holding a fixed fiber length of 15 cm. Figure 4.23 shows the results of this simulation, where the laser indeed bifurcates as the couplings are increased.

This bifurcation diagram looks very similar to the fiber length bifurcation diagram of Figure 4.8. Figure 4.24 shows a magnification of the period-doubling and chaotic regimes. The period-doubling and crises in the fiber coupling diagram occur just as for the fiber length bifurcation diagram, and the only major difference is the unstable region beyond the second crisis at $\gamma_1 = 0.315$. Rather than exhibiting period-four, this region only shows underlying period-two, and additionally does not reverse bifurcate back to a stable periodic orbit.

Performing the same analysis on this chaotic region ($\gamma_1 > 0.315$) as those in the fiber length bifurcation diagram, we see in Figure 4.25 that the Abarbanel false-nearest-neighbor algorithm requires a four-dimensional embedding dimension.

Even though the proper embedding dimension is four, there are only a small amount of false neighbors for three dimensions, and we can therefore reconstruct the attractor in three dimensions for a rough visual comparison to those in Figures 4.12–4.19. Figures 4.26 and 4.27 show the results of the three-dimensional reconstruction.

In order to confirm that this region is indeed chaotic, we can also use the Wolf algorithm to determine the largest Lyapunov exponent, as in Section 4.2.3. Using an attractor reconstructed in *four* dimensions, a minimum initial displacement of $\sim 10^{-5}$ and a “largeness” condition on the final displacement of $\sim 10^{-2}$, the Wolf code produced a largest exponent of $\lambda = 0.31$ bits/sec. This positive exponent

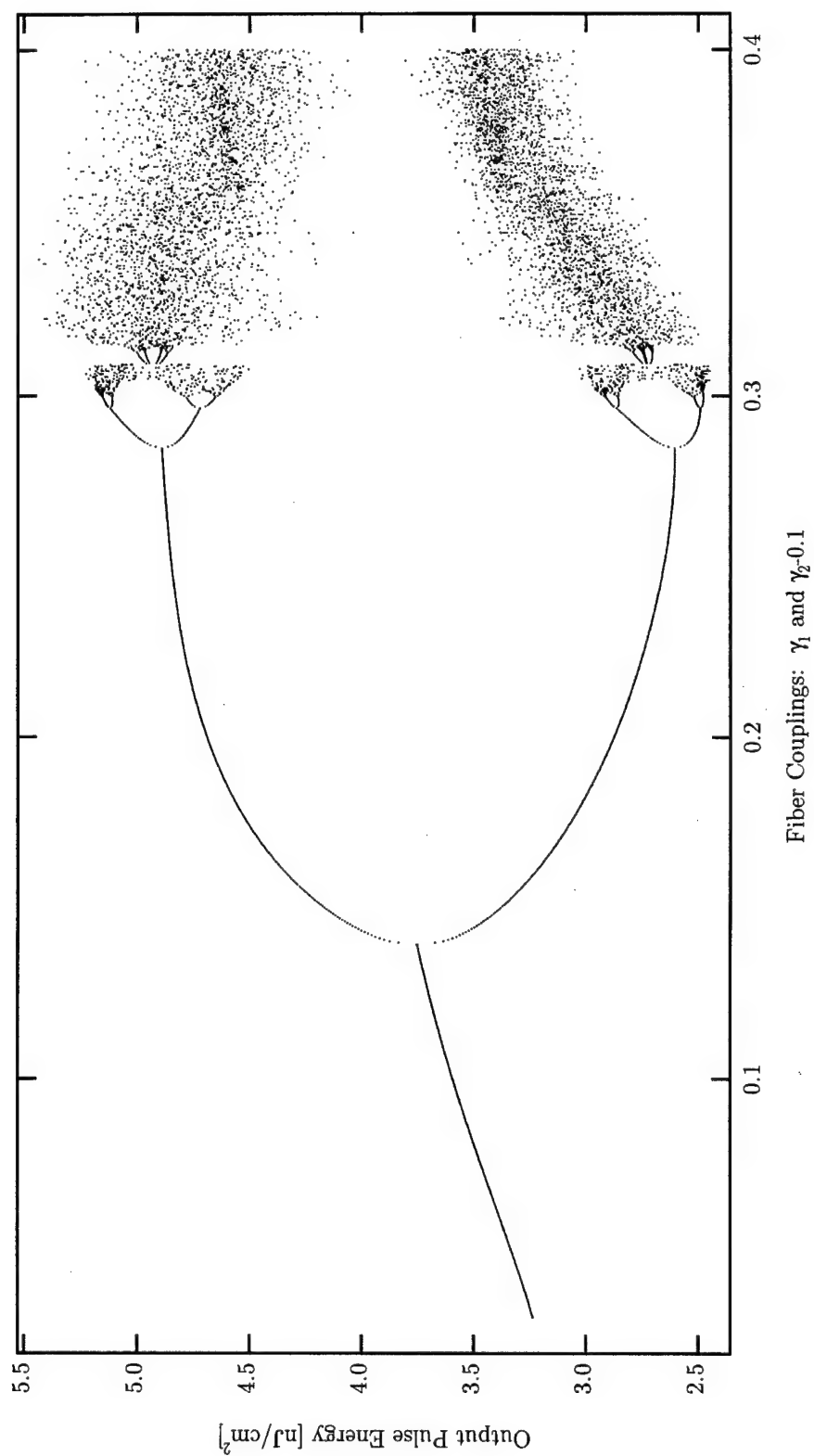


Figure 4.23: The APM Fiber-coupling Bifurcation Diagram: a plot of output pulse energy versus forward and backward fiber couplings, for a fiber length of 15 cm.

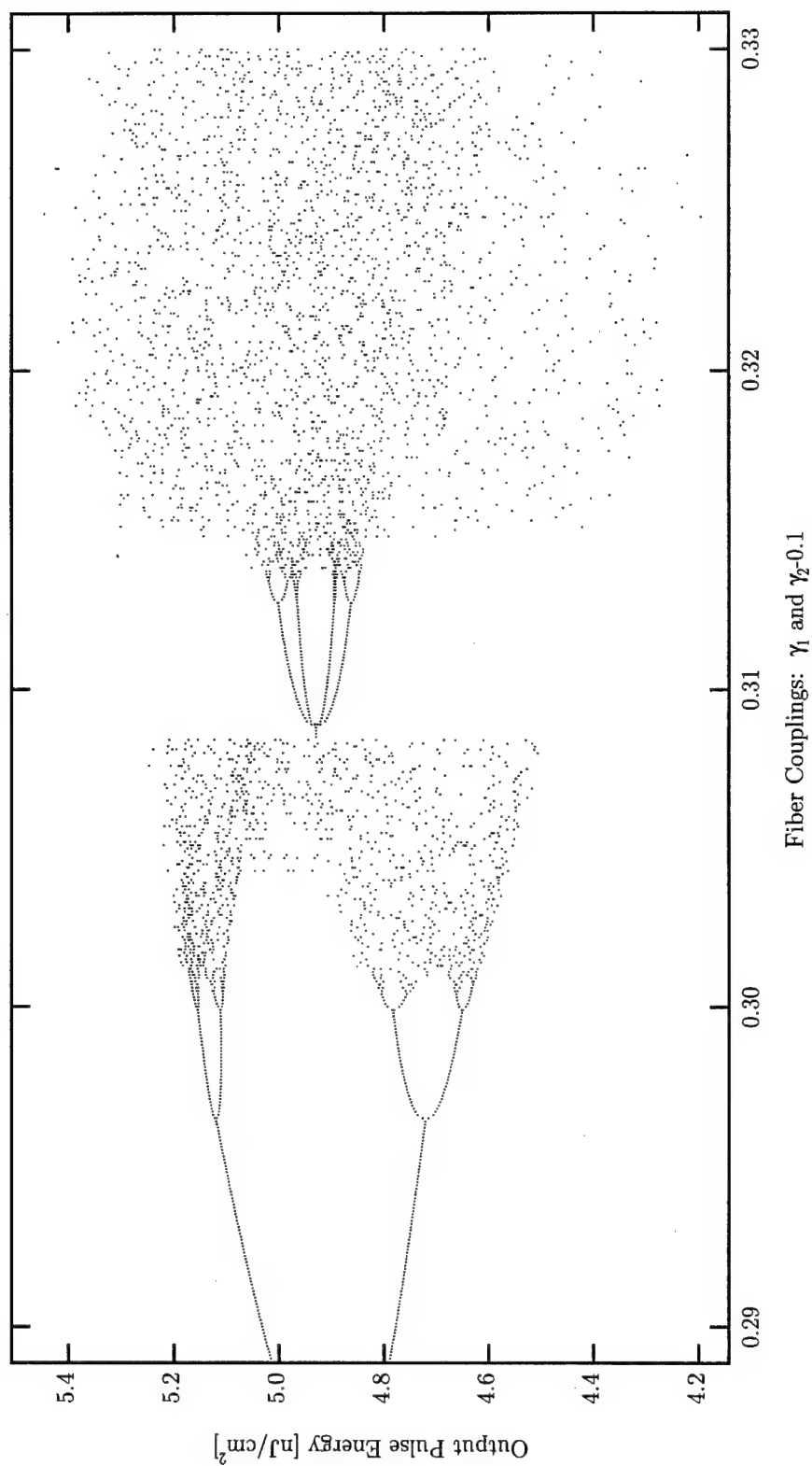


Figure 4.24: A Magnified Fiber-coupling Bifurcation Diagram: a plot of output pulse energy versus forward and backward fiber couplings, for a fiber length of 15 cm.

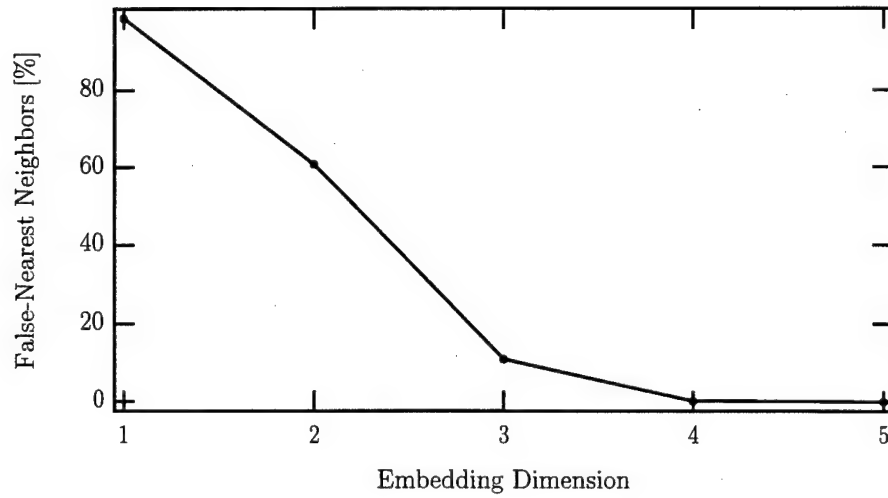


Figure 4.25: Embedding Dimension Calculation for Chaos in Figure 4.23, $\gamma_1 > 0.315$

indicates that the region is indeed chaotic.

4.3.2 Gain Variations

In light of Figure 4.23, we might well wonder what other parameter variations cause changes in the APM laser dynamics. Gain is perhaps the next most obvious candidate. Figure 4.28 shows a bifurcation diagram for the APM laser under variation of the model parameter G_0 , which is proportional to the pumping intensity of the laser system. The fiber length is fixed at 20 cm, and the fiber couplings are $\gamma_1 = 0.5$ and $\gamma_2 = 0.6$, corresponding to the small-coupling regime we studied for fiber length bifurcations in Section 4.2.1.

This diagram exhibits the same quasiperiodic region as the fiber length bifurcation diagram of Figure 4.4. Figure 4.28 has a much more positive slope, simply because the gain more strongly affects the output energy of the laser. Figure 4.29 shows 3 quasiperiodic return maps, for small signal gain values of 2.5, 2.6, and 2.7. The only new feature in Figure 4.28 is the collapse of the quasiperiodic region,

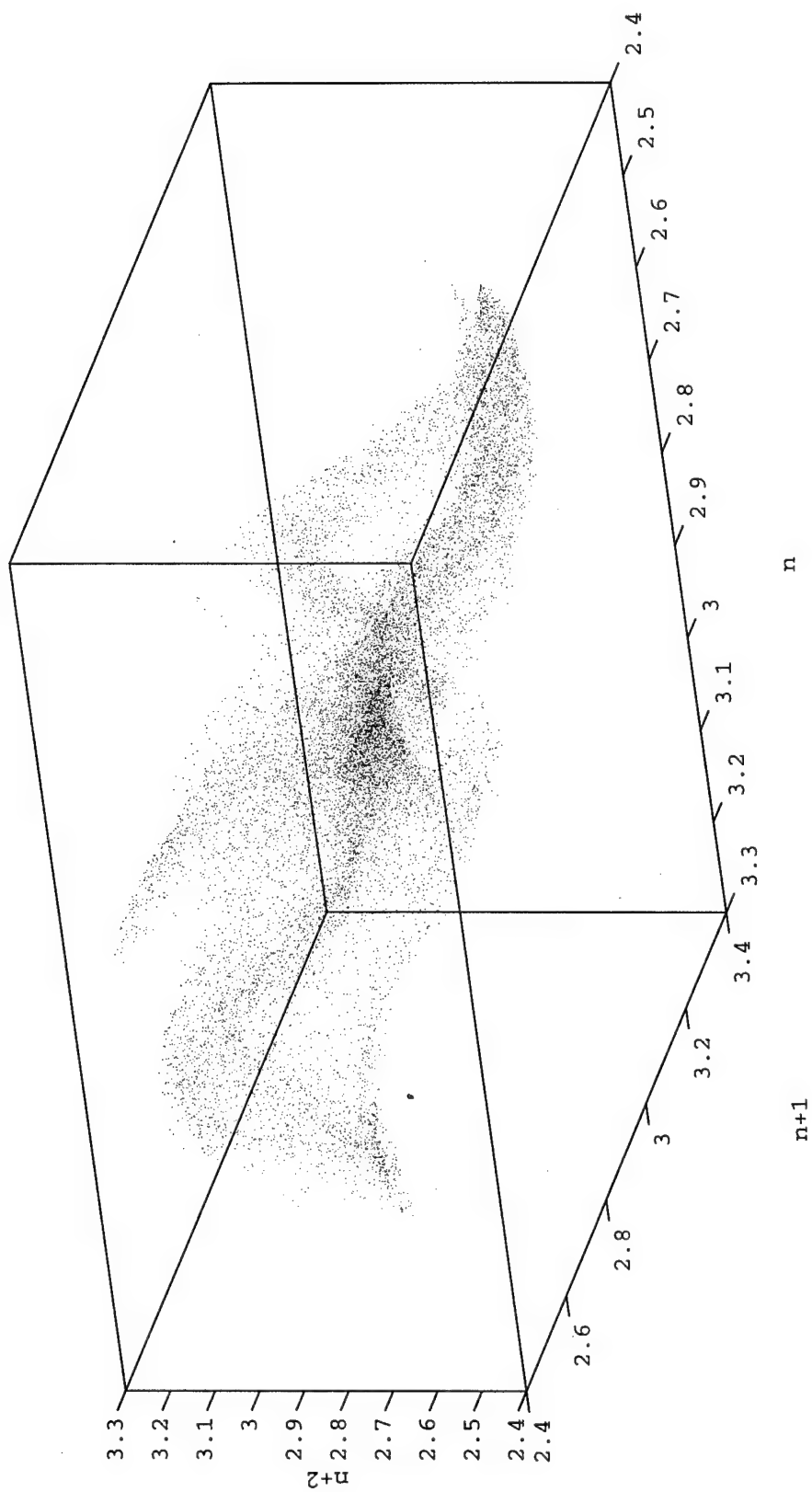


Figure 4.26: An APM Chaotic Attractor: one of two at $\gamma = 0.316$

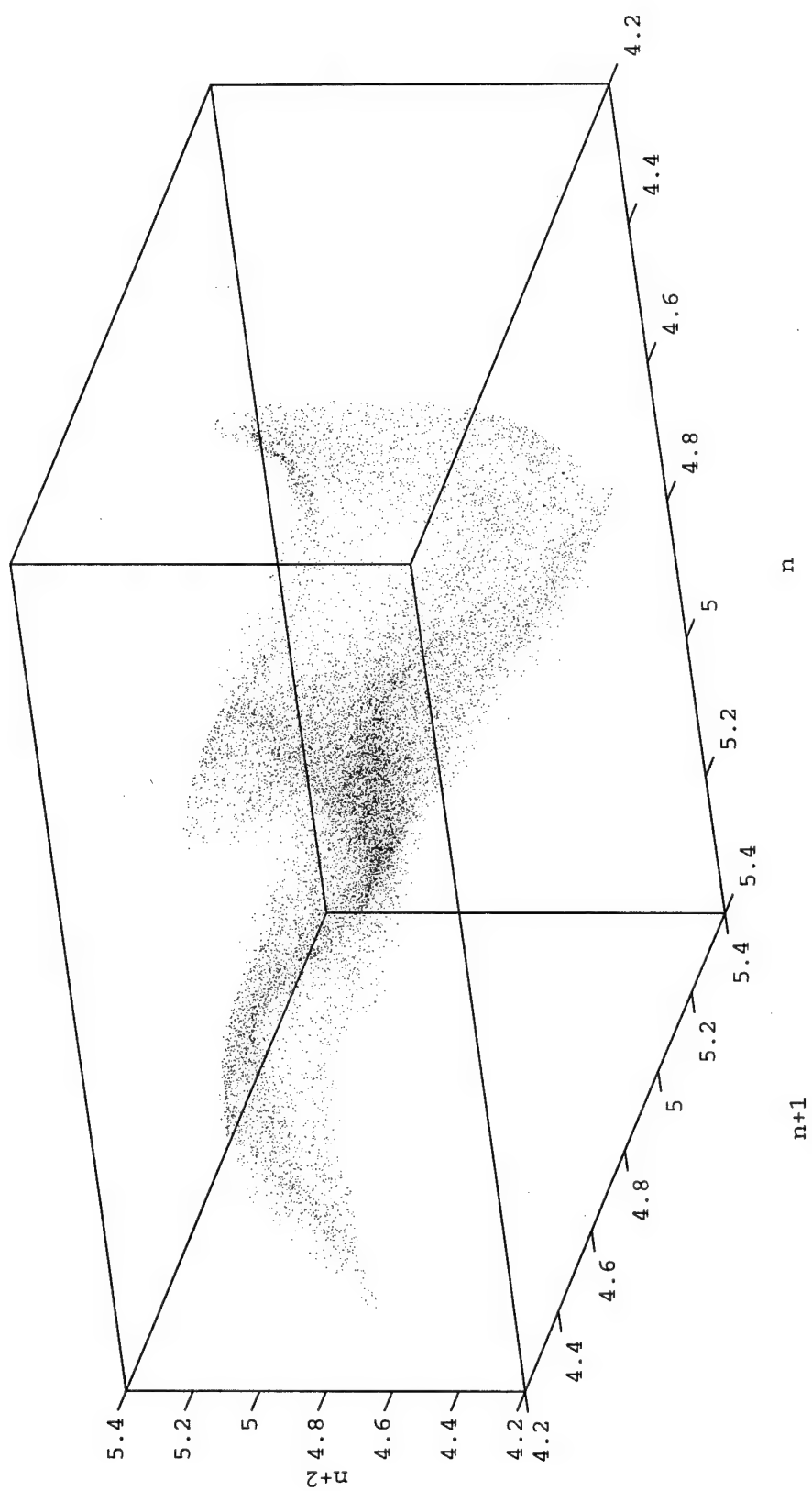


Figure 4.27: An APM Chaotic Attractor: two of two at $\gamma = 0.316$

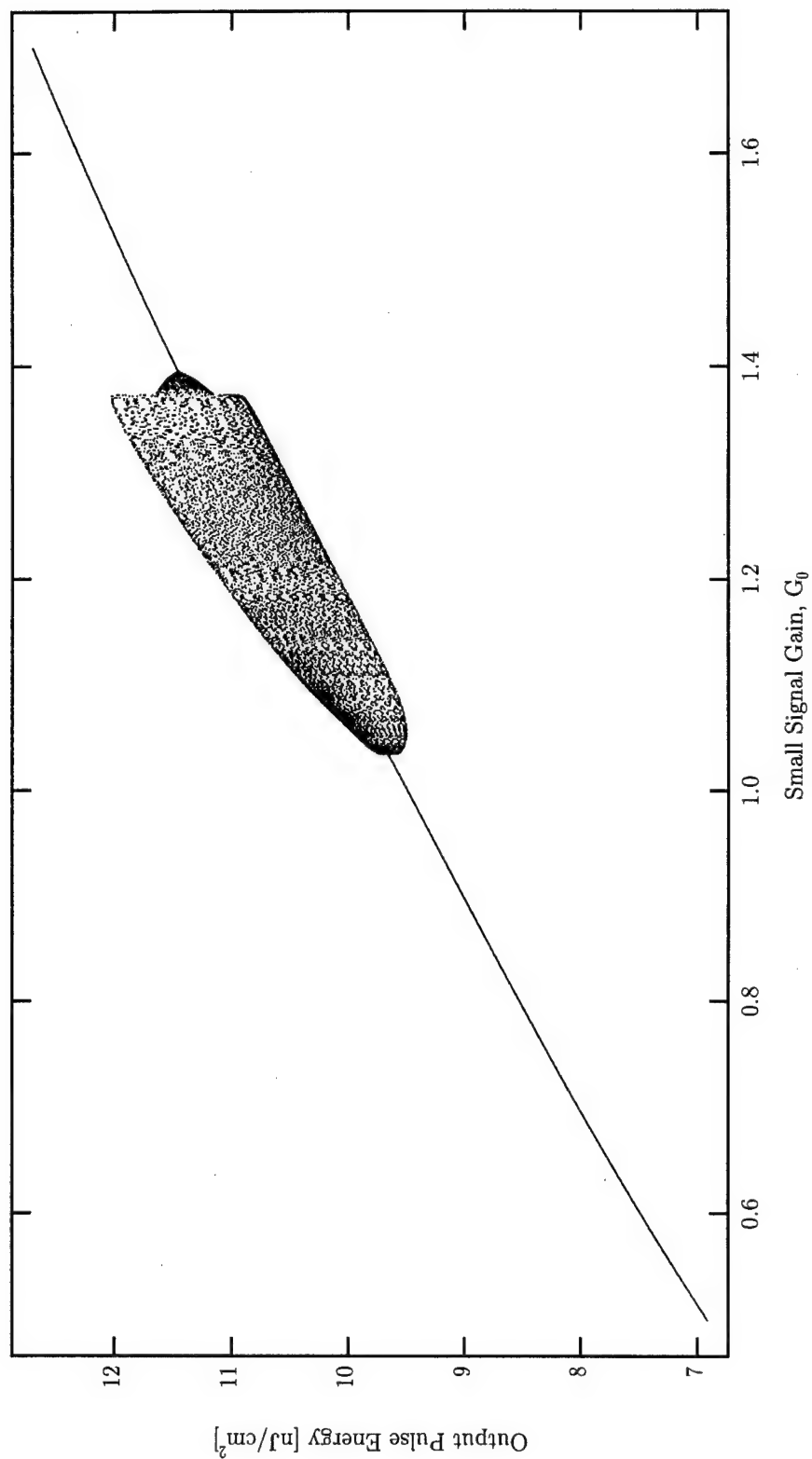


Figure 4.28: A Gain Bifurcation Diagram for the APM Laser: output pulse energy versus small signal gain, G_0 , for a fiber length of 10 cm, and fiber couplings of $\gamma_1 = 0.5$ and $\gamma_2 = 0.6$.

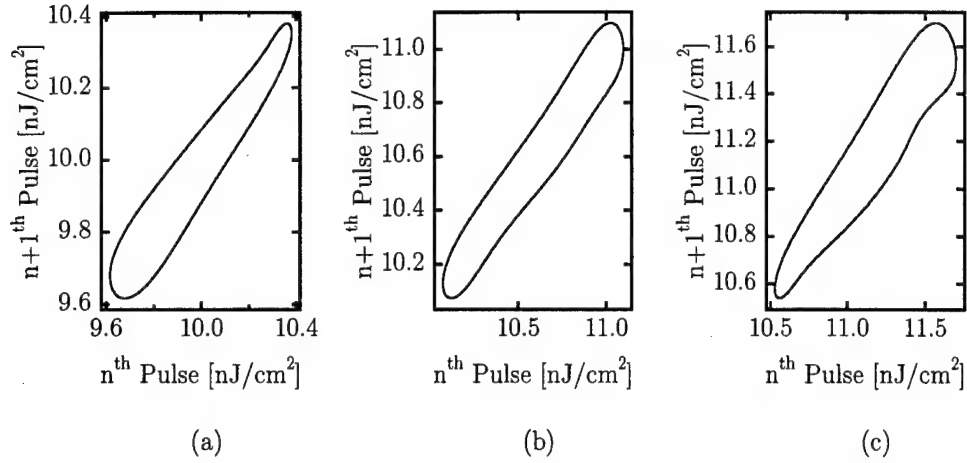


Figure 4.29: Quasiperiodicity in the APM output for 3 different small-signal gains: (a) $G_0 = 2.5$ (b) $G_0 = 2.6$ and (c) $G_0 = 2.7$

giving way to stable period-one behavior at high gains.

Similar to the fiber length bifurcation diagrams, the gain bifurcation diagram will produce drastically different dynamics when we increase the fiber couplings. Figure 4.30 shows the gain bifurcation diagram for the increased fiber couplings, $\gamma_1 = 0.8$ and $\gamma_2 = 0.9$, and a fiber length of 7 cm. Again, the gain diagram produces results almost identical to those of the fiber length bifurcation diagram in Figure 4.8 for increased couplings. The laser output first period-doubles into chaos, falls back to period-two with a crisis, again period-doubles into chaos, transitions to a new chaotic region with another crisis, then finally reverse bifurcates back to period-two. Figure 4.31 shows a magnified view of the bifurcating region of Figure 4.30.

Figures 4.30, 4.23, and 4.8 demonstrate some of the variations of the APM laser under limited parameter variations. The APM laser has a multi-dimensional parameter space (see the model development of Chapter 2), and variations in most of these parameters are strongly coupled. Indeed, the fiber length, coupling, and

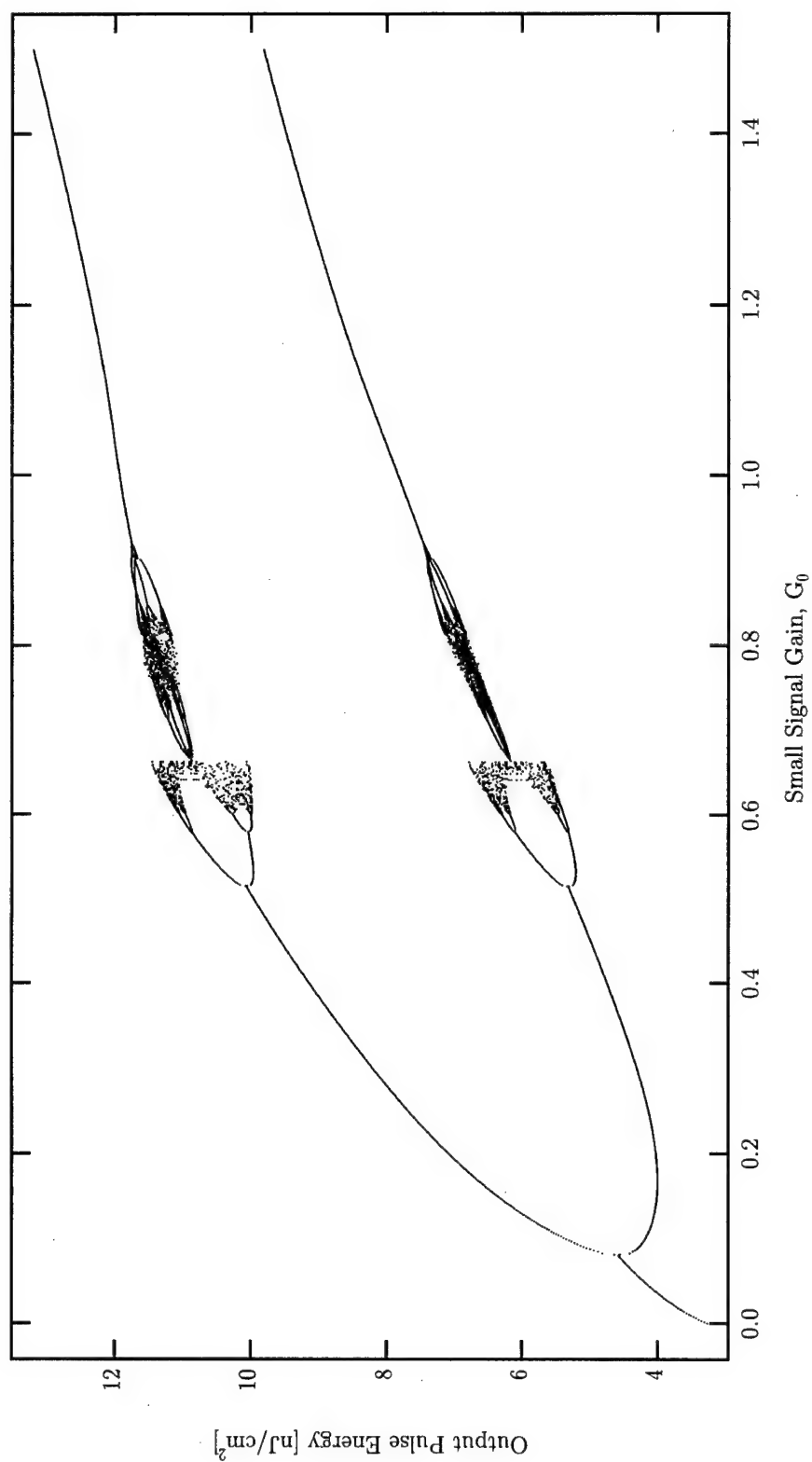


Figure 4.30: An Increased Fiber Coupling Gain Bifurcation Diagram: output pulse energy versus small signal gain, G_0 , for a fiber length of 7 cm, and fiber couplings of $\gamma_1 = 0.8$ and $\gamma_2 = 0.9$.

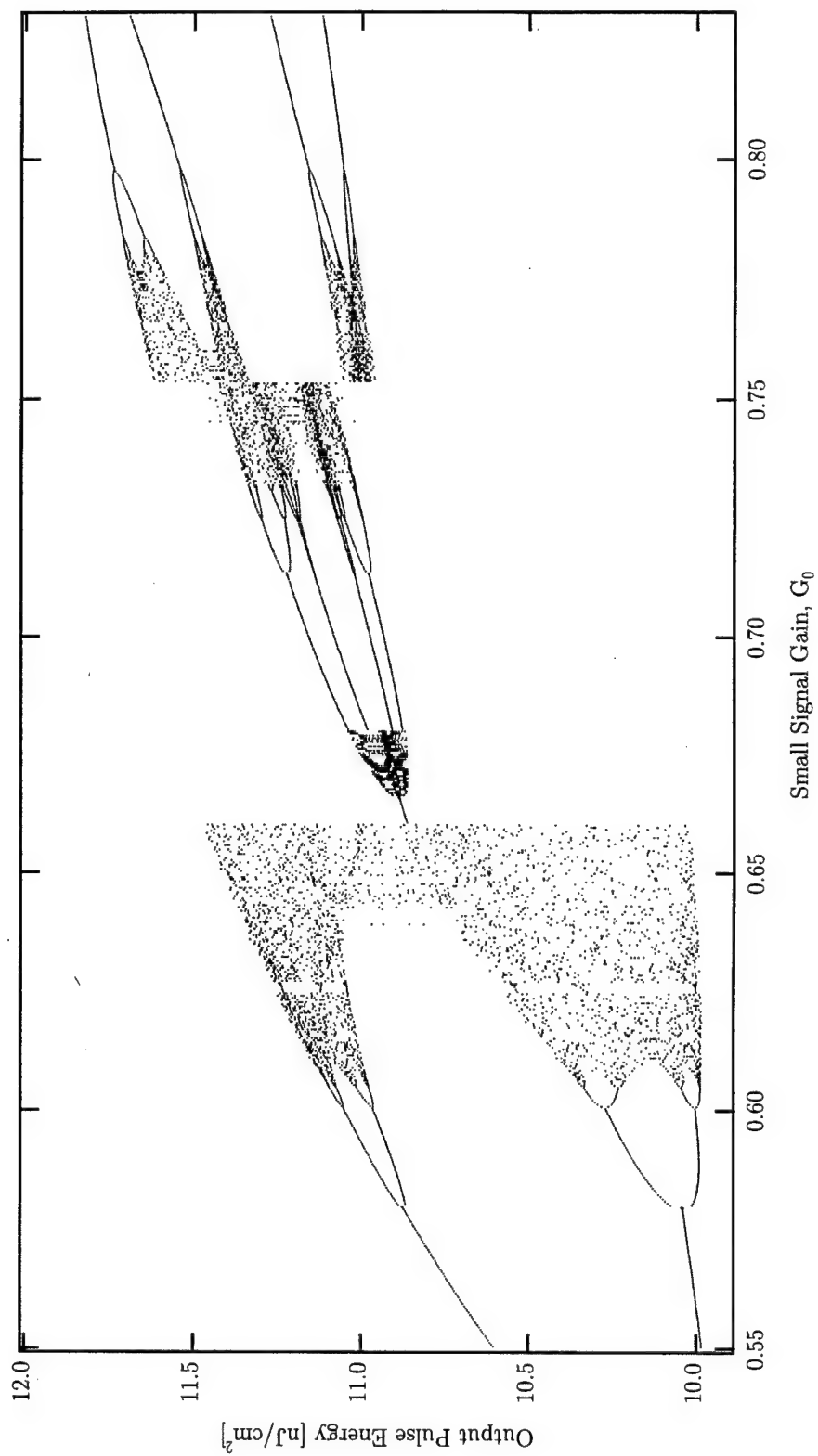


Figure 4.31: A Magnified View of Figure 4.30: output pulse energy versus small signal gain

the laser gain all affect the nonlinearity, although some more directly than others.

By varying only these three parameters, the laser has conclusively demonstrated quasiperiodic behavior, the period-doubling route to chaos, and crisis transitions. This thesis represents the first identification of the period-doubling route in the APM laser, and the first verification of true crisis behavior. A more detailed study of these and other parameter variations can and will undoubtedly be performed, although this will require an immense amount of time and memory in computer simulations.

Chapter 5

Conclusion

5.1 Model Limitations

The model developed in Chapter 2 and analyzed in Chapter 4 can be a very powerful tool for APM laser design, especially as applied to the avoidance or enhancement of chaotic behavior. As with any numerical model, however, we should be aware of some of the limitations.

First of all, certain physical effects were completely omitted from the model, and could modify operation if considered. These include the following:

- 1) *Gain Saturation*: although gain saturation analysis was performed in Chapter 2, only a pulse-averaged saturation was included in the numerical model, mainly because time-dependent saturation will cause the pulse to “walk forward” in time. This was avoided as it would require the extra time-consuming step of repositioning the pulse in the center of the array window every several iterations. The time-dependent saturation should only serve to slightly distort the pulse shape however, and cause some asymmetry in the simulation results.

- 2) *Dispersion*: dispersion was not explicitly included in the model since the optical fiber used in experimental systems is generally dispersion-shifted. A more rigorous approach could include the small dispersion contributions from the laser optics as well as the NaCl crystal and higher-order dispersion in the fiber, or even the more general case of non-dispersion-shifted fiber.
- 3) *Sync-pumping*: in many APM lasers, the gain medium is sync-pumped, which means that the pump laser which supplies energy to the gain crystal is itself mode-locked so as to provide gain only for small intervals of time, thereby encouraging modelocking simply through gain modulation. This type of system requires that both of the APM laser cavities be exactly matched in length to the pump laser cavity, so that the pulses in the APM laser will pass through the gain coincidentally with the pump pulses. Although this is a common APM laser design, many researchers are moving toward self-starting APM operation [30], which uses a CW pump, as modeled in this thesis. In addition, commercially available mode-locked lasers in the $1.06\text{ }\mu\text{m}$ region yield fairly large ($\sim\text{ ps}$) pulses, which, on the time scale of a 100 fs APM pulse, is only a small perturbation to a CW gain.

Approximations and omissions notwithstanding, the model parameters must be constrained within certain limits to avoid erroneous simulation behavior. Two particular situations involve an overly large external cavity pulse bandwidth, resulting from very high levels of nonlinearity (long fiber length, high fiber coupling, large laser gain). In the first case, the fraction of laser pulses which circulates in the external cavity experiences a cumulative increase in pulse bandwidth from multiple passes through the fiber. Since only a small component of the external cavity pulses actually couples back into the main cavity to be bandwidth-limited

by the tuner plate, some percentage of the chirped pulses will immediately circulate back into the fiber and experience more phase chirp. If the fiber coupling and length are large enough, this repeated phase chirp can cause an increase in pulse bandwidth beyond 100 THz. In the time domain, this corresponds to oscillations on the order of the optical carrier frequency (187.5 THz), at which point the distinction between the optical wave and its envelope becomes blurred; i.e., the situation is non-physical. Worse yet, the center (peak) of the pulse envelope can become extremely narrow, to the point of being represented by a single sample in the numerical simulator, as shown in Figure 5.1. In this case, aliasing has occurred,

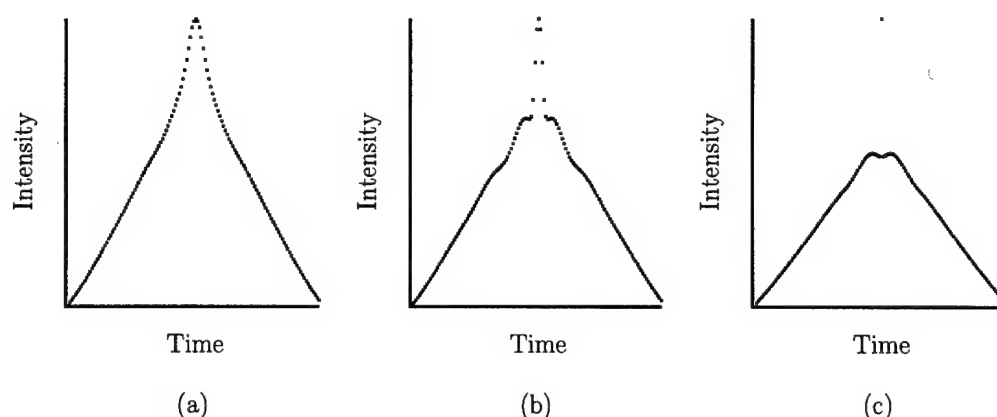


Figure 5.1: Simulator Pulse Discontinuity Due to Extreme Bandwidth. The central portion of a pulse from the APM simulations shows progressively worse compression in (a) and (b), and the resulting discontinuity in (c)

and the discontinuous pulse envelope results in a drastically altered pulse integral (energy). Thus, the simulator displays a marked discontinuity in the bifurcation diagram, as shown in Figure 5.2.

Experimentally, this situation should never arise, because other optical components would prevent the pulse bandwidth from growing too large. For example, a typical high reflector in the external cavity has the wavelength profile shown in

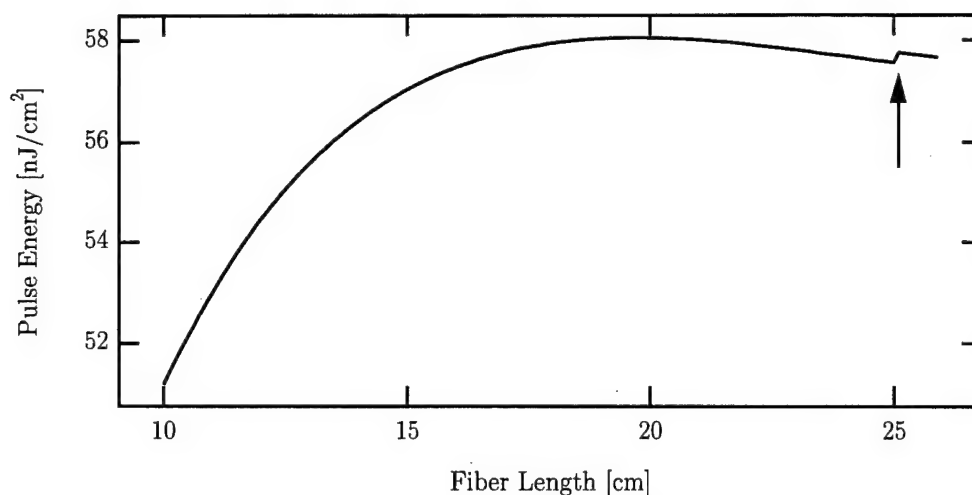


Figure 5.2: Discontinuity in the APM Simulation Output

Figure 5.3. The high reflectivity region reflects a typical bandwidth of only about

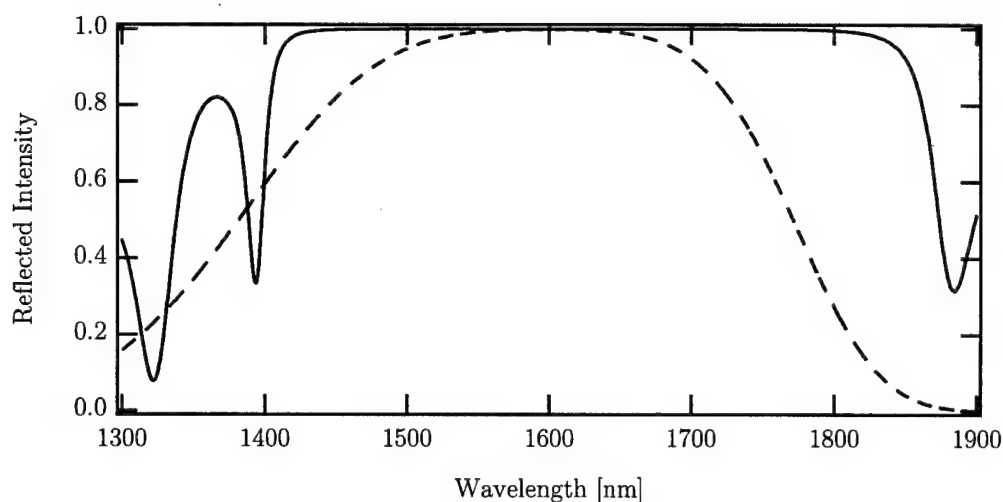


Figure 5.3: A Typical NaCl High Reflector: the solid curve represents the response of an actual NaCl laser mirror scanned with a spectrophotometer, and the dashed curve is the filter function used in the numerical simulations

400 nm. A simple combination of error functions,

$$M(\lambda) = \{\text{Erf}[\alpha(c/\lambda - \nu_0 + \delta\nu)] + 1\} \{-\text{Erf}[\alpha(c/\lambda - \nu_0 - \delta\nu)] + 1\} / 4 \quad (5.1)$$

can easily approximate this mirror transmission, as shown by the dashed curve of Figure 5.3. In (5.1), $\delta\nu$ is the half-width at half-maximum (HWHM), ν_0 is the

center frequency, and α is a constant related to the steepness of the mirror profile (in Figure 5.3, $\alpha = 50$). The dashed filter of Figure 5.3 was in fact applied to the external cavity in the simulations of this thesis to prevent the runaway of pulse bandwidth. This “mirror” filter was centered at 187.5 THz with a FWHM of 45 THz (which corresponds to ~ 400 nm of bandwidth), positioned in the external cavity after the fiber, and numerically implemented just as the filters of Section 2.4.2. With the addition of this filter, the simulations showed no indication of abnormal accumulated bandwidth, and the pulseshapes as well as the bifurcation diagrams showed no discontinuities.

The second case involving an overly large external cavity bandwidth results from the nature of the iterative model (2.51). The total accumulated phase chirp from one pass through the fiber is applied to the pulse in a single multiplication. Since the amount of phase chirp scales with the nonlinearity appearing in the exponent of (2.51), very high nonlinearity can result in multiple- π of phase across the pulse. One pass through the fiber could conceivably produce enough phase to again cause oscillations on the order of the carrier frequency, and thus aliasing in the simulation. This situation is different from the first case considered above, because the nature of the iterative model does not allow for bandwidth limitation *within* the fiber, and the mirror filter will therefore not correct the problem.

The solution in this case is to provide a detection mechanism for the overly large one-pass bandwidth. We can compare the pulse’s spectral content before and after filtering with the external cavity mirror, and look for significant differences. This involves simply taking the fft of the pulse before and after mirror filtering, and signalling an error when the integral of the filtered pulse spectrum varies from the unfiltered by more than 10%. With this check, all simulations can be kept within

the limits of “reasonable” bandwidth, meaning that no pulse acquires frequency components greater than 100 THz.

Without the bandwidth limiting measures described above, the APM simulator can produce drastically erroneous results, as shown in Figure 5.4. Results nearly

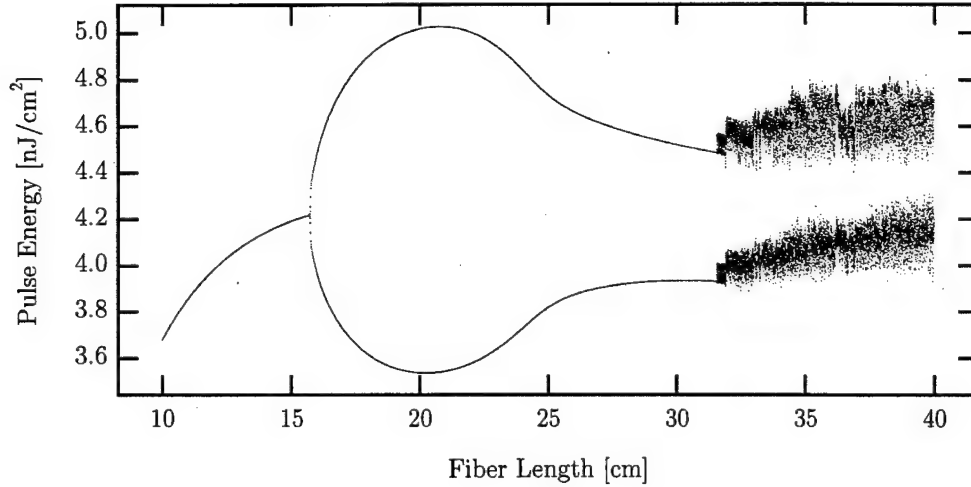


Figure 5.4: Erroneous Dynamics in the APM Bifurcation Diagram

identical to Figure 5.4 have actually been reported in past literature [2], and are most likely an artifact of overly large bandwidth.

5.2 Future Directions

5.2.1 Model Variations

Chapter 4 considered several parameter changes for the APM numerical simulations, but several more could be studied in the future. Of particular interest is the static phase mismatch, Φ_0 , between the main and control cavities. This parameter has historically been used for the active stabilization of the APM laser, since the cavity mismatch can be directly monitored by the average power in the control

cavity [31]. The phase mismatch would be an interesting parameter to vary, since it perturbs the control cavity power with a sinusoidal dependence. It also has the attractive property of being a readily variable parameter in the laboratory. Other researchers have examined the effects of varying a similar parameter for a passive ring resonator, and found behavior much like the fiber coupling bifurcation diagrams in Section 4.3.1 [32].

Other aspects of the APM laser simulations could also be changed, to explore more laser dependencies. Focusing in the gain crystal should have a strong effect on the laser dynamics, since this would affect the amount of saturation, and therefore the overall pulse energy within the main cavity. Even different configurations for the APM laser, such as the Michelson Interferometer scheme, could be explored with few modifications to the model. Finally, several hypothetical cavity configurations could be considered, to test the dynamics before spending the time and money necessary for an experimental effort.

5.2.2 Experimental Possibilities

Experimentally, the findings of this thesis present a large arena for research. First, verification of the different APM dynamics found in Chapter 4 presents an immediate area for study. Others have already begun to explore APM dynamics experimentally [2, 3], but no effort has been made to construct a bifurcation diagram, or explore actual output pulse profiles for period-two or larger behavior. Bifurcations with all the different laser parameters studied in this thesis should also be considered, and eventually, some of the routes to chaos verified experimentally. In addition, fiber couplings above the current experimental limits could be explored, perhaps by a different cavity design which could feature only a single

pass through the fiber.

Another direction for research is exploration of dynamical operation of the APM laser when mode-locking is assisted by a saturable Bragg reflector (SBR). An SBR consists of several quarter-wave layers of semiconductor, to form a Bragg stack high reflector. In the top layer, one or more quantum wells resides, with a band edge very near the desired lasing wavelength. Essentially, this top layer is a saturable absorber, which acts as loss for normal cavity intensities, but favors short, high-intensity light pulses which can quickly saturate the absorption, and reflect without loss. With this type of mirror in the cavity, several researchers have achieved a very robust, self-starting mode-locking [33]. In fact, when an SBR was used as a secondary element in a regeneratively mode-locked Ti:Sapphire laser, reproducible self-starting behavior was reported [34]. Generally, the SBR so favors pulsed behavior that mode-locking is stable for a greater range of parameters. This technique could be applied to the APM laser, which has historically required a feedback loop to achieve stable mode-locked behavior. With an SBR as a secondary element, the APM laser may mode-lock for a wider range of parameters, or even display greater stability for the current parameter ranges. In either case, the study of nonlinear APM laser dynamics could greatly benefit from a larger accessible parameter space.

Beyond the study of the APM laser, efforts should be made to control the dynamics for some useful purpose. In 1990, Edward Ott *et al.* explained how to control unstable periodic orbits within a chaotic system [35]. Since a typical chaotic attractor contains an infinite number of unstable periodic orbits, with the proper control, one could exploit any one of these orbits with a small perturbation, thus making a single system capable of many different types of output. The idea

behind such control involves reconstructing an attractor as per Section 3.4.3, then locating a desired periodic orbit (in the case of a map, this would be equivalent to a fixed point for period one, or a fixed set of n points for period- n). Next, one creates a set of linearized equations in the neighborhood of the fixed point, by observing the shift in the fixed point when a system control parameter is perturbed. Now, when the chaotic system trajectory enters a small neighborhood of the desired fixed point, one perturbs the control parameter as dictated by the linearized equations to force the trajectory onto the stable manifold of the fixed point. For a small enough neighborhood, such perturbations are small, and control is readily achieved.

Since this original proposal, E. Hunt has described a variation called *occasional proportional feedback* (OPF), which involves using a small fraction of the system output as feedback to alter the control parameter, whenever the trajectory falls in a neighborhood of the desired fixed point [36]. This technique has been successfully demonstrated in several systems, electrical and optical [37]. OPF control could be directly applied to the APM laser, by using some fast intracavity modulator (such as an electrooptic cell) to alter the trajectory based upon feedback from the output. Even more recently, Glorieux *et al.* proposed a method of control based upon delayed *continuous* feedback [38], which could be applied to the APM laser by an simple, small reflection of the output back into the APM cavity.

Control of the APM laser would first require that the laser experimentally exhibit chaotic output. This thesis presents a detailed model which will hopefully make design of the laser with chaotic dynamics in mind possible. Such control techniques, if successful, would result in an APM laser capable of a much larger range of output, in regions of parameter space where stable output was previously impossible.

Appendix A

ABCD Analysis of the NaCl

APM Cavity

To analyze the main laser cavity of Figure 2.1 with the dimensions specified in Figure 2.2 b, we can use ABCD matrix formalism as applied to laser oscillators [39, pp. 130–137]. First, to determine the cavity stability, we create a ray matrix for each element, then multiply these individual matrices in the order of a unit cell to arrive at a cavity matrix. Starting from the output coupler (far left) of Figure 2.2 b, we have

$$\begin{pmatrix} A & B \\ C & D \end{pmatrix} = \begin{pmatrix} 1 & d_1 \\ 0 & 1 \end{pmatrix} \begin{pmatrix} 1 & 0 \\ -\frac{1}{f} & 1 \end{pmatrix} \begin{pmatrix} 1 & d_2 \\ 0 & 1 \end{pmatrix} \begin{pmatrix} 1 & 0 \\ -\frac{1}{f} & 1 \end{pmatrix} \begin{pmatrix} 1 & d_3 \\ 0 & 1 \end{pmatrix} \times \\ \begin{pmatrix} 1 & d_3 \\ 0 & 1 \end{pmatrix} \begin{pmatrix} 1 & 0 \\ -\frac{1}{f} & 1 \end{pmatrix} \begin{pmatrix} 1 & d_2 \\ 0 & 1 \end{pmatrix} \begin{pmatrix} 1 & 0 \\ -\frac{1}{f} & 1 \end{pmatrix} \begin{pmatrix} 1 & d_1 \\ 0 & 1 \end{pmatrix} \quad (\text{A.1})$$

where d_1 is the distance from the output coupler to the left lens, d_2 is the distance between the lenses, d_3 is the distance from the right lens to the pump mirror, and f is the focal length of the lenses. The small effect of the NaCl index of refraction on the distance d_2 has been omitted for simplicity.

Carrying out this matrix multiplication (from right to left), we arrive at

$$\begin{pmatrix} A & B \\ C & D \end{pmatrix} = \frac{1}{f^4} \begin{pmatrix} 2d_1d_2^2d_3 - 2d_2f(d_1d_2 + 4d_1d_3 + d_2d_3) + 2[d_1d_2 - f(2d_1 + d_2) + 2f^2(3d_1d_2 + d_2^2 + f^2)][d_1d_2d_3 - f(d_1d_2 + 4d_1d_3 + 3d_2d_3) - 2d_1d_3 + d_2d_3] + f^2(d_1 + 4f^3(d_1 + d_2 + d_3) + f^4 d_2 + d_3)] \\ 2d_1d_2^2d_3 - 2d_2f(d_1d_2 + 2(d_2 - 2f) \times 4d_1d_3 + d_2d_3) + (d_2d_3 - d_2f - 2f^2(3d_1d_2 + d_2^2 + 2d_3f + f^2) 4d_1d_3 + 3d_2d_3) - 4f^3(d_1 + d_2 + d_3) + f^4 \end{pmatrix} \quad (\text{A.2})$$

The ABCD stability condition for laser oscillators is

$$\left| \frac{A + D}{2} \right| \leq 1 \quad (\text{A.3})$$

Given the values $d_1 = 120$ cm, $d_2 = 10.003$ cm, and $d_3 = 57.497$ cm from Figure 2.2 b, this becomes

$$0.959975 \leq 1 \quad (\text{A.4})$$

so the cavity is stable.

In order to determine the spot size throughout the cavity, we can examine the beam waist of a propagating zeroth-order Gaussian mode. The gaussian beam parameter, q , is defined as

$$q(z) = z + jz_0 \quad (\text{A.5})$$

where z_0 is called the *confocal parameter* and defined as

$$z_0 = \frac{\pi n w_0^2}{\lambda_0} \quad (\text{A.6})$$

The Gaussian beam parameter relates to the physical radius and curvature of the Gaussian beam as

$$\frac{1}{q(z)} = \frac{1}{R(z)} - j \frac{\lambda_0}{\pi n w^2(z)} \quad (\text{A.7})$$

where $R(z)$ describes the beam curvature, and $w(z)$ represents the beam waist, for any distance z in free space. From (A.7), we can obtain an expression for the beam waist,

$$w^2(z) = w_0^2 \left[1 + \left(\frac{\lambda_0 z}{\pi n w_0^2} \right)^2 \right] \quad (\text{A.8})$$

(A.8) describes the beam waist at any position z in free space, given the minimum beam waist, w_0 , which is just the waist at $z = 0$.

ABCD matrix formalism can be applied to Gaussian beam propagation [39] through

$$q(z_m) = \frac{Aq(z_m) + B}{Cq(z_m) + D} \quad (\text{A.9})$$

where $q(z_m)$ is the Gaussian beam parameter evaluated at $z = z_m$, just to the left of the first element of the unit cell used to calculate $(ABCD)$. This equation can be simplified by solving for q ,

$$0 = Cq^2 + q(D - A) - B \quad (\text{A.10})$$

$$\Rightarrow q = \left(\frac{A - D}{2C} \right) \pm \frac{\sqrt{(D - A)^2 + 4BC}}{2C} \quad (\text{A.11})$$

$$= \left(\frac{A - D}{2C} \right) \pm \frac{1}{C} \left[\left(\frac{D - A}{2} \right)^2 + BC \right]^{1/2} \quad (\text{A.12})$$

Using the fact that $AD - BC = 1$ and organizing q into real and imaginary parts, we obtain

$$q = \left(\frac{A - D}{2C} \right) \pm j \frac{\left[1 - \left(\frac{A+D}{2} \right)^2 \right]^{1/2}}{C} = z_m + jz_0 \quad (\text{A.13})$$

The real and imaginary parts of (A.13) determine z_m , the location of the minimum beam waist relative to the first element of the unit cell (since $z = 0$ describes the

position of the beam waist), and z_0 , which contains the minimum beam waist value, w_0 .

Thus, the beam waist can be determined for any space d_n within the APM cavity as follows. We calculate the ABCD matrix for a unit cell starting with d_n . We next use (A.6) and (A.13) to determine the nearest minimum beam waist and its value. The spatially-shifted version of (A.8),

$$w^2(z) = w_0^2 \left[1 + \left(\frac{\lambda_0 (z - z_m)}{\pi n w_0^2} \right)^2 \right] \quad (\text{A.14})$$

where z_m is the location of the nearest minimum beam waist as determined from (A.13), can then be used to determine the beam waist everywhere within d_n . By applying this type of evaluation to each space d_1 – d_3 within the APM cavity, we arrive at the spot size plot of Figure 2.2 a.

Bibliography

- [1] L. F. Mollenauer and R. H. Stolen. The soliton laser. *Optics Letters*, 9(1):13-15, January 1984.
- [2] G. Sucha, S. R. Bolton, S. Weiss, and D. S. Chemla. Period doubling and quasi-periodicity in additive-pulse mode-locked lasers. *Optics Letters*, 20(17):1794-1796, 1996.
- [3] U. Morgner, L. Rolefs, and F. Mitschke. Dynamic instabilities in an additive-pulse mode-locked Nd:YAG laser. *Optics Letters*, 21(16), August 1996.
- [4] Joseph F. Pinto, Efstratios Georgiou, and Clifford R. Pollock. Stable color-center laser in OH-doped NaCl operating in the 1.41- to 1.81- μm region. *Optics Letters*, 11(8):519-521, August 1986.
- [5] Joseph Francis Pinto. *Development of a Color Center Laser in Sodium Chloride*. PhD thesis, Cornell University, January 1989.
- [6] J. H. Schulman and W. D. Compton. *Color Centers in Solids*. The Macmillan Company, 1962.
- [7] Y. Farge and M. P. Fontana. *Electronic and Vibrational Properties of Point Defects in Ionic Crystals*. North-Holland Publishing Co., 1979.
- [8] Clifford R. Pollock. *Fundamentals of Optoelectronics*. Richard D. Irwin, Inc., 1995.
- [9] D. R. Preuss and J. L. Gole. Three-stage birefringent filter tuning smoothly over the visible region: Theoretical treatment and experimental design. *Applied Optics*, 19(5):702-710, March 1980.
- [10] Robert A. Meyers, editor. *Encyclopedia of Lasers and Optical Technology*. Academic Press, 1991.
- [11] Anthony E. Siegman. *LASERS*. University Science Books, 1986.
- [12] Christopher P. Yakymyshyn, Joseph F. Pinto, and Clifford R. Pollock. Additive-pulse mode-locked NaCl:OH⁻ laser. *Optics Letters*, 14(12):621-623, June 1989.

- [13] Jay M. Weisenfeld, Linn F. Mollenauer, and Erich P. Ippen. Ultrafast configurational relaxation of optically excited color centers. *Physical Review Letters*, 47(23):1668–1671, December 1981.
- [14] Marvin J. Weber, editor. *CRC Handbook of Laser Science and Technology*, volume IV. CRC Press, Inc., 1986.
- [15] J. Guckenheimer and P. Holmes. *Nonlinear Oscillations, Dynamical Systems, and Bifurcations of Vector Fields*. Springer, 1983.
- [16] E. N. Lorenz. Deterministic nonperiodic flow. *Journal of Atmospheric Sciences*, 20:130, 1963.
- [17] Steven H. Strogatz. *Nonlinear Dynamics and Chaos*. Addison-Wesley Publishing Company, 1994.
- [18] B. B. Mandelbrot. *The Fractal Geometry of Nature*. W. H. Freeman, 1983.
- [19] Francis C. Moon. *Chaotic and Fractal Dynamics*. John Wiley & Sons, Inc., 1992.
- [20] Anastasios A. Tsonis. *Chaos*. Plenum Press, 1992.
- [21] Hassler Whitney. Differentiable manifolds. *Annals of Mathematics*, 37(3):645–682, July 1936.
- [22] N. H. Packard, J. P. Crutchfield, J. D. Farmer, and R. S. Shaw. Geometry from a time series. *Physical Review letters*, 45(9):712–716, September 1980.
- [23] J. -C. Roux, Reuben H. Simoyi, and Harry L. Swinney. Observation of a strange attractor. *Physica D*, 8D:257–266, December 1982.
- [24] J. -P. Eckmann and D. Ruelle. Ergodic theory of chaos and strange attractors. *Reviews of Modern Physics*, 57(3):617–656, July 1985.
- [25] Alan Wolf, Jack B. Swift, Harry L. Swinney, and John A. Vastano. Determining lyapunov exponents from a time series. *Physica D*, 16D(3):285–317, 1985.
- [26] Reggie Brown, Paul Bryant, and Henry D. I. Abarbanel. Computing the lyapunov spectrum of a dynamical system from an observed time series. *Physical Review A*, 43(6):2787–2806, March 1991.
- [27] Kensuke Ikeda. Multiple-valued stationary state and its instability of the transmitted light by a ring cavity system. *Optics Communications*, 30(2):257–261, August 1979.
- [28] Celco Grebogi, Edward Ott, and James A. Yorke. Critical exponent of chaotic transients in nonlinear dynamical systems. *Physical Review Letters*, 57(11):1284–1287, September 1986.

- [29] Matthew B. Kennel, Reggie Brown, and Henry D. I. Abarbanel. Determining embedding dimension for phase-space reconstruction using a geometrical construction. *Physical Review A*, 45(6):3403–3411, March 1992.
- [30] Gregg Sucha. Self-starting of an additive-pulse mode-locked color-center laser. *Optics Letters*, 16(12):922–924, June 1991.
- [31] F. M. Mitschke and L. F. Mollenauer. Stabilizing the soliton laser. *IEEE Journal of Quantum Electronics*, QE-22(12):2242–2250, December 1986.
- [32] G. Steinmeyer, A. Buchholz, M. Hänsel, M. Heuer, A. Schwache, and F. Mitschke. Dynamical pulse shaping in a nonlinear resonator. *Physical Review A*, 52(1):830–838, July 1995.
- [33] B. C. Collings, J. B. Stark, S. Tsuda, W. H. Knox, J. E. Cunningham, W. Y. Jan, R. Pathak, and K. Bergman. Saturable bragg reflector self-starting passive mode locking of a Cr^{4+} :YAG laser pumped with a diode-pumped Nd:YVO₄ laser. *Optics Letters*, 21(15):1171–1173, August 1996.
- [34] G. R. Jacobovitz-Veselka, U. Keller, and M. T. Asom. Broadband fast semiconductor saturable absorber. *Optics Letters*, 17(24):1791–1793, December 1992.
- [35] Edward Ott, Celso Grebogi, and James A. Yorke. Controlling chaos. *Physical Review Letters*, 64(11):1196–1199, March 1990.
- [36] E. R. Hunt. Stabilizing high-period orbits in a chaotic system: The diode resonator. *Physical Review Letters*, 67(15):1953–1955, October 1991.
- [37] R. Roy, T. W. Murphy, Jr., T. D. Maier, Z. Gills, and E. R. Hunt. Dynamical control of a chaotic laser: Experimental stabilization of a globally coupled system. *Physical Review Letters*, 68(9):1259–1262, March 1992.
- [38] Serge Bielawski, Dominique Derozier, and Pierre Glorieux. Controlling unstable periodic orbits by a delayed continuous feedback. *Physical Review E*, 49(2):R971–R974, February 1994.
- [39] Joseph T. Verdeyen. *Laser Electronics*. Prentice-Hall, Inc., 3 edition, 1995.